UNIVERSITÀ
DEGLI STUDI
FIRENZE

DOTTORATO DI RICERCA
INTERNATIONAL DOCTORATE IN STRUCTURAL BIOLOGY

CICLO XXXI

COORDINATOR Prof. Claudio Luchinat

COMPUTATIONAL ASPECTS OF PROTEIN AGGREGATION IN NEURODEGENERATIVE DISEASES

Settore Scientifico Disciplinare CHIM/03

PhD student
Dott. Giovanni Bellomo

Tutor
Prof. Claudio Luchinat

Coordinator
Prof. Claudio Luchinat

November 2015 – 2019

This thesis has been approved by the University of Florence, the University of Frankfurt and the Utrecht University

Universiteit Utrecht

CERM Firenze

Table of Contents

General Introduction

The research work performed during the doctorate focused on the computational aspects of the kinetics of aggregation and interaction of amyloidogenic proteins involved in neurological disorders.

Incorrectly folded proteins may lose their colloidal stability, resulting in the formation of soluble oligomers and insoluble amyloidogenic aggregates. Amyloid fibrils are protein aggregates characterized by a filamentous β-sheet-rich structure.[1] Although specific amyloidogenic proteins, such as α-synuclein (α-syn), β-amyloid (Aβ), huntingtin, prion protein (PrP), etc., are known to be involved in neurodegenerative diseases, the current understanding of fibril formation mechanisms implies that at certain (sometimes non-physiological) conditions almost every protein may form fibrillary structures.[1] In the human organism, although there are few evidences of functional and physiological amyloids,[2] these structures generally lead to amyloidosis by forming insoluble plaques, which accumulate in tissues and organs, leading to disruption of their normal functions.[3,4] Some of the most known amyloid-related human disorders are listed below in Table 1.

Disease	Protein featured
Alzheimer's disease	Aβ1-40/42, Tau
Diabetes mellitus type 2	Amylin
Parkinson's disease	α-syn
Bovine spongiform encephalopathy	PrP
Fatal Familial Insomnia	PrP
Huntington's Disease	Huntingtin
Medullary carcinoma of the thyroid	Calcitonin
Isolated atrial amyloidosis	Atrial natriuretic factor
Atherosclerosis	Apolipoprotein AI
Rheumatoid arthritis	Serum amyloid A
Aortic medial amyloid	Medin
Prolactinomas	Prolactin
Familial amyloid polyneuropathy	Transthyretin
Dialysis-related amyloidosis	β2M
Amyloid light-chain (AL) amyloidosis	Immunoglobulin light chains
Amyotrophic lateral sclerosis	TDP-43

Table 1: List of some of the most important amyloidogenic proteins and related human pathologies.

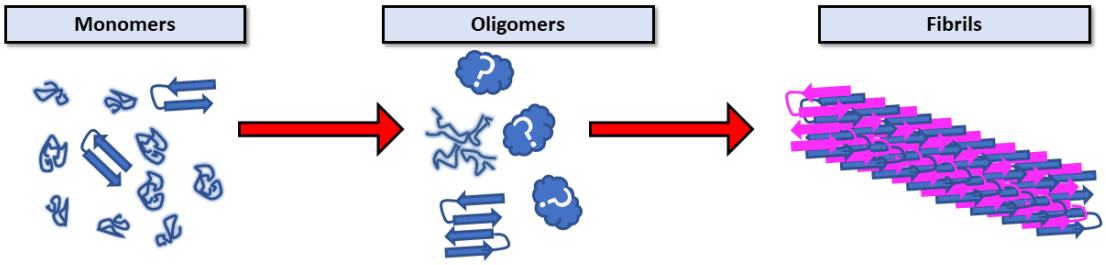

Fig 1 Aggregate classification for amyloidogenic proteins. ***Monomers:*** *Native and (generally) unfolded proteins.* ***Oligomers:*** *transient intermediate aggregates, soluble oligomers and protofibrils are known to be the most toxic species among the aggregates of amyloidogenic proteins. Oligomeric intermediates can either have fibrillary β-sheet structure or be in a more globular and amorphous state.* ***Fibrils****: last stage of aggregation, fibrils have well characterized cross β-sheet motif. Fibril structure, although characterized by a common cross β-sheet motif, is found be different between different proteins and isoforms of the same proteins (e.g. S-shape structure for Aβ1-42, U-shape structure for Aβ1-40).*

In particular, Aβ1-40 and α-synuclein (α-syn) are strictly linked to the onset and progression of Alzheimer's disease (AD)[5] and Parkinson's disease (PD),[6] which are the two most common neurodegenerative disorders. These pathologies affect more than 50 million people worldwide[7] with enormous social and economic costs. The kinetics of the aggregation of amyloidogenic proteins can be very complex as both on-pathway and off-pathway oligomeric intermediates can be formed. Furthermore, aggregates with different structure and different kinetic rates for growth and dissociation are possible, depending on the specific conditions. So, several transient species, can be formed before the formation of fibrils that are generally considered local minima in the energy profile of amyloidogenic aggregation processes.[8–12] Although the mechanisms of toxicity are still not fully understood, what is emerging nowadays is that soluble oligomeric intermediates of Aβ and α-syn appear more toxic than fibrils.[8] In fact, the existence of non-demented individuals with advanced AD neuropathology demonstrates that, at least for Aβ peptides, the plaque burden does not correspond to cognition impairment or degeneration,[13] while both Aβ and α-syn oligomers were found to damage cellular membranes[14–16] and to interfere with proteasomal function[17] with a much greater extent with respect to fibrils.

The first chapter of the thesis work mainly involves the biophysical aspects of the aggregation mechanisms of Aβ1-40, the most common and less toxic isoform of Aβ.[18] During this study, we developed a kinetic model describing the formation of oligomeric and fibrillary species by using data coming from solution NMR. This work started by an extensive literature search of the available kinetic models describing protein aggregation, from the

very pioneering study of Osawa[19] of 1969 to the more recent models developed by of Knowles, Dobson and co-workers,[9] that demonstrates that *secondary nucleation*[20] can play an important role in the aggregation kinetics of Aβ1-42.[21] Successively, we performed several tests to find the suitable experimental conditions for monitoring an unbiased aggregation by 1D ^{1}H solution NMR experiments and, in the end, we proceeded with the kinetic modelling on the experimental NMR profiles of monomeric Aβ1-40. In our work we proved that solution NMR is a valuable technique for the investigation of the aggregation kinetics of the Aβ1-40 peptide that provides a complementary point of view compared to ThT fluorescence. We developed a computational model that fits well the trend of the monomer consumption and supports the existence of at least two categories of aggregates: oligomers and fibrils, with different rates of growth. Despite the existence of oligomeric and fibrillar species in Aβ1-40 aggregation is a well-established concept, the quantification of the aggregation rates involving these species and the development of a reliable computational model is an important step forward for the comprehension of Aβ aggregation processes. Furthermore, it makes possible to quantify the actual impact of drug candidates in contrasting aggregation and protein misfolding.

The comprehension of the aggregation mechanism of amyloidogenic proteins has several possible direct applications. Among them, the recent development Protein Misfolding Cyclic Amplification (PMCA)[22] and Real-Time Quaking Induced Conversion (RT-QuIC)[23] for α-syn opened new doors for the early-stage diagnosis of PD and other synucleinopathies. With respect to this, the second chapter involves the application of the expertise earned while studying the aggregation kinetics of amyloidogenic proteins for the development of a diagnostic biophysical assay for the diagnosis of synucleinopathies. These assays work by amplifying the amount of α-syn aggregates in samples containing imperceptible concentration of aggregates. This approach makes it possible to increase the detection limit of α-syn aggregates present in a biological fluid or tissue homogenate, with a profound impact in diagnosis. The chapter starts with the review made on PMCA and RT-QuIC applied on synucleinopathies,[24] continues with computer simulations and then, the results relative to the tests performed with preformed aggregates and human Cerebrospinal Fluid (CSF) samples are shown. In the second chapter is described, and demonstrated by several aggregation experiments, how the sensitivity of these assays is strongly dependent on the fragmentation, nucleation and elongation kinetics of α-syn aggregates, which in turn depend on biophysical factors such as temperature, shaking modalities, pH, ionic strength, the

presence of preformed aggregates, the presence of detergents, monomer starting concentration and the presence of CSF.

From the observation that compounds present in human CSF interact with α-syn monomer and inhibit the aggregation of α-syn in RT-QuIC experiments, we started to investigate the proteostasis of α-syn in biofluids and analyzed its interaction with some of the most abundant compounds found in CSF and blood serum. Indeed, CSF is involved the spreading of α-syn aggregates in PD.[25] Once some intracellular lysosomal[26] and proteasomal[17] degradation pathways are compromised (by genetics or by the action of fibrils and oligomers) and can no longer sustain the amount of fibrils or oligomers present in the cell, some of the aggregates are expelled by exocytosis[25] or by passive diffusion[14] in the extracellular environment and in CSF where some of these oligomers/fibrils can be transferred to blood and degraded through the brain glymphatic system.[27] In chapter 3, the effect of some of the most abundant compounds present in CSF on α-syn aggregation was investigated. Surprisingly, we observed a direct interaction between monomeric α-syn and Human Serum Albumin (most abundant protein in CSF and serum). We found that HSA can interact with monomeric α-syn and to inhibit its aggregation in an ionic strength and pH dependent manner. This effect can be relevant in blood, due to the high concentration of HSA and α-syn; indeed, α-syn is found to be able to cross the Brain Blood Barrier (BBB) bidirectionally[28] moving from CSF to blood and *vice versa*; moreover, it is also physiologically highly expressed in human red blood cells.[29] Apart from being biologically relevant, the antiaggregatory effects of HSA on α-syn will be something to take into account also in future developments of α-syn RT-QuIC assays for serum samples. In chapter 3, we also characterized the interaction between α-syn and High-Density Lipoproteins (HDL) coming from human plasma, which were previously reported to inhibit Aβ aggregation in CSF.[30] We did not observe a direct interaction between plasma HDL and monomeric α-syn by NMR, but we observed a drastic reduction of both oligomeric and fibrillary aggregates by ThT aggregation assays and conformation specific antibodies, suggesting an interaction between oligomeric α-syn and HDL that may exert a protective role in the human organism.

The fourth chapter of the thesis is about the development of computational tools for the automatic assignment of 3D NOESY ^{1}H-^{15}N HSQC to answer the need of a fast and cost-effective way to screen different folded proteins, with known X-ray structure. Although it may seem not so related to the field of neurological diseases, this project was born in late 2017 to answer the need of a fast and cost-effective way to screen different folded proteins, with

known X-ray structure. This protocol can have sizeable impact in the whole structural biology, making possible to rapid access to NMR assignments in the large number of sample where the structure is already known, and without the need of ^{13}C labelling. Since the approach to this problem is very general, the results of this research might be useful for any protein-ligand screening also outside the field of neurological disorders.

1 Aggregation kinetics of Aβ1-40

1.1 Overview

The filamentous growth processes of amyloids involve the assembly of elementary units to the ends of growing structures. The physical concepts of nucleation and polymerization applied to biofilaments date back to the work of Osawa et al.[19] (1962), in which kinetic models have been developed to describe the formation of cytoskeletal structures. This early investigation of filamentous growth was focused on homogeneous nucleation of template units followed by linear polymerization. In the following decades, Ferrone and coworkers adapted these linear polymerization models for the study of protein accumulation diseases.[10,31] In more recent years, the groups of Murphy[11,12] and Dobson[9,32,33] are the ones that more than others contributed to this field. The Dobson's group in 2011 obtained a closed-form system of differential equations (also finding approximated analytical solutions) describing the formation of amyloidogenic fibrils, taking into account fragmentation mechanisms and applied the concept of "secondary surface catalyzed nucleation"[32] to amyloid aggregation kinetics. Apart from the growth, fragmentation, nucleation and secondary nucleation of fibrils, in the last years, the role of on-pathway oligomers emerged as a key feature of both Alzheimer's disease and Parkinson's disease. Recent works demonstrated that the formation of fibrillar aggregates depend upon the structural reorganization of prefibrillar oligomers.[34–36] These findings suggest that considering only fibrillar species while studying amyloid aggregation kinetics my be too reductive. In the paragraph below is attached the published paper and the supporting information relative to the work on the aggregation of Aβ1-40 published in 2018 on *Chemical Communications*. This article is part of the themed collection "Amyloid Aggregation",[37] for which we have also been asked to produce an artwork for the back cover page. The supporting information is also provided for this work, since some of the results were not inserted in main text due to the strict page limit of the journal. In paragraph 1.3 are also reported some of the unpublished data relative to the experiments performed to find the optimal conditions to make the Aβ1-40 peptide aggregate in the most reproducible way. Although this data were not included in the publication, I think that they might be useful for other researchers.

1.2 Aggregation kinetics of Aβ1-40 monitored by NMR

Showcasing research from the Magnetic Resonance Center (CERM) and Chemistry Department of the University of Florence, Sesto Fiorentino, Italy.

Aggregation kinetics of the Aβ1–40 peptide monitored by NMR

The aggregation of Aβ1–40 was studied by solution NMR. The data support a kinetic model where monomers initially aggregate with the reversible formation of oligomers, which then irreversibly convert into fibrils. This, not only sheds new light on the aggregation process, but helps in designing new potential drugs.

As featured in:

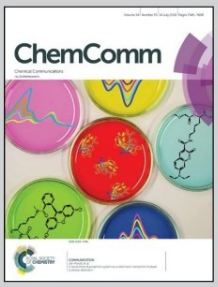

See Moreno Lelli, Claudio Luchinat *et al.*, *Chem. Commun.*, 2018, **54**, 7601.

ROYAL SOCIETY OF CHEMISTRY

rsc.li/chemcomm

Registered charity number: 207890

ChemComm

COMMUNICATION

View Article Online
View Journal | View Issue

Check for updates

Cite this: *Chem. Commun.*, 2018, 54, 7601

Received 20th March 2018,
Accepted 3rd May 2018

DOI: 10.1039/c8cc01710g

rsc.li/chemcomm

Published on 16 May 2018. Downloaded by Universita Studi di Firenze on 11/12/2018 1:40:46 PM.

Aggregation kinetics of the Aβ1–40 peptide monitored by NMR†

Giovanni Bellomo, [a] Sara Bologna,[a] Leonardo Gonnelli,[a] Enrico Ravera, [ab] Marco Fragai, [ab] Moreno Lelli [*ab] and Claudio Luchinat [*abc]

The aggregation of Aβ1–40 was monitored by solution NMR, which showed a trend complementary to the one observed by ThT-fluorescence. The NMR data support a kinetic model where Aβ1–40 initially aggregates with the reversible formation of oligomeric species, which then irreversibly convert into fibrils.

Aβ1–40, Aβ1–42 and τ-protein are involved in the onset and progression of Alzheimer's disease (AD).[1] In particular, the Aβ peptides are the major constituents of the amyloid plaques found in biopsies of AD patients. Although Aβ1–40 is the most common isoform of Aβ, Aβ1–42 seems to be more toxic and more prone to aggregation.[2] Moreover, the structure of the final fibrillary aggregates of Aβ1–40[3,4] is found to be different from the one of Aβ1–42[5–7] and not univocal.[8] There is also evidence that the structure of the transient oligomeric species might be different for the two isoforms, with Aβ1–42 forming more fibril-like oligomers, rich in β-sheets, and Aβ1–40 forming more globular and amorphous aggregates.[9–11] The soluble oligomers and especially the low molecular weight (LMW) oligomers were shown to be the most toxic species among all the Aβ aggregates.[12,13] These findings suggest that the aggregation kinetics may be different for the two isoforms of Aβ as proposed in some of the kinetic models developed over the years.[14–18] The development of kinetic models and the understanding of the aggregation mechanisms of amyloidogenic proteins would be dramatically important in designing new therapies and drugs. In 2011, Knowles and co-workers[17] developed a two-species (monomers and fibrils) model describing the aggregation of Aβ1–42. They also introduced the idea of surface-catalysed secondary nucleation[19] and tested the model against ThT fluorescence data at different monomer concentrations.[20] The model was then adapted[18] to Aβ1–40, observing strong differences in nucleation behaviour and suggesting that secondary nucleation saturates above 6 μM of Aβ1–40 monomer concentration. However, Kelly and co-workers[21] brought up evidence of conversion of soluble globular oligomers of Aβ1–40 into fibrils; this evidence was also supported by other works.[22–24] These findings suggest that considering only two species for the kinetic modelling of amyloid aggregation, at least for Aβ1–40, could be reductive. For this reason, we investigated the aggregation kinetics of Aβ1–40 by solution NMR, focusing our attention on the early stage of the aggregation. The peculiarity of NMR is that it monitors directly the free monomer concentration, which is affected from the beginning of the aggregation process, thus providing complementary information with respect to ThT-fluorescence. With modern high-field instruments the NMR experiments can be performed under near physiological conditions, at a micromolar concentration range and without the need to add fluorescent or chromophoric probes that may alter the aggregation.[25] Solution NMR was already applied to study the aggregation of the Aβ peptides: Fawzi *et al.*[26,27] obtained information about oligomeric species of Aβ1–40/42 using the dark-state exchange saturation transfer (DEST), probing the exchange processes between monomers and protofibril-bound states. Pauwels *et al.*[28] and Bax and coworkers[29] monitored the Aβ1–40/42 aggregation with NMR and ThT-fluorescence but they did not propose kinetic models for the amyloidogenic process. Ramamoorthy and coworkers obtained a high resolution structure of a partially folded Aβ1–40 monomer with solution NMR[30] and observed directly the formation of at least five different oligomeric species by using ^{19}F-NMR on a ^{19}F labelled Aβ1–40 peptide.[31] They also further characterized some oligomeric aggregates with solid-state NMR in a subsequent work.[32] Oligomerization kinetics was monitored also by Bertini and co-workers with sedimentation NMR,[9,33] trapping oligomeric species of about 70–80 kDa by MAS induced sedimentation. In order to obtain information about the aggregation kinetics of Aβ1–40 we acquired a series

[a] *Magnetic Resonance Center (CERM), University of Florence, Via L. Sacconi 6, 50019 Sesto Fiorentino, Italy. E-mail: lelli@cerm.unifi.it, luchinat@cerm.unifi.it*
[b] *Department of Chemistry "Ugo Schiff", University of Florence, Via della Lastruccia 3, 50019 Sesto Fiorentino, Italy*
[c] *Giotto Biotech S.R.L., Via Madonna del Piano 6, 50019 Sesto Fiorentino, Florence, Italy*

† Electronic supplementary information (ESI) available: Supporting figures, mathematical description of kinetic models, and experimental details. See DOI: 10.1039/c8cc01710g

Published on 16 May 2018. Downloaded by Universita Studi di Firenze on 11/12/2018 1:40:46 PM.

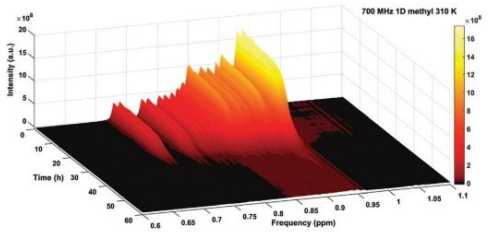

Fig. 1 Series of 1D ^{1}H NMR spectra of the methyl region of a 50 μM sample of Aβ1–40 plotted with MATLAB. Spectra were acquired using a 700 MHz (16.4 T) spectrometer, using an ammonium acetate buffer at pH 8.5 (see details in the ESI†). Spectra were binned with AMIX software (bin width = 0.005 ppm) prior to image formation.

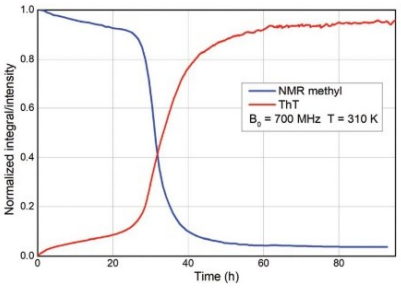

Fig. 2 Aggregation kinetics of 50 μM of Aβ1–40 at 310 K and pH 8.5. The decrease in the methyl proton integral showed a behaviour complementary to the ThT fluorescence intensity. NMR integrals were normalized by dividing them by the highest value, ThT fluorescence data were normalized setting the point at 92.8 h to 1 – (the NMR normalised integral) in that point.

of 1D ^{1}H NMR spectra under quiescent conditions. The NMR investigation was performed on recombinant Aβ1–40 samples at pH 8.5 and with concentrations between 30 and 100 μM, for details see the ESI.† This higher than physiological pH was chosen because it corresponds to the pH where Aβ1–40 easily forms fibrils with high reproducibility.[3] The temperature was set to the physiological value of 310 K in order to avoid a too long lag-time, considering that the elongation rate of amyloids strongly increases with temperature,[34] while lower temperatures can promote a partially folded state of the monomer.[30] In Fig. 1, we report the trend of the methyl region of the 1D ^{1}H spectrum as a function of time up to the almost complete disappearance of the monomer resonances. The intensities of the methyl peaks decreased with an almost sigmoidal behaviour with a slow decrease in monomer concentration of about 10% during the first 20 hours; then a sharp concentration decrease is observed, with the consumption of most of the monomer, followed by a final plateau where the monomer concentration remained almost stationary at less than 2% of the initial amount. Similar trends were observed also for the aromatic resonances (see the ESI,† Fig. S3), but we analysed the methyl region because of the higher signal to noise ratio.

To get insight into this process, we repeated the aggregation experiment by monitoring another 50 μM Aβ1–40 sample simultaneously through NMR and ThT fluorescence. Fig. 2 reports the NMR integral of the methyl region as a function of time compared with the increase in the fluorescence signal. The presence of ThT can affect the kinetics of the fibril formation, especially with ThT concentration comparable to the one of Aβ1–40.[25] Thus we kept the ThT concentration at 5 μM (1/10 of the Aβ1–40 concentration) and we added it in both the NMR tube and the quartz cuvette. Notably, the drop of the monomer concentration happens in concomitance with the growth of the fluorescence (due to fibril formation), with an almost complementary trend. The NMR experiments were repeated at different initial monomer concentrations (30, 50 and 100 μM) in order to understand the impact of the concentration on the aggregation kinetics. The decrease in the integrals of the methyl spectrum as a function of time is reported in Fig. 3 and is almost entirely associated to the monomer consumption (see the ESI† and Fig. S1). We fitted these experimental data using three different kinetic models. In Fig. 3A, the NMR integrals are fitted with the model developed by Knowles and coworkers.[18] This model was created also considering the previous works of Oosawa,[35] Ferrone,[16] Murphy[17] and Pöschel.[36] In this two-species model, the monomeric Aβ is expected to nucleate directly to fibrils, which in turn can elongate, dissociate or fragment into shorter fibrils.

Secondary nucleation catalysed by the fibril surface is also included, as it was demonstrated to have a key role for Aβ1–42. This model was adapted[19] to fit the aggregation trend of Aβ1–40 at pH 7.4, introducing a saturation limit for the secondary nucleation for Aβ1–40 monomer concentration: the results of the fitting to this model are shown in Fig. 3B. In Fig. 3A and B the simulated curves reproduce the sigmoidal-like decrease at the main inflection point, but the agreement is rather poor for the initial part of the trend. We thus decided to modify the model of Knowles considering also the formation of oligomeric species. In our model (depicted in Fig. S4 and eqn (S1), (S2) in the ESI†), monomers can nucleate into oligomers, the nucleation kinetics considered is fundamentally equal to the one used by Knowles,[18] Ferrone,[16] Pöschel[36] and to the one originally developed by Oosawa.[35] In our case, however, monomers do not nucleate directly into fibrils but into transient oligomeric aggregates. Oligomers can grow and decrease by addition or dissociation of monomers, as well as fibrils, but with different kinetic rates with respect to the latter. For the depolymerization kinetics we used slightly different terms in the kinetic equations resulting in a total probability of monomer detachment proportional to the oligomer size (see the ESI†). The crucial part of the model is the introduction of a conversion kinetics step from oligomers to fibrils: when the oligomers reach a given critical size n_c (*e.g.* 20 monomers in the present case) they are allowed to irreversibly convert into fibrils. Fibrils can then grow and decrease through polymerization and depolymerization by the addition or release of monomers with a kinetics identical to the one of the previously cited models.[15,16,20,35,36] Likewise, fibrils can also fragment producing smaller fibrils (not oligomers or monomers)

 This journal is © The Royal Society of Chemistry 2018

Published on 16 May 2018. Downloaded by Universita Studi di Firenze on 11/12/2018 1:40:46 PM.

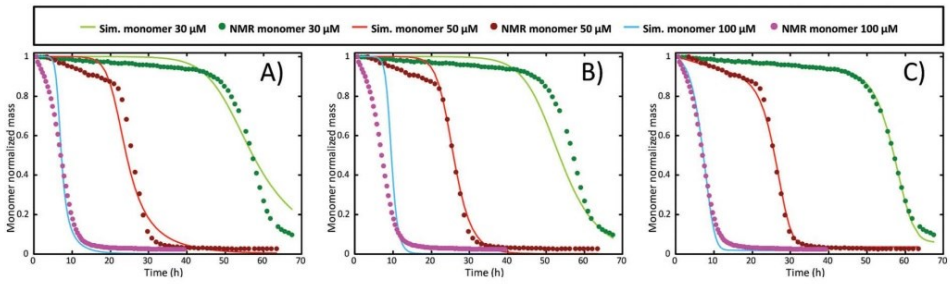

Fig. 3 Simulated monomer populations were fitted in parallel to the experimental NMR data: integrals of the methyl region of 1D solution NMR spectra at 30, 50 and 100 μM Aβ1–40 initial monomer concentration (pH 8.5, T = 310 K). Three different kinetic models were tested on these data: in (A) the two-species model for Aβ1–42, in (B) the two-species model for Aβ1–40, while in (C) the "conversion" model developed in this work.

that can then act as new seeds for polymerization. In this model fibrils are not allowed to fragment in species smaller than the critical size n_c. In this way, fragmentation of fibrils only produces fibrils above the critical size and this is why we named this process "fibril closed fragmentation". With this kinetic model we fitted the experimental data in Fig. 3C. The addition of the irreversible conversion from oligomers into fibrils allowed for a significantly better agreement between the simulated and the experimental data with respect to the previous models, especially for the initial part of the aggregation. Notably, this model fits well the evolution during the lag-time when oligomers are supposed to be formed; by NMR we can monitor this evolution through the monomer consumption while the fluorescence remains quite low. The fitted kinetic constants of the three tested models are shown in Table S1 in the ESI.† In our "conversion model" the kinetic constant for the fibril growth (k_+) is an order of magnitude higher than the one for the monomer addition to oligomeric species (k_{+ol}). This difference explains why, once a sufficient amount of large oligomers is converted to fibrils, monomers start to be rapidly consumed while the mass of fibrils rapidly increases producing a sigmoidal-like behaviour for the monomer consumption kinetics. In the third part of the trend, in the tail of the sigmoidal decrease, where most of the peptides are aggregated into fibrils, the process of monomer dissociation remains the only relevant, and is responsible for the residual amount of monomer still present in solution. In the previously published models for Aβ1–40[19] and Aβ1–42[18] there is no distinction between "oligomers" and "fibrils" and a single polymerization constant is fitted for all the aggregation steps. With these models the rapid monomer consumption of the sigmoidal trend is the result of a strong secondary nucleation that becomes explosively strong as soon as there is a small amount of long-fibrils formed. On the basis of the fitted kinetic constants we back-calculated the relative fibril size distribution for the three models (Fig. S7–S9, ESI†). As shown in Fig. S7 (ESI†) (50 μM sample) for the Aβ1–42 and Aβ1–40 models, it can be observed that, at the end of the aggregation process ($t \sim 60$ h), the majority of the fibrils should have a size smaller than 20 monomers, and for the Aβ1–42 model even smaller than 10 monomers (40 kDa). In the trials we made, only the model based on the oligomer-to-fibril conversion predicts the formation of fibrils larger than 433 kDa (>100 mers). Indeed, the strong secondary nucleation process of the first two models results in a rapid formation of dimers during the sigmoidal step that are not able to elongate much because of the depleted monomer concentration in solution. In our conversion model, we have not included secondary nucleation and the "limited" number of converted fibrils favours their elongation towards high molecular weights. We do not exclude that the secondary nucleation process exists for Aβ1–40, since it has been well demonstrated for Aβ1–42,[21] but for Aβ1–40 in our conditions of concentration and pH (8.5), the secondary nucleation seems not to be determinant. Indeed, if secondary nucleation is included in the conversion model (Fig. S5 and Table S2, ESI†), its impact on the fit quality is minimal and the relative kinetic constant remains quite small. Solution NMR is a profitable technique to follow these aggregation processes, because it gives an overview of the sample status. In several cases, the presence of impurities or the concomitant occurrence of degradation processes (for example due to undetectable amounts of proteases[37]) can be determined by 1D ^{1}H NMR spectra. In the ESI† we report the case of degradation (Fig S10), which usually manifests itself with the formation of sharp resonances near the ones of the monomer. Another aspect which needs attention is the presence of preformed aggregates and/or electrostatic surfaces that can drastically promote fibrillation *in vitro*.[38] As an example, in Fig. 4 we show a sample where presumably the presence of a solid impurity promoted the formation of a macroscopic fibrillary aggregate into the NMR tube. The presence of this impurity had a dramatic effect on the aggregation kinetics. Some fibrillary nuclei were formed on its surface at the bottom of the NMR tube. From these quickly formed nuclei the aggregation proceeded mainly through polymerization. This hypothesis is also in line with the observation of an exponential decay of the monomer signal (Fig. 4B). Indeed, with reference to eqn (S6) (ESI†), a pure polymerization kinetics from a preformed concentration of fibrils implies an exponential decay of the monomer.

Published on 16 May 2018. Downloaded by Universita Studi di Firenze on 11/12/2018 1:40:46 PM.

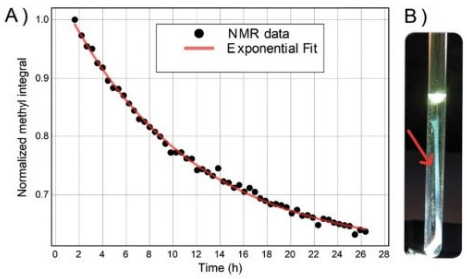

Fig. 4 (A) The kinetic profile of the NMR signal (B_0 = 700 MHz T = 310 K) was fitted with an exponential decay that is typical of a polymerization kinetics. (B) A curious image of an agglomerate of fibrils presumably grown over the surface of an impurity present in the bottom of the NMR tube, the pale blue color resulted from the addition of 5 μM of ThT.

In conclusion, solution NMR is a valuable technique for the investigation of the aggregation kinetics of the Aβ1–40 peptide, giving a complementary point of view compared to ThT fluorescence. We developed a computational model that well fits the trend of the monomer consumption and supports the existence of at least two categories of aggregates: oligomers and fibrils, with different rates of growth. Despite the existence of oligomeric and fibrillar species in Aβ1–40 aggregation is a well-established concept, the quantification of the aggregation rates involving these species and the development of a reliable computational model is an important step forward for the comprehension of Aβ aggregation processes. Furthermore, it makes it possible to quantify the actual impact of drug candidates in contrasting aggregation and protein misfolding.

This work was supported by ERA-NET NEURON ABETA ID, MIUR PRIN 2012SK7ASN, Fondazione Cassa di Risparmio di Firenze, the University of Florence CERM-TT and Instruct-ERIC, an ESFRI Landmark, supported by national member subscriptions. Specifically, we thank the Instruct-ERIC Core Centre CERM, Italy.

Conflicts of interest

There are no conflicts to declare.

Notes and references

1 J. Wang, B. J. Gu, C. L. Masters and Y.-J. Wang, *Nat. Rev. Neurol.*, 2017, **13**, 612–623.
2 K. Parameshwaran, C. Sims, P. Kanju, T. Vaithianathan, B. C. Shonesy, M. Dhanasekaran, B. A. Bahr and V. Suppiramaniam, *Synapse*, 2007, **61**, 367–374.
3 I. Bertini, L. Gonnelli, C. Luchinat, J. Mao and A. Nesi, *J. Am. Chem. Soc.*, 2011, **133**, 16013–16022.
4 J.-X. Lu, W. Qiang, W.-M. Yau, C. D. Schwieters, S. C. Meredith and R. Tycko, *Cell*, 2013, **154**, 1257–1268.
5 Y. Xiao, B. Ma, D. McElheny, S. Parthasarathy, F. Long, M. Hoshi, R. Nussinov and Y. Ishii, *Nat. Struct. Mol. Biol.*, 2015, **22**, 499–505.
6 M. A. Wälti, F. Ravotti, H. Arai, C. G. Glabe, J. S. Wall, A. Böckmann, P. Güntert, B. H. Meier and R. Riek, *Proc. Natl. Acad. Sci. U. S. A.*, 2016, **113**, E4976–E4984.
7 M. T. Colvin, R. Silvers, Q. Z. Ni, T. V. Can, I. Sergeyev, M. Rosay, K. J. Donovan, B. Michael, J. Wall, S. Linse and R. G. Griffin, *J. Am. Chem. Soc.*, 2016, **138**, 9663–9674.
8 R. Tycko, *Protein Sci.*, 2014, **23**, 1528–1539.
9 I. Bertini, G. Gallo, M. Korsak, C. Luchinat, J. Mao and E. Ravera, *ChemBioChem*, 2013, **14**, 1891–1897.
10 C. G. Glabe, *J. Biol. Chem.*, 2008, **283**, 29639–29643.
11 N. J. Economou, M. J. Giammona, T. D. Do, X. Zheng, D. B. Teplow, S. K. Buratto and M. T. Bowers, *J. Am. Chem. Soc.*, 2016, **138**, 1772–1775.
12 D. M. Walsh, I. Klyubin, J. V. Fadeeva, W. K. Cullen, R. Anwyl, M. S. Wolfe, M. J. Rowan and D. J. Selkoe, *Nature*, 2002, **416**, 535–539.
13 S. Lesné, M. T. Koh, L. Kotilinek, R. Kayed, C. G. Glabe, A. Yang, M. Gallagher and K. H. Ashe, *Nature*, 2006, **440**, 352.
14 J. P. Bernacki and R. M. Murphy, *Biophys. J.*, 2009, **96**, 2871–2887.
15 F. Ferrone, *Methods Enzymol.*, 1999, **309**, 256–274.
16 M. M. Pallitto and R. M. Murphy, *Biophys. J.*, 2001, **81**, 1805–1822.
17 S. I. A. Cohen, M. Vendruscolo, M. E. Welland, C. M. Dobson, E. M. Terentjev and T. P. J. Knowles, *J. Chem. Phys.*, 2011, **135**, 065105.
18 G. Meisl, X. Yang, E. Hellstrand, B. Frohm, J. B. Kirkegaard, S. I. A. Cohen, C. M. Dobson, S. Linse and T. P. J. Knowles, *Proc. Natl. Acad. Sci. U. S. A.*, 2014, **111**, 9384–9389.
19 S. Linse, *Biophys. Rev.*, 2017, **9**, 329–338.
20 S. I. A. Cohen, S. Linse, L. M. Luheshi, E. Hellstrand, D. A. White, L. Rajah, D. E. Otzen, M. Vendruscolo, C. M. Dobson and T. P. J. Knowles, *Proc. Natl. Acad. Sci. U. S. A.*, 2013, **110**, 9758–9763.
21 J. Lee, E. K. Culyba, E. T. Powers and J. W. Kelly, *Nat. Chem. Biol.*, 2011, **7**, 602–609.
22 Z. Fu, D. Aucoin, J. Davis, W. E. Van Nostrand and S. O. Smith, *Biochemistry*, 2015, **54**, 4197–4207.
23 M. Cheon, C. K. Hall and I. Chang, *PLoS Comput. Biol.*, 2015, **11**, e1004258.
24 N. Benseny-Cases, M. Cócera and J. Cladera, *Biochem. Biophys. Res. Commun.*, 2007, **361**, 916–921.
25 M. D'Amico, M. G. Di Carlo, M. Groenning, V. Militello, V. Vetri and M. Leone, *J. Phys. Chem. Lett.*, 2012, **3**, 1596–1601.
26 N. L. Fawzi, J. Ying, R. Ghirlando, D. A. Torchia and G. M. Clore, *Nature*, 2011, **480**, 268–272.
27 N. L. Fawzi, J. Ying, D. A. Torchia and G. M. Clore, *Nat. Protoc.*, 2012, **7**, 1523–1533.
28 K. Pauwels, T. L. Williams, K. L. Morris, W. Jonckheere, A. Vandersteen, G. Kelly, J. Schymkowitz, F. Rousseau, A. Pastore, L. C. Serpell and K. Broersen, *J. Biol. Chem.*, 2012, **287**, 5650–5660.
29 J. Roche, Y. Shen, J. H. Lee, J. Ying and A. Bax, *Biochemistry*, 2016, **55**, 762–775.
30 S. Vivekanandan, J. R. Brender, S. Y. Lee and A. Ramamoorthy, *Biochem. Biophys. Res. Commun.*, 2011, **411**, 312–316.
31 Y. Suzuki, J. R. Brender, M. T. Soper, J. Krishnamoorthy, Y. Zhou, B. T. Ruotolo, N. A. Kotov, A. Ramamoorthy and E. N. G. Marsh, *Biochemistry*, 2013, **52**, 1903–1912.
32 S. A. Kotler, J. R. Brender, S. Vivekanandan, Y. Suzuki, K. Yamamoto, M. Monette, J. Krishnamoorthy, P. Walsh, M. Cauble, M. M. B. Holl, E. N. G. Marsh and A. Ramamoorthy, *Sci. Rep.*, 2015, **5**, 11811.
33 I. Bertini, C. Luchinat, G. Parigi and E. Ravera, *Acc. Chem. Res.*, 2013, **46**, 2059–2069.
34 Y. Kusumoto, A. Lomakin, D. B. Teplow and G. B. Benedek, *Proc. Natl. Acad. Sci. U. S. A.*, 1998, **95**, 12277–12282.
35 F. Oosawa and M. Kasai, *J. Mol. Biol.*, 1962, **4**, 10–21.
36 T. Pöschel, N. V. Brilliantov and C. Frömmel, *Biophys. J.*, 2003, **85**, 3460–3474.
37 T. Saido and M. A. Leissring, *Cold Spring Harbor Perspect. Med.*, 2012, **2**, a006379.
38 B. Moores, E. Drolle, S. J. Attwood, J. Simons and Z. Leonenko, *PLoS One*, 2011, **6**, e25954.

This journal is © The Royal Society of Chemistry 2018

Electronic Supplementary Material (ESI) for Chemical Communications.
This journal is © The Royal Society of Chemistry 2018

Supporting Information

Aggregation kinetics of the Aβ1-40 peptide monitored by NMR

Giovanni Bellomo,[a] Sara Bologna,[a] Leonardo Gonnelli,[a] Enrico Ravera,[a,b] Marco Fragai, [a,b] Moreno Lelli,[a,b,*] and Claudio Luchinat [a,b,*]

[a.] *Magnetic Resonance Center (CERM), University of Florence, Via L. Sacconi 6, 50019 Sesto Fiorentino, Italy.*
[b.] *Department of Chemistry "Ugo Schiff", University of Florence, Via della Lastruccia 3, 50019 Sesto Fiorentino, Italy.*
[c.] *Giotto Biotech S.R.L., Via Madonna del Piano 6, 50019 Sesto Fiorentino, Florence, Italy*
**To whom correspondence should be addressed*

Contents

1. 1D ^{1}H NMR experiments to monitor kinetics

The NMR investigation was performed on Aβ1-40 samples at pH 8.5 and with concentrations between 30 and 100 μM. This higher than physiological pH was chosen because it corresponds to the pH where Aβ1-40 easily form fibrils with high reproducibility.[1] Most of the analyses were performed on 1D ^{1}H NMR spectra. 1D spectra were preferred compared to 2D because they provide a higher signal-to-noise ratio for the same amount of time. Figure S1 shows the methyl region of the 1D ^{1}H NMR spectrum of Aβ1-40 acquired at 50 μM, at 310 K and at different times (t). It can be seen that during aggregation the protein signals decay without the growth of any new visible peak or change in the pattern profile: in Figure S1B it is possible to appreciate that the spectrum after 33.2 h maintains the same profile of the monomeric spectrum acquired at 0.66 h with some small differences around 0.95 ppm (that accounts less than 2% of methyl protons starting integral), due to the rescaled signals of protease inhibitors added to prevent protein degradation (see details below, in the Experimental session). We decided to compare our NMR integrals with the simulated monomer concentration (estimated by kinetic models) because we had no hints (no new growing peaks in the 1D NMR spectra) about any contribution from other species in the integration regions we considered, up to 80 h of aggregation.

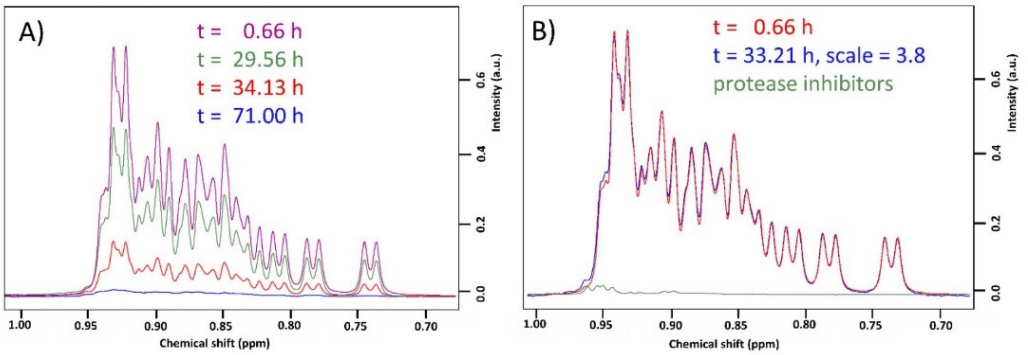

Figure S1: A) Decay of the monomer methyl signals from 1D ^{1}H NMR experiments acquired in a 700 MHz spectrometer. Line broadening was set to 1.0 Hz. The Aβ1-40 monomer starting concentration was 50 μM in ammonium acetate buffer, pH 8.5 and T = 310 K. B) Superposition of the methyl signal at 0.66h (red) with those at 33.21h rescaled (x3.8, blue). The methyl signals retain their shape during aggregation, indicating that species with a spectrum different from monomer are almost not visible by 1D ^{1}H NMR in this spectra region and in our experimental conditions. The only differences between the monomer and the rescaled spectrum, at t = 33 h, can be found at 0.95 ppm where small signals from protease inhibitors are present.

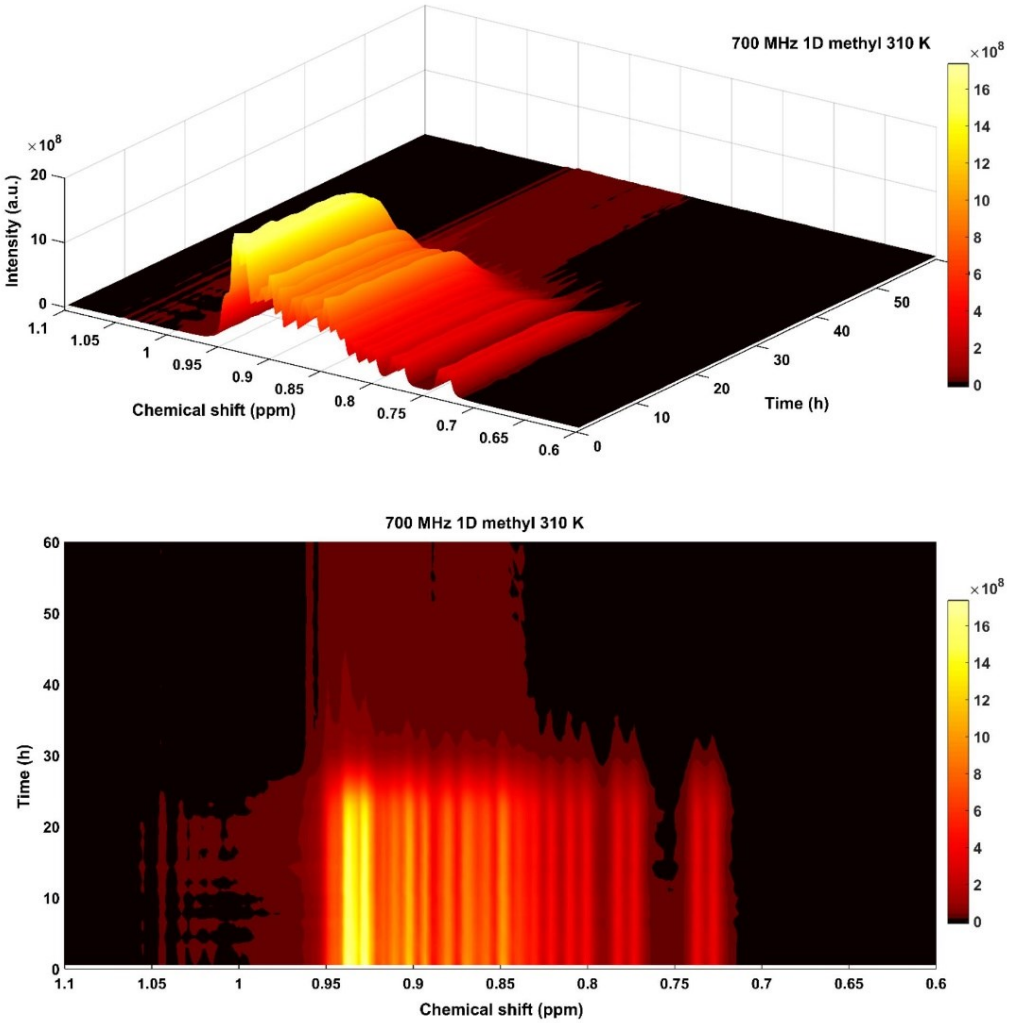

Figure S2: Series of 1D ^{1}H NMR spectra of the methyl region of a 50 µM sample of Aβ1-40 plotted in two different projections (graphical image produced with MATLAB R2017a). Spectra were acquired in a 700 MHz (16.4 T) spectrometer, using an ammonium acetate buffer with 0.2% of sodium azide, 1.0 mM EDTA and protease inhibitors at low concentrations (the ABSF was 10 µM, see Experimental for details). Spectra were binned (bin width = 0.005 ppm) with AMIX (Analysis of MIXtures software, Bruker Biospin) prior to image formation.

In addition to the methyl spectral region, also the aromatic resonances were analysed with very little interference from the background. On these signals, the 1D-NOESY spectra performed better than the 1D ^{1}H excitation sculpting experiments, because the water pre-saturation steps strongly attenuated the buffer resonances in exchange with water (i.e. ammonium and ammonia).

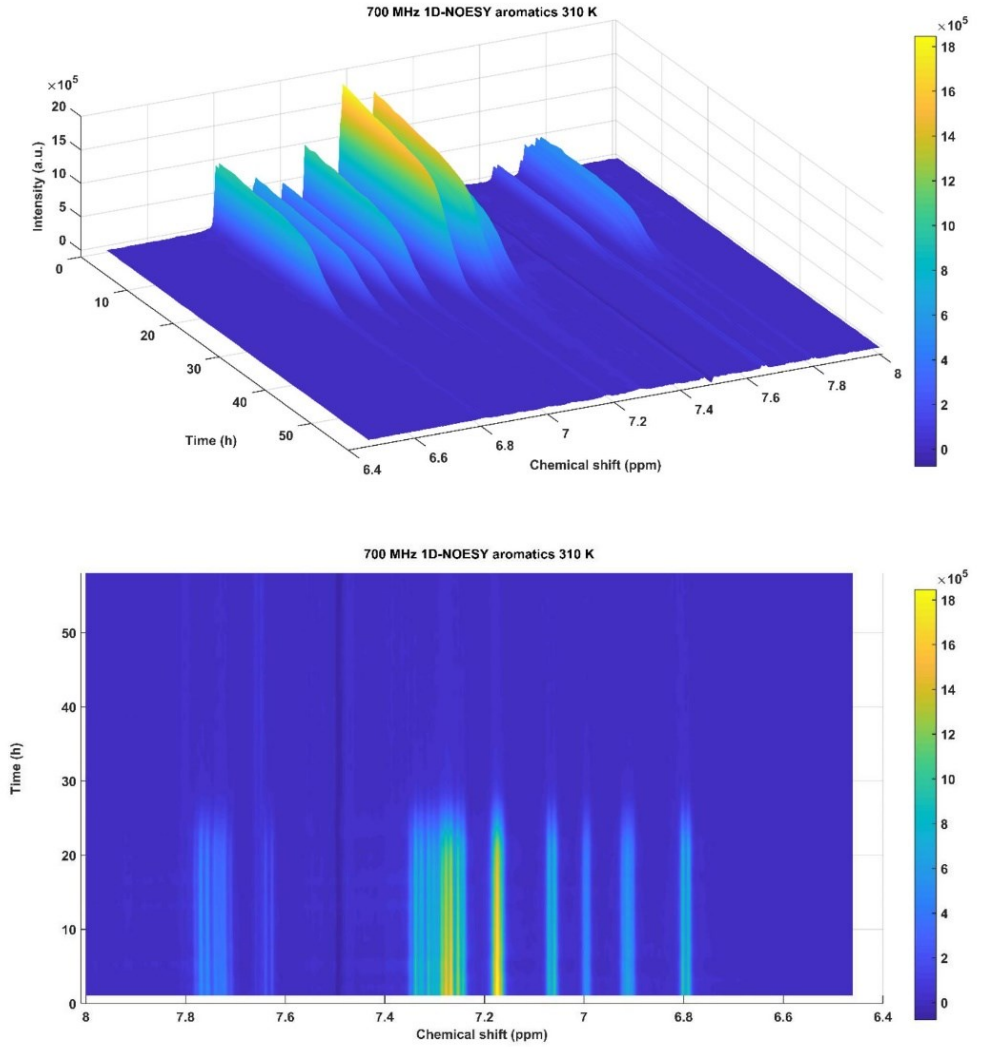

Figure S3: Series of 1D ^{1}H-NOESY spectra of the aromatic region of a 50 µM sample of Aβ1-40 plotted in two different projections, from one side (upper panel) and from the top(lower panel) (graphical image produced with MATLAB R2017a). Spectra were acquired in a 700 MHz (16.4 T) spectrometer, using an ammonium acetate buffer with 0.2% of sodium azide, 1.0 mM EDTA and protease inhibitors at low concentrations (the ABSF was 10 µM, see Experimental Session for details). Spectra were binned (bin width = 0.005 ppm) with AMIX (Analysis of MIXtures software, Bruker Biospin) prior to image formation.

2. Kinetic models

In the model we tested in this work (depicted graphically in Fig. S4 and mathematically in Eq. S1 and S2), monomers can nucleate into oligomers, the nucleation kinetics we considered is fundamentally equal to the one used by Knowles,[2] Ferrone,[3] Pöschel[4] and to the one originally developed by Oosawa.[5] In our case, however, monomers do not nucleate directly into fibrils but into a transient, on pathway oligomeric aggregates. Oligomers can grow and decrease by addition or dissociation of monomers, as well as fibrils, but with different

kinetic rates with respect to the latter. For the growth kinetics of oligomers we applied the same mathematical description of Knowles,[2] Ferrone,[3] Pöschel[4] and Oosawa,[5] while for the depolymerization kinetics we used slightly different terms in the kinetic equations: since oligomers are generally species less stable than fibrils, the overall dissociation rate of a single peptide is likely not the same for any oligomer and we scaled it for the larger monomer content in the aggregate, resulting in a total probability of detachment proportional to the oligomer size. The crucial part of the model is the introduction of a conversion kinetics step from oligomers to fibrils: when the oligomers reach a given critical size n_c (e.g. 20 monomers in the present case) they are allowed to irreversibly convert into fibrils. Fibrils can then grow and decrease through polymerization and depolymerization by addition or release of Aβ1-40 monomers. The mathematical description of the polymerization and depolymerization of fibrils is identical to the one of the cited models.[3–7] Fibrils can then also fragment producing smaller fibrils that can then act as new seeds for polymerization. In this model fibrils are not allowed to fragment in species smaller than the critical size n_c, in this way fragmentation of fibrils only produces fibrils above the critical size and this is why we dubbed this process "fibril closed fragmentation". With this constraint we wanted to force the fibrillary "nuclei" converted from oligomers to be stable and to be only subjected to depolymerization. The mathematical description of the model is reported in Eq. S1 and Eq. S2 in the master equation formalism. We report as fi and Oi the fibrils and oligomers populations made by i monomers, respectively. θ is the Heaviside theta function, δ is the Dirac delta function, n0 is the minimum nucleus size, nc is the critical size for oligomer conversion into fibrils, m is the Aβ1-40 monomer population. The values of the k constants reflect the importance of the corresponding process (the colour code in Eq. S1 and S2 matches the one in Fig. S4).

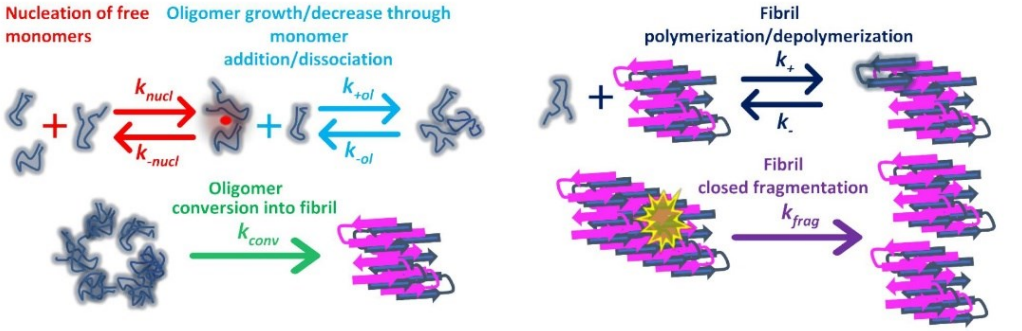

Figure S4: Schematic description of the developed kinetic model for the aggregation of Aβ1-40. The colors of the processes names correspond to the colors of the terms descriptive of the model in Eq. S1 and Eq. S2.

$$\frac{df_i}{dt} = +k_{conv}O_i\theta(i-n_c) - k_+f_im + k_+f_{i-1}m - k_-f_i + k_-f_{i+1} - k_{frag}(i-2n_c+1)f_i\theta(i-2n_c) + 2k_{frag}\sum_{j=i+n_c}^{\infty} f_j \qquad \text{(S1)}$$

$$\frac{dO_i}{dt} = +k_{nucl}\delta(i-n_0)m^{n_0} - k_{-nucl}\delta(i-n_0)n_0O_{n_0} - k_{+ol}O_im + k_{+ol}O_{i-1}m - k_{-ol}iO_i\theta(i-n_0) +$$

$$+k_{-ol}(i+1)O_{i+1}\theta(i-n_0+1) - k_{conv}O_i\theta(i-n_c) \qquad \text{(S2)}$$

As depicted in the equations below, oligomer total population and mass are calculated by summing up all the O_i terms (Eq. S3), while the differential equations for fibril total population and mass are calculated by using the condensed expressions for the summations (Eq. S3). These condensed expressions were obtained from Eq. S1 with calculations similar to the ones performed by Pöschel et al..[4] comparing the experimental time points of monomer depletion with the simulated monomer m(t), calculated by Eq. S5 through the numerical integration of Eq. S3 and Eq. S4. In the equations below, the terms O_{Max} represent the maximum allowed size of oligomers for the numerical solving of the differential equations, theoretically this term can go up to ∞ but in our simulations oligomer population were almost empty after $i = 30$, see Fig. S8B.

$$\frac{dO}{dt} = \sum_{i=n_0}^{O_{Max}} \frac{dO_i}{dt}; \qquad \frac{dO_{crit}}{dt} = \sum_{i=n_c}^{O_{Max}} \frac{dO_i}{dt}; \qquad \frac{dM_O}{dt} = \sum_{i=n_0}^{O_{Max}} i\frac{dO_i}{dt}; \qquad \frac{dM_{O\,crit}}{dt} = \sum_{i=n_c}^{O_{Max}} i\frac{dO_i}{dt} \tag{S3}$$

$$\frac{dF}{dt} = \sum_{i=n_c}^{\infty} \frac{df_i}{dt} = k_{conv}O_{crit} + k_{frag}\left(M_f - F(2n_c+1)\right); \qquad \frac{dM_f}{dt} = \sum_{i=n_c}^{\infty} i\frac{df_i}{dt} = k_{conv}M_{O\,crit} + k_+mF - k_-F \tag{S4}$$

$$m = m_0 - \sum_{i=n_c}^{\infty} if_i - \sum_{i=n_0}^{\infty} iO_i = m_0 - M_f - M_O \tag{S5}$$

The cumulative masses of aggregated species are defined as M_f, M_O, M_{Ocrit}, for the total mass of fibrils, oligomers and oligomers above the critical size (n_c), respectively. This new proposed model contains oligomeric intermediates with different aggregation properties and kinetic constants with respect to fibrils. We put $n_0 = 2$, we considered the smallest oligomer as the dimer and the best fit was achieved using $n_c = 20$ as critical size. In Table S1 we reported the fitted kinetic constants for this model and for the other two model considered in the main text, that one developed for the aggregation of Aβ1-42[2] and that one for Aβ1-40[8] at pH 7.4. The agreement between calculated and experimental values is now optimal also during the lag-time where the monomer concentration is decreasing due to the progressive formation of oligomeric species. In our model, the kinetic constant for the monomer addition to fibrils species (k_+) is an order of magnitude higher than the one for the monomer addition to oligomeric species (k_{+ol}). This difference explains why, once a sufficient amount of large oligomers is converted to fibrils, monomers start to be rapidly consumed while the mass of fibrils rapidly increases producing a sigmoidal behaviour for the monomer consumption kinetics. In the third part of the trend, where most of the peptides are aggregated into fibrils, the process of monomer dissociation becomes relevant and is responsible for the residual amount of monomer still present in solution in the tail of the sigmoidal decrease. The critical size of the oligomer-to-fibril conversion was found to be $n_c = 20$; this number is anyway just an estimate, since reasonably good values were found also for $15<n_c<40$, and we cannot exclude that conversion may begin at even larger sizes.

Parameters	Conversion model	Model Aβ1-40	Model Aβ1-42
k_{nucl} $[M^{-1}s^{-1}]$	$1.25\cdot10^{-6}$	$2.64\cdot10^{-10}$	$1.28\cdot10^{-9}$
k_{-nucl} $[s^{-1}]$	$6.96\cdot10^{-9}$	-	-
k_+ $[M^{-1}s^{-1}]$	$2.83\cdot10^{-1}$	$7.09\cdot10^{-3}$	$6.19\cdot10^{-4}$
k_- $[s^{-1}]$	$5.22\cdot10^{-7}$	$6.11\cdot10^{-21}$	$2.57\cdot10^{-12}$
k_{frag} $[s^{-1}]$	$8.68\cdot10^{-11}$	-	$2.52\cdot10^{-12}$
k_{nucl2} $[M^{-2}s^{-1}]$	-	1.92	6.54
k_{+ol} $[M^{-1}s^{-1}]$	$2.11E\cdot10^{-2}$	-	-
k_{-ol} $[s^{-1}]$	$1.30\cdot10^{-7}$	-	-
k_{conv} $[s^{-1}]$	$1.35\cdot10^{-8}$	-	-
K_{sat} $[M^2]$	-	$9.73\cdot10^{-5}$	-

Table S1: Fitted parameters for the conversion model developed in this work, for the Aβ1-40 model from the work of Meisl, Knowles and co-workers[8] and for the Aβ1-42 model from the works of Knowles, Dobson and co-workers.[2]

3. Test with secondary nucleation active

We repeated the fitting procedure by adding the secondary nucleation term (depicted in the line below) in Eq. S1.

$$+\delta(i-n_2)m^{n_2}\sum_{j=2}^{\infty} jf_j$$

In this term we considered the fibrillary nucleus size $n_2 = 2$, with the meaning that fibril-like dimers are allowed to form on the fibril surface of all the other fibrils. The fitting results are shown in Fig. S5 and the fitted kinetic constants are in Table S2.

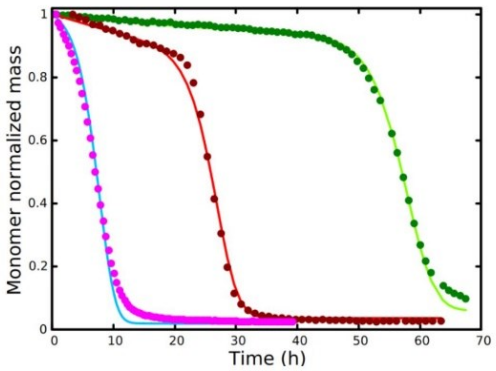

Figure S5: Simulated monomer populations coming from the "conversion" model with secondary nucleation were fitted to the experimental data coming from the integration of the methyl region of 1D solution NMR spectra at different starting monomer concentrations (30, 50 and 100 μM).

Parameters	Conversion Model with secondary nucleation
k_{nucl} $[M^{-1}s^{-1}]$	$1.23 \cdot 10^{-6}$
k_{-nucl} $[s^{-1}]$	$7.87 \cdot 10^{-9}$
k_{+} $[M^{-1}s^{-1}]$	$3.18 \cdot 10^{-1}$
k_{-} $[s^{-1}]$	$5.49 \cdot 10^{-7}$
k_{frag} $[s^{-1}]$	$7.41 \cdot 10^{-11}$
k_{nucl2} $[M^{-2}s^{-1}]$	$5.89 \cdot 10^{-6}$
k_{+ol} $[M^{-1}s^{-1}]$	$2.30 \cdot 10^{-2}$
k_{-ol} $[s^{-1}]$	$1.39 \cdot 10^{-7}$
k_{conv} $[s^{-1}]$	$1.04 \cdot 10^{-8}$

Table S2: Fitted kinetic constants for the conversion model developed in this work with secondary nucleation added. The kinetic constant relative to the secondary surface catalyzed nucleation remains quite smal (see the fitted values for the two-species models in Table 1) in order to fit the NMR data.

4. Including low molecular weight (LMW) oligomers in the fitting

In the first chapter of these Supporting Information we showed how the observed species in the 1D spectrum is essentially the monomeric peptide. Nevertheless, oligomers even up to about 10 units have a molecular weight <50 kDa and should be visible in the NMR spectrum. Thus, we cannot exclude that integrating the methyl region we can include resonances of small oligomeric species. To demonstrate the robustness of the analysis, we repeated the simulation of the oligomer-to-fibril conversion model considering as visible in the integral also LMW oligomeric species until hexamers (species until hexamers should be clearly visible by 1D NMR). We examined two cases: first we repeated the fit using the same constants of Table 1, but including in the simulated curve the LMW oligomers (Figure S6A). Second, we repeated the fit allowing the constant to be adapted (Figure S6B & Table S3). Since these small-size oligomeric species are transient and present in low concentration (at least in our simulations) taking them into account while fitting the NMR data caused only minimal differences in the trend of the calculated curves.

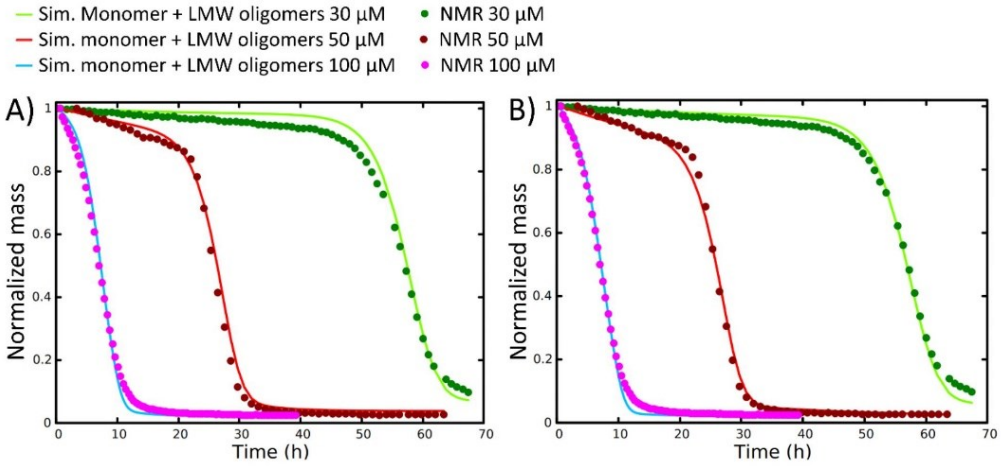

Figure S6: A) Simulated monomer and small oligomer populations (oligomers of size ≤6 and monomers were included) coming from the "conversion" model were fitted to the experimental data coming from the integration of the methyl region of 1D solution NMR spectra at different starting monomer concentrations (30, 50 and 100 µM), the kinetic constants used were the ones of Table 1. B) kinetic constants were optimized to fit monomers and species until hexamers (fitted parameters are present in Table S3).

Parameters	Conversion model with LMW oligomeric species
k_{nucl} $[M^{-1}s^{-1}]$	$1.51 \cdot 10^{-6}$
k_{-nucl} $[s^{-1}]$	$1.53 \cdot 10^{-9}$
k_{+} $[M^{-1}s^{-1}]$	$2.67 \cdot 10^{-1}$
k_{-} $[s^{-1}]$	$1.93 \cdot 10^{-7}$
k_{frag} $[s^{-1}]$	$8.50 \cdot 10^{-11}$
k_{nucl2} $[M^{-2}s^{-1}]$	-
k_{+ol} $[M^{-1}s^{-1}]$	$2.87 \cdot 10^{-2}$
k_{-ol} $[s^{-1}]$	$1.64 \cdot 10^{-7}$
k_{conv} $[s^{-1}]$	$7.32 \cdot 10^{-9}$

Table S3: kinetic constants relative to the fitted data in Figure S6 (right).

5. Populations of the aggregates

On the basis of the fitted constants of Table S1, we back-calculated the relative size of the fibril distribution for the three models (Fig. S8 and Fig. S9). With reference to Figure S7, it results that, for the Aβ1-42 and Aβ1-40 models at the end of the aggregation process of the 50 µM sample (t ~60h), the majority of the fibrils should have a size smaller than 20 monomers, and for the Aβ1-42 model even smaller than 10 monomers (40 kDa). In the trials we made, only the model based on the oligomer-to-fibril conversion predicts the formation of fibrils larger than 433 kDa (>100mers). Indeed, the strong secondary nucleation process of the first two models results in a rapid formation of nucleation seeds during the sigmoidal step that are not able to elongate much because of the depleted monomers in solution. In our conversion model we have not included the secondary nucleation process and the "limited" number of converted fibrils favors their elongation towards higher molecular weights.

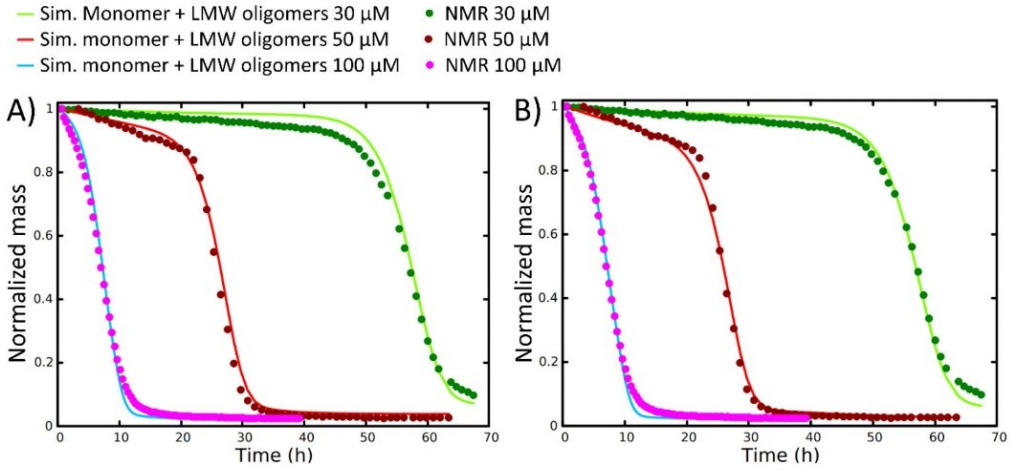

Figure S6: A) Simulated monomer and small oligomer populations (oligomers of size ≤6 and monomers were included) coming from the "conversion" model were fitted to the experimental data coming from the integration of the methyl region of 1D solution NMR spectra at different starting monomer concentrations (30, 50 and 100 µM), the kinetic constants used were the ones of Table 1. B) kinetic constants were optimized to fit monomers and species until hexamers (fitted parameters are present in Table S3).

Parameters	Conversion model with LMW oligomeric species
k_{nucl} $[M^{-1}s^{-1}]$	$1.51 \cdot 10^{-6}$
k_{-nucl} $[s^{-1}]$	$1.53 \cdot 10^{-9}$
k_{+} $[M^{-1}s^{-1}]$	$2.67 \cdot 10^{-1}$
k_{-} $[s^{-1}]$	$1.93 \cdot 10^{-7}$
k_{frag} $[s^{-1}]$	$8.50 \cdot 10^{-11}$
k_{nucl2} $[M^{-2}s^{-1}]$	-
k_{+ol} $[M^{-1}s^{-1}]$	$2.87 \cdot 10^{-2}$
k_{-ol} $[s^{-1}]$	$1.64 \cdot 10^{-7}$
k_{conv} $[s^{-1}]$	$7.32 \cdot 10^{-9}$

Table S3: kinetic constants relative to the fitted data in Figure S6 (right).

5. Populations of the aggregates

On the basis of the fitted constants of Table S1, we back-calculated the relative size of the fibril distribution for the three models (Fig. S8 and Fig. S9). With reference to Figure S7, it results that, for the Aβ1-42 and Aβ1-40 models at the end of the aggregation process of the 50 µM sample (t ~60h), the majority of the fibrils should have a size smaller than 20 monomers, and for the Aβ1-42 model even smaller than 10 monomers (40 kDa). In the trials we made, only the model based on the oligomer-to-fibril conversion predicts the formation of fibrils larger than 433 kDa (>100mers). Indeed, the strong secondary nucleation process of the first two models results in a rapid formation of nucleation seeds during the sigmoidal step that are not able to elongate much because of the depleted monomers in solution. In our conversion model we have not included the secondary nucleation process and the "limited" number of converted fibrils favors their elongation towards higher molecular weights.

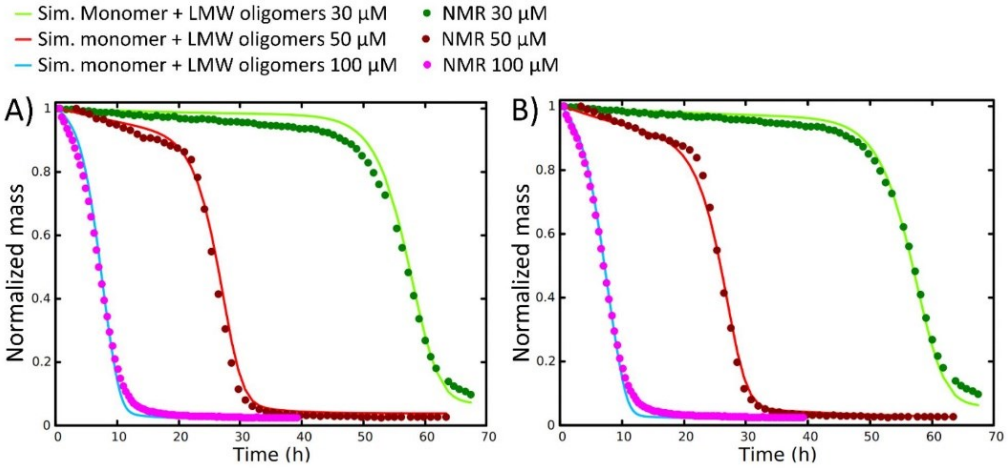

Figure S6: A) Simulated monomer and small oligomer populations (oligomers of size ≤6 and monomers were included) coming from the "conversion" model were fitted to the experimental data coming from the integration of the methyl region of 1D solution NMR spectra at different starting monomer concentrations (30, 50 and 100 µM), the kinetic constants used were the ones of Table 1. B) kinetic constants were optimized to fit monomers and species until hexamers (fitted parameters are present in Table S3).

Parameters	Conversion model with LMW oligomeric species
k_{nucl} $[M^{-1}s^{-1}]$	$1.51 \cdot 10^{-6}$
k_{-nucl} $[s^{-1}]$	$1.53 \cdot 10^{-9}$
k_{+} $[M^{-1}s^{-1}]$	$2.67 \cdot 10^{-1}$
k_{-} $[s^{-1}]$	$1.93 \cdot 10^{-7}$
k_{frag} $[s^{-1}]$	$8.50 \cdot 10^{-11}$
k_{nucl2} $[M^{-2}s^{-1}]$	-
k_{+ol} $[M^{-1}s^{-1}]$	$2.87 \cdot 10^{-2}$
k_{-ol} $[s^{-1}]$	$1.64 \cdot 10^{-7}$
k_{conv} $[s^{-1}]$	$7.32 \cdot 10^{-9}$

Table S3: kinetic constants relative to the fitted data in Figure S6 (right).

5. Populations of the aggregates

On the basis of the fitted constants of Table S1, we back-calculated the relative size of the fibril distribution for the three models (Fig. S8 and Fig. S9). With reference to Figure S7, it results that, for the Aβ1-42 and Aβ1-40 models at the end of the aggregation process of the 50 µM sample (t ~60h), the majority of the fibrils should have a size smaller than 20 monomers, and for the Aβ1-42 model even smaller than 10 monomers (40 kDa). In the trials we made, only the model based on the oligomer-to-fibril conversion predicts the formation of fibrils larger than 433 kDa (>100mers). Indeed, the strong secondary nucleation process of the first two models results in a rapid formation of nucleation seeds during the sigmoidal step that are not able to elongate much because of the depleted monomers in solution. In our conversion model we have not included the secondary nucleation process and the "limited" number of converted fibrils favors their elongation towards higher molecular weights.

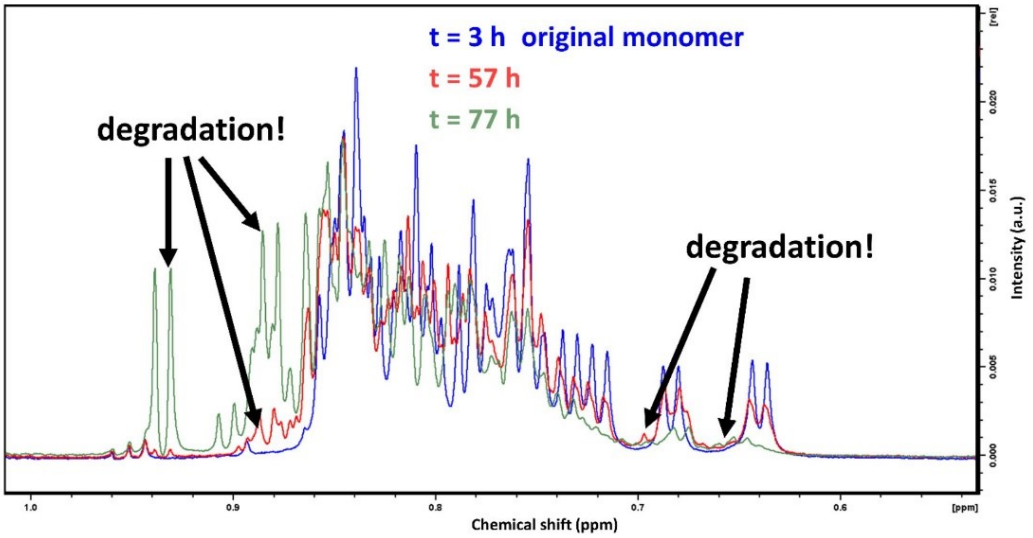

Figure S10: Spectra at different time points of a 40 µM Aβ1-40 sample at 298 K, pH 8.5 in ammonium acetate buffer in absence of EDTA, NaN_3 and protease inhibitors. The growth of sharp peaks near the monomer signals in the methyl region is a hallmark of degradation.

7. Experimental

7.1 AβM1-40 expression and purification

Escherichia Coli BL21(DE3) pLysS cells were transformed with pET-3a(+) vector containing the gene encoding the AβM1-40 peptide gene. The expression was performed using the Marley method.[17] Transformed cells were grown in LB medium until OD600 value reached 0.6-0.8 and, after a centrifugation at 3500 rpm (JA-10, Beckman Coulter), the pellet was exchanged into the M9 minimal medium containing $(^{15}NH_4)_2SO_4$ 1.0 g/L as sole nitrogen source. The same method was used to obtain unlabelled samples. The expression was induced with 1.2 mM Isopropyl-β-D-thiogalactoside and, after 4 hours incubation at 39 °C, cells were harvested at 4000 rpm (JA-10, Beckman Coulter). The pellet was suspended in TRIS 10mM, EDTA 1.0 mM, pH 8.0 buffer and sonicated for 40 minutes (cycle ON 2 seconds, cycle OFF 15 seconds). The suspension was utracentrifuged at 40000 rpm (Type 70 Ti rotor, Beckman Coulter) for 25 min and the pellet was collected, washed with TRIS 10 mM, EDTA 1.0 mM, pH 8.0 buffer and utracentrifuged a second time. Surnatant was discarded and, since Aβ peptides are expressed into inclusion bodies (IBs), a homogenization step with a buffer TRIS 10mM, EDTA 1.0 mM, pH 8.0 containing Urea 8.0 M, until the IBs were fully solubilized, was needed. Purification was performed through anion exchange chromatography in batch with TRIS 10 mM, EDTA 1.0 mM, NaCl 20 mM, 50 mM, 125 mM, 150 mM, 300 mM, 1.0 M at pH 8.0 as elution buffer[18] using DEAE 52 cellulose (DE52) resin. Fractions containing the protein were collected and added to Guanidine hydrochloride 6.0 M. A size-exclusion chromatography step was carried out exploiting the preparative column HiLoad 26/600 Superdex 75 pg with 50 mM $(NH_4)OAc$ pH 8.5 as final buffer [19]. The typical NMR sample conditions counted 30 µM to 100 µM AβM1-40 in 50 mM $(NH_4)OAc$, EDTA 1.0 mM, NaN3 0.2%, Thioflavin-T 5.0 µM (only for samples which were used in parallel with fluorescence), SigmaFast Protease Inhibitor Cocktail (the most abundant component was ABSF 10 µM), 10% D_2O at pH 8.5.

7.2 NMR experiments

Solution NMR experiment were acquired on an Avance III 950 MHz Bruker spectrometer and 700 MHz spectrometer both equipped with a $^1H/^{13}C/^{15}N$ triple resonance cryoprobe. 1D ^1H NMR spectra were acquired with standard direct excitation sequence with excitation sculpting water suppression[20] and a standard 1D NOESY sequence with water presaturation.[21] ^1H π/2 pulse was calibrated at 12.51 µs, 24576 complex points were acquired with an overall acquisition time of 1.95 s, each experiment was acquired accumulating 512 scans with a recycle delay of 1.0 s. Experiments were processed with 65536 complex points and an exponential window function of 0.3 Hz. All the 1D NMR experiments were run at 310 K while the 2D ones at 298 K using new and clean 5 mm glass tubes.

7.3 ThT fluorescence

Fluorescence experiments were performed in a Cary Eclipse fluorescence spectrophotometer (Agilent). The excitation wavelength was set to 450 nm, the emission wavelength to 485 nm and the temperature was kept at 310 K, with emission and excitation slits of 5 nm. ThT final concentration was 5 μM. Fluorescence intensity was recorded every 5 minutes in quiescent conditions. A quartz cuvette with a sample volume 550 μL was used. We preferred the use of a quartz cuvette instead of the more frequently used well plates because it is known that the water/air interface can promote aggregation.[22] In a NMR tube, the ratio between the exposed interface and the sample volume is, in general, smaller than the one of well plate (0.036 mm^{-1} for a typical 5 mm NMR-tube with 550 μL of sample and 0.15-0.14 mm^{-1} for a common flat bottom well with 250 μL of sample). In a quartz cuvette (10 mm x 2 mm) with a sample volume of 550 μL, the exposed interface/sample volume ratio is 0.036 mm^{-1}, equal to the value obtained for the NMR tube.

7.4 Kinetic analysis

Monomer simulated concentrations were compared with the integral values of methyl signals of the 1D spectra (0.67-1.0 ppm) or with the integrals of the signals of QD2 protons of H6, H13 and H14 and QE protons of Y10 of the aromatic regions of 1D-NOESY spectra (6.7-7.1 ppm). While NMR integrals were normalized by simply dividing by the highest value in the 1D series, the ThT fluorescence data were normalized to 1 minus the final plateau value (normalized integral) of the replicate sample in the NMR spectrometer. The kinetic simulations were performed by integrating with Euler method (total points 150000, discrete time interval = 2 s) the kinetic differential equations (Eq. 2 and Eq. 3) describing oligomer and fibril population. The squared differences between the normalized integrals of the methyl signals and the simulated monomer populations were minimized in parallel for different monomer concentrations by optimizing the kinetic constants using a Nelder-Mead minimization algorithm.[23]

7.5 HPLC-Mass Spectrometry

One aliquot of freshly purified and monomerized AβM1-40 (that is the peptide used in manuscript, which corresponds to the Aβ1-40 peptide with an additional methionine in the position 0, and is commonly named AβM1-40 in the text) was frozen (–80 °C) and successively checked by HPLC-MS in a HPLC Dionex Thermo instrument, model Ultimate 3000, coupled to a Thermo LTQ-Orbitrap mass spectrometer via ESI interface. The HPLC column was an Agilent Zorbax 300SB C8 2.1 x 100 mm, 3.5 μm. A gradient elution was performed with two solvents: solvent A H2O with 0.1% formic acid, and solvent B acetonitrile with 0.1% formic acid. The gradient started at time 0.00 minutes with 97% A and 3% of solvent B, reaching at 11.75 min 50% of B, and at time 14.75 min 20% of A and 80% of B. The flow rate was 0.40 mL/min and the injected sample volume was 5 μL. The Mass spectra of the eluted sample were continuously acquired with an Orbitrap system at resolution 30000 (at m/z = 400) in the range of m/z 300–2000. The ESI interface parameters were: Spray voltage 5 kV; Capillary voltage 10 V; Tube lens 60 V; Capillary temperature 280°C. Gas: Sheath gas 10 (arbitrary units), Auxiliary gas 5, Sweep gas 5.

Figure S11 reports the elution profile acquired for m/z comprised between 1000 and 1500. The main peak is composed by the monomeric AβM1-40 with high degree of purity. The figure S12 reports the mass distribution in the central region of the elution peak at times comprised between 8.15 min and 8.48 min. The main patterns, with charges z=4, 5, 6, 7, correspond to the multicharged AβM1-40 peptide. Figure S13 reports the enlarged region around m/z = 893 where is possible to see, together with the isotopic profile of the positive pentacharged AβM1-40 peptide, also the pentacharged isotopic pattern of a small amount of oxidized peptide ($MW_{A\beta M1\text{-}40} + {}^{16}O$), probably related to the oxidation of one of the two methionine residues, (either M0 or M35). Figure S14 reports the enlargement of the tetracharged peptide (m/z= 1116.06) where is possible to recognize also here a small amount of the oxidized peptide (m/z=1120.06) and of the peptide without the initial methionine (–131 uma) (m/z=1083.30). The relative amount of these impurities is estimated on the bases of the integrals of the multi charged patterns: the amount of oxidized peptide is of the order of 5.82% of the not oxidized AβM1-40, while the Aβ1-40 (missing the first methionine) is about 2.82% of the entire peptide.

While the presence, or the missing of the first methionine is expected to have almost no-influence in the aggregation kinetics,[18] the Aβ1-40 peptide fully oxidized at the methionine-35 shows large differences in the aggregation behaviour.[24,25] Nevertheless, since we are in presence of only a very small amount of oxidized species (that could be either M0 or M35) we expect this impurity has no influence in the observed aggregation kinetics.

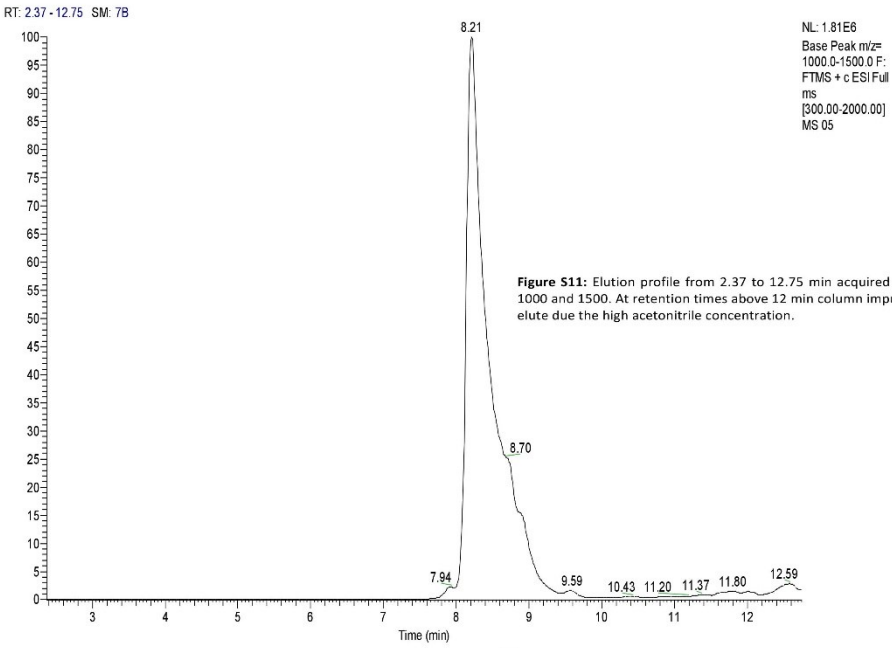

Figure S11: Elution profile from 2.37 to 12.75 min acquired at m/z between 1000 and 1500. At retention times above 12 min column impurities start to be elute due the high acetonitrile concentration.

13

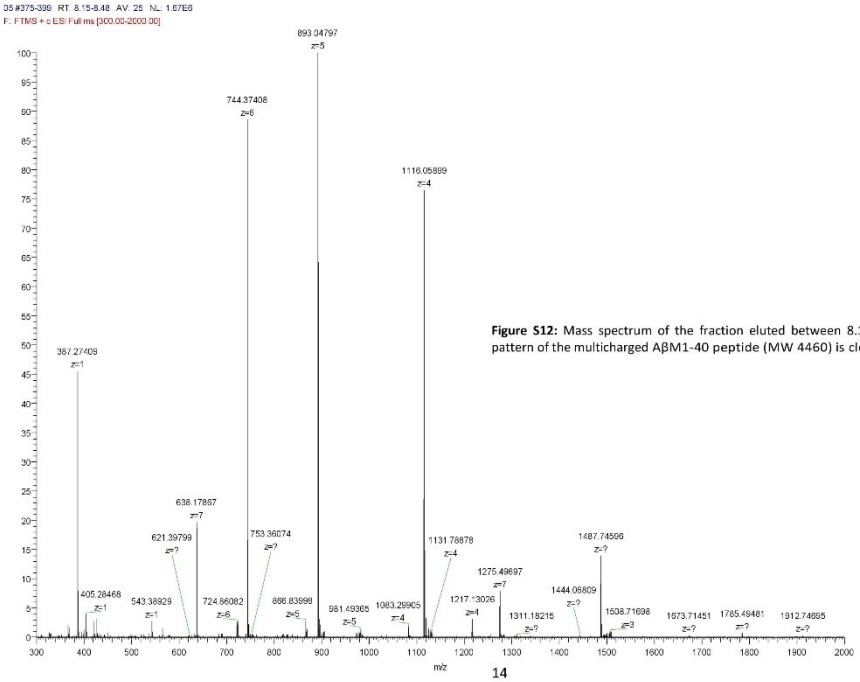

Figure S12: Mass spectrum of the fraction eluted between 8.15 and 8.48 min. The pattern of the multicharged AβM1-40 peptide (MW 4460) is clearly visible.

14

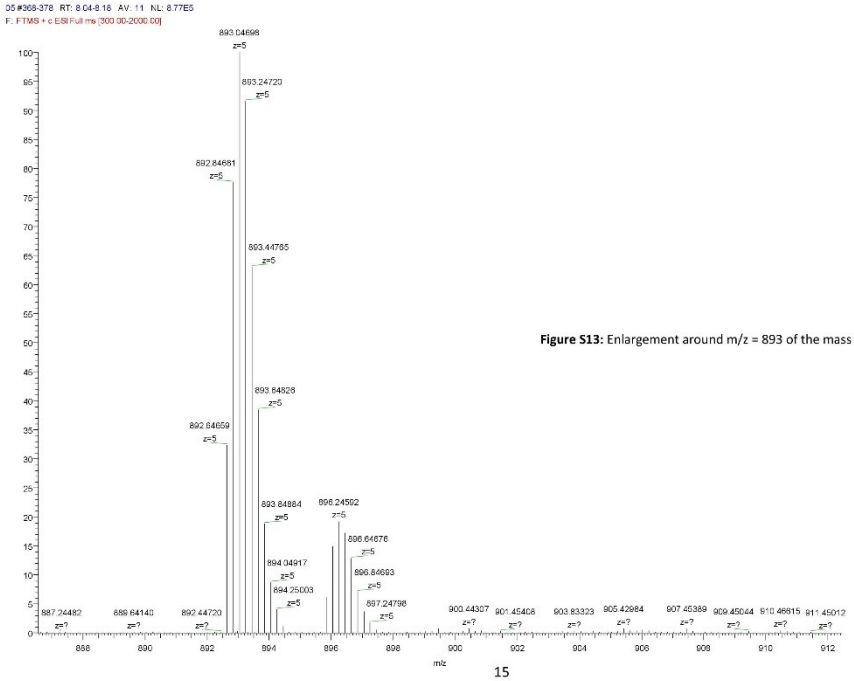

Figure S13: Enlargement around m/z = 893 of the mass spectrum of Figure S12.

15

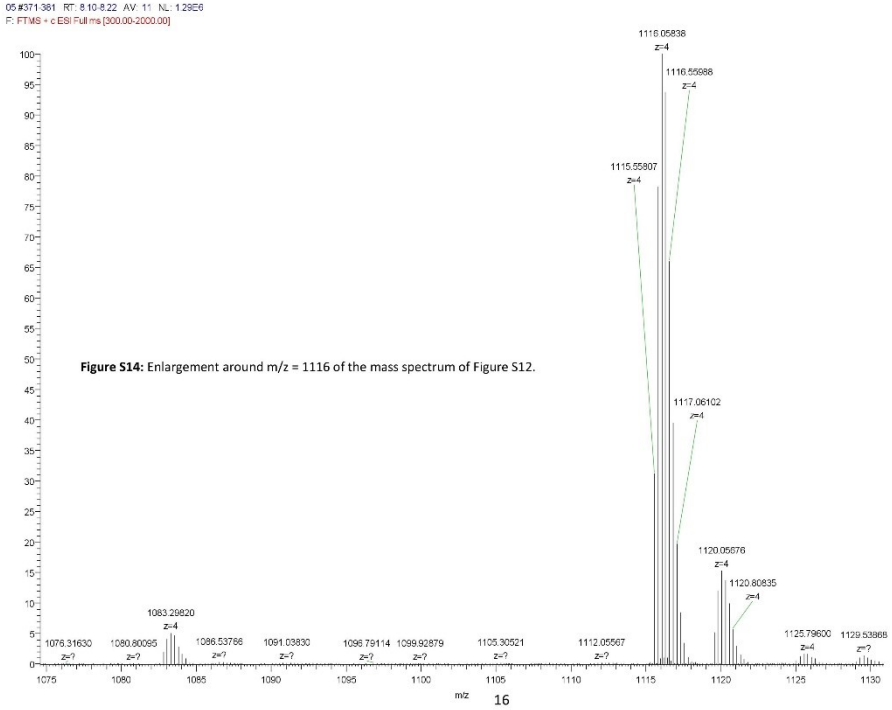

Figure S14: Enlargement around m/z = 1116 of the mass spectrum of Figure S12.

16

References

1 I. Bertini, G. Gallo, M. Korsak, C. Luchinat, J. Mao and E. Ravera, *Chembiochem Eur. J. Chem. Biol.*, 2013, **14**, 1891–1897.
2 S. I. A. Cohen, M. Vendruscolo, M. E. Welland, C. M. Dobson, E. M. Terentjev and T. P. J. Knowles, *J. Chem. Phys.*, 2011, **135**, 065105.
3 F. Ferrone, *Methods Enzymol.*, 1999, **309**, 256–274.
4 T. Pöschel, N. V. Brilliantov and C. Frömmel, *Biophys. J.*, 2003, **85**, 3460–3474.
5 F. Oosawa and M. Kasai, *J. Mol. Biol.*, 1962, **4**, 10–21.
6 S. I. A. Cohen, S. Linse, L. M. Luheshi, E. Hellstrand, D. A. White, L. Rajah, D. E. Otzen, M. Vendruscolo, C. M. Dobson and T. P. J. Knowles, *Proc. Natl. Acad. Sci.*, 2013, **110**, 9758–9763.
7 M. M. Pallitto and R. M. Murphy, *Biophys. J.*, 2001, **81**, 1805–1822.
8 G. Meisl, X. Yang, E. Hellstrand, B. Frohm, J. B. Kirkegaard, S. I. A. Cohen, C. M. Dobson, S. Linse and T. P. J. Knowles, *Proc. Natl. Acad. Sci. U. S. A.*, 2014, **111**, 9384–9389.
9 J. K. Davis and S. S. Sindi, *Appl. Math. Lett.*, 2015, **40**, 97–101.
10 F. Hane and Z. Leonenko, *Biomolecules*, 2014, **4**, 101–116.
11 M. Vestergaard, T. Hamada, M. Morita and M. Takagi, *Curr. Alzheimer Res.*, 2010, **7**, 262–270.
12 L. Hou, I. Kang, R. E. Marchant and M. G. Zagorski, *J. Biol. Chem.*, 2002, **277**, 40173–40176.
13 C. F. Lee, S. Bird, M. Shaw, L. Jean and D. J. Vaux, *J. Biol. Chem.*, 2012, **287**, 38006–38019.
14 B. Morel, L. Varela, A. I. Azuaga and F. Conejero-Lara, *Biophys. J.*, 2010, **99**, 3801–3810.
15 B. Moores, E. Drolle, S. J. Attwood, J. Simons and Z. Leonenko, *PLoS ONE*, , DOI:10.1371/journal.pone.0025954.
16 T. Saido and M. A. Leissring, *Cold Spring Harb. Perspect. Med.*, , DOI:10.1101/cshperspect.a006379.
17 J. Marley, M. Lu and C. Bracken, *J. Biomol. NMR*, 2001, **20**, 71–75.
18 D. M. Walsh, E. Thulin, A. M. Minogue, N. Gustavsson, E. Pang, D. B. Teplow and S. Linse, *FEBS J.*, 2009, **276**, 1266–1281.
19 I. Bertini, L. Gonnelli, C. Luchinat, J. Mao and A. Nesi, *J. Am. Chem. Soc.*, 2011, **133**, 16013–16022.
20 T. L. Hwang and A. J. Shaka, *J. Magn. Reson. A*, 1995, **112**, 275–279.
21 S. Bouatra, F. Aziat, R. Mandal, A. C. Guo, M. R. Wilson, C. Knox, T. C. Bjorndahl, R. Krishnamurthy, F. Saleem, P. Liu, Z. T. Dame, J. Poelzer, J. Huynh, F. S. Yallou, N. Psychogios, E. Dong, R. Bogumil, C. Roehring and D. S. Wishart, *PloS One*, 2013, **8**, e73076.
22 C. Schladitz, E. P. Vieira, H. Hermel and H. Möhwald, *Biophys. J.*, 1999, **77**, 3305–3310.
23 R. O'Neill, *J. R. Stat. Soc. Ser. C Appl. Stat.*, 1971, **20**, 338–345.
24 L. Hou, H. Shao, Y. Zhang, H. Li, N. K. Menon, E. B. Neuhaus, J. M. Brewer, I.-J. L. Byeon, D. G. Ray, M. P. Vitek, T. Iwashita, R. A. Makula, A. B. Przybyla and M. G. Zagorski, *J. Am. Chem. Soc.*, 2004, **126**, 1992–2005.
25 M. Friedemann, E. Helk, A. Tiiman, K. Zovo, P. Palumaa and V. Tõugu, *Biochem. Biophys. Rep.*, 2015, **3**, 94–99.

1.3 Degradation issues

The NMR experiments focused on observing the aggregation kinetics of Aβ1-40 started in 2016, since then there have been several progresses but also problems, mainly connected to the degradation of the samples. Naturally unfolded proteins, like Aβ1-40 are known for the propensity to aggregate but, since they are very exposed to the solvent, they are also subjected to the action of residual proteases present in solution. Indeed, apart from the problems related to uncontrolled aggregation, experimenters working with recombinant naturally unfolded proteins may also face protein degradation issues. The very first experiments related to the work presented in the previous paragraph were conducted at 298 K in an ammonium acetate buffer with 0.02% of sodium azide and a small fraction of *SigmaFast®* EDTA-free protease inhibitors (the ABSF, which is the most concentrated constituent of the tablet, was 10 μM in the final buffer). At first, we did not expect any degradation, we observed the growing of new peaks with a parallel sigmoidal decrease in the ones of the monomer. The sigmoidal decrease of the monomer and the concomitant growing of new species is shown in Fig 1.3.1 for the aromatic region (proton groups were assigned using a ^{1}H -^{1}H TOCSY experiment), but an equivalent behavior was observed for the methyl resonances. The sharpness of these growing peaks made us suspicious about the nature of the grown species, so we immediately performed a Diffusion-Ordered Spectroscopy (DOSY) experiment[38] to obtain information about their size.

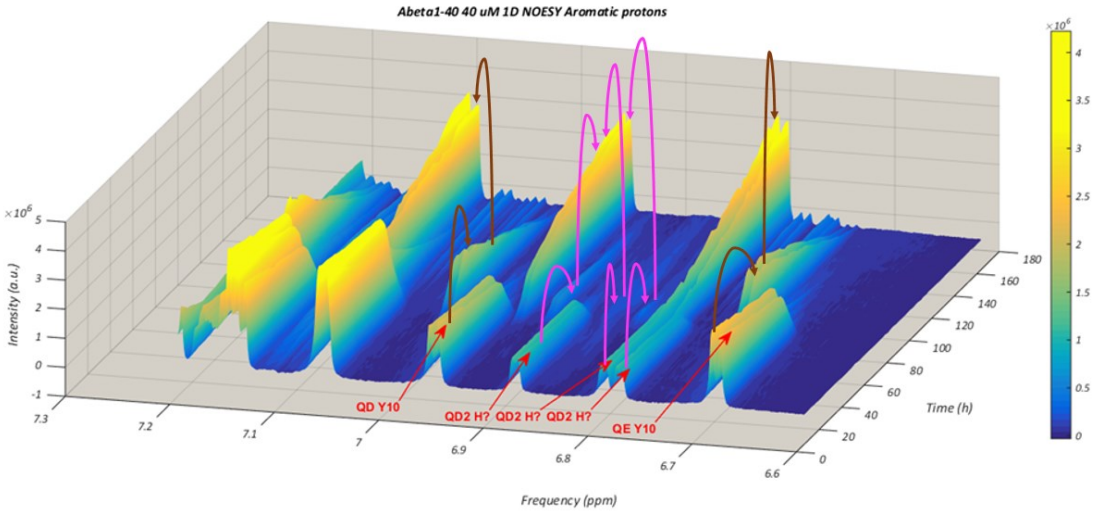

Fig. 1.3.1 Series of 1D ^{1}H NMR spectra of the aromatic region of a 60 μM sample of Aβ1-40 plotted together with MATLAB. Spectra were acquired with a Bruker Avance III 950 MHz NMR spectrometer, in ammonium acetate buffer at pH 8.5. Spectra were binned with AMIX software (bin width = 0.005 ppm) prior to image formation. In this picture the hypothetical degradation pathways for tyrosine and histidine residues are shown.

The results of the DOSY experiment are described in table 1.3.1, gradients were not calibrated prior to the experiments thus, only relative diffusion constants (by using acetate ion diffusion constant as reference) are displayed in for peaks the in the methyl region.

Peak n°	F2 [ppm]	D_{ACE}/D_i
81	0.802	1.5
74	0.809	1.4
73	0.825	1.4
72	0.829	1.4
71	0.833	1.4
70	0.841	1.4
69	0.846	1.5
68	0.853	1.5
67	0.858	1.5
66	0.864	1.4
65	0.879	1.4
64	0.886	1.4
63	0.9	1.4
62	0.907	1.5
61	0.932	1.4
60	0.939	1.4
59	0.954	1.3
58	0.961	1.3
57	1.015	1.2

Table 1.3.1 Apparent diffusion coefficient ratios of methyl peaks measured with the DOSY experiment; the apparent values of the diffusion coefficients were rescaled on the apparent diffusion coefficient of acetate. DOSY experiments were performed on a Bruker Avance III 950 MHz spectrometer at 298 K.

Surprisingly, we measured apparent diffusion coefficients that were comparable to the one of acetate and we understood that the supposed growing species signals were rising from protein fragments and free amino acids. The measured apparent diffusion coefficients for the peaks of the new species were almost comparable the one of acetate. By applying a very simple formula, it is possible to give an estimate of the relative masses of these species by using the Stokes-Einstein relation:

$$D \cong \frac{K_b T}{6\pi\eta r} \propto \frac{1}{r};\ m \propto V \propto r^3 \Longrightarrow \left(\frac{D_{ace}}{D_i}\right)^3 \cong \frac{m_i}{m_{ace}}$$

By using the measured ratios $\frac{D_{ace}}{D_i}$ we found that the majority of the $\frac{m_i}{m_{ace}}$ ratios were smaller than 3.4, indicating that the growing species observed were very small and probably produced by fragments or single amino acids detached from the initial monomer. The single amino acids hypothesis was also in accord with the fact that the QD resonances of three histidines of Aβ1-40 (they are doublets because the sample was ^{15}N labelled) converged in a single doublet at the end of the experiment (Fig. 1.3.1). To understand the causes of the sample degradation, we started performing new experiments with a Bruker 700 MHz NMR

spectrometer equipped with an automatic sample changer. The use of the sample changer allowed us to perform many experiments at the same time at the cost of losing control on temperature (the sample changer was not controlled in temperature). This choice did not allow us to have quantitative information about the aggregation kinetics, but it was necessary to screen many experimental conditions in few sessions and find a way to prevent the degradation of Aβ1-40. The results of this screening are summarized in Table 1.3.2. After having analysed all the data, we understood that there were two main sources of degradation. The most unexpected and relevant one was probably bacterial contamination. Indeed, adding more sodium azide or sterilizing the tube decreased the observed degradation; moreover, bacterial growth is compatible with the sigmoidal line shape observed for the decrease of monomer signals. However, we do not think that bacteria actively degraded the protein but rather the proteases coming from dead bacteria caused the degradation. It is also confirmed by literature that a quantity of 0.02% of sodium azide could be not sufficient to avoid contamination.[39] The second hypothesized cause of degradation was the presence of some metalloproteases that were not blocked by the inhibitors, indeed, by increasing the quantity of EDTA-free inhibitors we did not stop the degradation, while by adding EDTA we completely stopped it (moreover EDTA at high concentration is also quite bactericide). In the end, we decided to use 0.2% of sodium azide with the previous small quantity of inhibitors (*SigmaFast* EDTA-free complete protease inhibitor cocktail) with an ABSF concentration of 10 μM and 1 mM of EDTA. To accelerate the kinetic processes, we also decided to raise the temperature to 310 K. With this new setup, we were finally able to monitor the aggregation process without degradation with shorter experiments in a more reproducible way. These final conditions are the one used in the work shown in paragraph 1.2.

N°	Aβ (µM)	Final state	Features of the (NH_4)OAc buffer
1	40	Fast degradation	NaN_3 0.02% + inib. 10 µM ABSF
2	40	Fast degradation	-
3	40	Poor degradation w/o fibrillation	NaN_3 0.2%
4	40	Poor degradation w/o fibrillation	NaN_3 0.2% + inib. 100 µM ABSF
5	40	Poor degradation w/o fibrillation	NaN_3 0.2% + inib. 10 µM ABSF
6	40	Degradation	inib. 100 µM ABSF
7	40	Degradation	NaN_3 0.02% + inib. 100 µM ABSF
8	40	No degradation w fibrillation	NaN_3 0.02% + inib. 10 µM ABSF + 10 mM EDTA
9	40	No signal w protein precipitation	NaN_3 0.02% + inib. 10 µM ABSF + 1 mM $ZnCl_2$
10	40	Degradation w fibrillation	NaN_3 0.02% + inib. 10 µM ABSF + 100 µM EDTA
11	40	Poor degradation w fibrillation	NaN_3 0.2% + 1mM EDTA
12	40	Fast degradation	NaN_3 0.02% + inib. 10 µM ABSF + 1 µM ZnCl2
13	40	Poor degradation w/o fibrillation	NaN_3 0.02% + inib. 10 µM ABSF + 20 µM ThT
14	40	Poor degradation w fibrillation	NaN_3 0.02% + inib. 10 µM ABSF + 100 µM EDTA + 20 µM ThT
15	40	Poor degradation w fibrillation	1 mM EDTA
16	40	No degradation w fibrillation	10 mM EDTA
17	40	Degradation w fibrillation	NaN_3 0.2% + inib. 10 µM ABSF
18	40	Poor degradation w/o fibrillation	NaN_3 0.02% + inib. 10 µM ABSF (sterilized tube)
19	40	Degradation	NaN_3 0.2% + inib. 10 µM ABSF + 1 mM ZnCl2
20	100	Poor degradation w fibrillation	NaN_3 0.2% + 1 mM EDTA
21	150	No degradation w fibrillation	NaN_3 0.2% + inib. 10 µM ABSF + 1 mM EDTA

Table 1.3.2 Summary of the tests performed with the sample changer installed on a 700 MHz Bruker NMR spectrometer to find the optimal aggregation conditions.

2 Protein aggregation assays for the diagnosis of synucleinopathies

2.1 Overview

Parkinson's disease (PD), the most common neurodegenerative movement disorder, is pathologically characterized by the presence, in selectively vulnerable brain regions, of intracytoplasmic and axonal inclusions, called Lewy bodies (LB) and Lewy neurites, primarily consisting of aggregated α-synuclein (α-syn).[40] Accumulation and formation of insoluble fibrillary α-syn is usually accompanied, both as a cause and a consequence, by the impairment of the autophagy-lysosomal pathways, which represents one of the main routes implicated in the intracellular degradation of α-syn.[26,41–44] The clinical diagnosis of PD can be very difficult in early stages of the disease, when the motor and neurological symptoms are still not present, with high risk of misdiagnosis. The long prodromal phase of PD[45] provides the possibility for early therapeutic intervention, once disease-modifying therapies have been developed, but the lack of biomarkers for early diagnosis and monitoring of disease progression represents a major obstacle to the achievement of this goal. CSF levels of total α-syn,[46] oligomeric α-syn,[47] S129-phosphorylated α-syn,[47] DJ-1,[48] Aβ1-42,[48] tau[49] and lysosomal enzymes[41] are promising candidates for PD biomarkers although they have still low specificity and sensitivity for PD and other synucleinopathies. The understanding of the "prion-like" behavior of α-synuclein provided new perspectives for the development of new diagnostic assays. With respect to this, oligomeric and fibrillary aggregates of α-syn are found to spread from cell to cell both through exosomal pathways and by passive diffusion through CSF;[25,50,51] this evidence makes the detection of misfolded α-syn in CSF a promising strategy for the presymptomatic diagnosis of PD. Two biophysical assays, born for misfolded prion protein (PrP^{Sc}) detection in biological fluids of animals and humans, named PMCA[22] and RT-QuIC,[23] have been recently applied for the detection of prone-to-aggregation α-syn in CSF and brain homogenates.[52–55] These two assays take advantage on the peculiar aggregation kinetics of prion proteins by amplifying small amounts of aggregates in biological fluids at the expense of recombinant monomeric protein added in solution (further details in paragraph 2.2). The PMCA assay was also applied for the detection of misfolded Aβ1-42 in CSF,[56] for the diagnosis of AD, but the existence of

accurate and reliable CSF and blood biomarkers for AD[57–59] diagnosis makes the research on new applications of PMCA and RT-QuIC assays more valuable for PD and other synucleinopathies. The project of "Protein aggregation assays for the diagnosis of synucleinopathies" was born from a collaboration between *CERM* (*Centro Risonanze Magnetiche*) of the *University of Florence* and the *Laboratory of Clinical Neurochemistry* of the *University of Perugia*. The scientists involved in this research have very different academic background (physicians, chemists, biochemists and physicists) but they work together for the ambitious goal of developing assays, based on PMCA and RT-QuIC techniques, for the pre-symptomatic diagnosis of PD. The following chapter of the thesis consists on a review,[24] published in 2018 in *Frontiers in Neurology*. This review contains all the relevant literature about the application of PMCA and RT-QuIC assays for the detection of misfolded α-syn in biological fluids and may serve as an introduction (for the sake of brevity the introduction of paragraph 2.3 is not included) for the unpublished results present in paragraphs 2.3 and 2.4. I would also like to take advantage of this thesis to report two very recent studies in this field that were not included in the review. The first one is the very interesting work of the group of Prof. A. J. Green, which performed a pilot study to evaluate the ability of α-syn RT-QuIC in stratifying PD patients;[60] the second one is a comparative study conducted by the group of Prof. Claudio Soto in collaboration with the group of Prof. A. J. Green in order to validate α-syn PMCA and α-syn RT-QuIC in an independent cohort of patients and control individuals.[61] This last study confirmed the incredible diagnostic potential of these two techniques. The two research groups, considering the similarities of α-syn PMCA and α-syn RT-QuIC agree that the name "*seeding aggregation assays"* (SAA) can group up the two techniques for the future.

2.2 Review on PMCA and RT-QuIC techniques applied for synucleinopathies

frontiers in Neurology

MINI REVIEW
published: 06 June 2018
doi: 10.3389/fneur.2018.00415

Are We Ready for Detecting α-Synuclein Prone to Aggregation in Patients? The Case of "Protein-Misfolding Cyclic Amplification" and "Real-Time Quaking-Induced Conversion" as Diagnostic Tools

Silvia Paciotti[1†], *Giovanni Bellomo*[2†], *Leonardo Gatticchi*[1] *and Lucilla Parnetti*[3*]

[1] Department of Experimental Medicine, University of Perugia, Perugia, Italy, [2] Magnetic Resonance Center (CERM), University of Florence, Sesto Fiorentino, Italy, [3] Laboratory of Clinical Neurochemistry, Department of Medicine, University of Perugia, Perugia, Italy

OPEN ACCESS

Edited by:
Claudio Soto,
University of Texas Health Science Center at Houston, United States

Reviewed by:
Luis Concha-Marambio,
Amprion Inc., United States
Alison Jane Ellen Green,
University of Edinburgh, United Kingdom

***Correspondence:**
Lucilla Parnetti
lucilla.parnetti@unipg.it

[†]These authors have contributed equally to this work.

Specialty section:
This article was submitted to Neurodegeneration, a section of the journal Frontiers in Neurology

Received: 20 March 2018
Accepted: 22 May 2018
Published: 06 June 2018

Citation:
Paciotti S, Bellomo G, Gatticchi L and Parnetti L (2018) Are We Ready for Detecting α-Synuclein Prone to Aggregation in Patients? The Case of "Protein-Misfolding Cyclic Amplification" and "Real-Time Quaking-Induced Conversion" as Diagnostic Tools. Front. Neurol. 9:415. doi: 10.3389/fneur.2018.00415

The accumulation and deposition of α-synuclein aggregates in brain tissue is the main event in the pathogenesis of different neurodegenerative disorders grouped under the term of synucleinopathies. They include Parkinson's disease, dementia with Lewy bodies and multiple system atrophy. To date, the diagnosis of any of these disorders mainly relies on the recognition of clinical symptoms, when the neurodegeneration is already in an advanced phase. In the last years, several efforts have been carried out to develop new diagnostic tools for early diagnosis of synucleinopathies, with special interest to Parkinson's disease. The Protein-Misfolding Cyclic Amplification (PMCA) and the Real-Time Quaking-Induced Conversion (RT-QuIC) are ultrasensitive protein amplification assays for the detection of misfolded protein aggregates. Starting from the successful application in the diagnosis of human prion diseases, these techniques were recently tested for the detection of misfolded α-synuclein in brain homogenates and cerebrospinal fluid samples of patients affected by synucleinopathies. So far, only a few studies on a limited number of samples have been performed to test PMCA and RT-QuIC diagnostic reliability. Neverthless, these assays have shown very high sensitivity and specificity in detecting synucleinopathies even at the pre-clinical stage. Despite the application of PMCA and RT-QuIC for α-synuclein detection in biological fluids is very recent, these techniques seem to have the potential for identifying subjects that will be likely to develop synucleinopathies.

Keywords: PMCA, RT-QuIC, α-synuclein, synucleinopathies, early diagnosis

INTRODUCTION

Protein-Misfolding Cyclic Amplification (PMCA) and Real-Time Quaking-Induced Conversion (RT-QuIC) represent two ultrasensitive protein amplification methods for detecting pathological protein aggregates in patients affected by protein misfolding disorders (1–3). PMCA and RT-QuIC are assays conceptually similar to a polymerase chain reaction (PCR):

a template (protein aggregate) grows at the expense of a substrate (protein monomer) in a cyclic reaction characterized by a growth step followed by an increase in template units. Currently, the need of specific and sensitive early diagnostic tools for synucleinopathies points out the attention on novel approaches. Since α-synuclein (α-syn) follows aggregation mechanisms similar to PrP, PMCA and RT-QuIC assays were tested for the detection of misfolded α-syn in samples of patients affected by synucleinopathies (4–9).

A critical analysis on PMCA and RT-QuIC available data and protocols could help in evaluating whether these techniques could be suitable for the detection of α-syn aggregates in body fluids with high sensitivity and specificity, hopefully at a preclinical stage (4–7). The aim of this review is to provide an overview on existing data on PMCA and RT-QuIC assays, and their possible application for the diagnosis of synucleinopathies.

PMCA and RT-QuIC: A Brief History

The first PMCA protocol was developed by Soto's group in 2001 to detect the misfolded prion protein (PrP^{Sc}) (10). The multiplication of the template units was performed by sonication followed by an incubation phase to let the aggregates grow. These steps were repeated several times in a cyclic process to allow the detection of the misfolded proteins in the samples [e.g., brain homogenates (BH), urine, blood, cerebrospinal fluid (CSF) and saliva]; at the end of the process, proteinase K (PK) digestion and western blot (WB) analysis were used to characterize and recognize the presence of pathological aggregates. The PMCA technique was tested in the subsequent years on biological samples coming from animals and patients affected by transmissible spongiform encephalopathy (11, 12). Atarashi et al., taking advantage on PMCA method, developed the QuIC assay by introducing some variants in the protocol (2, 13, 14). In the QuIC, the PrP^{C} substrate coming from hamsters BH was replaced by recombinant PrP^{C} and sonication was replaced with a vigorous intermittent shaking which promoted seeded aggregation of the monomeric substrate (13). Moreover, the WB analysis was substituted by a real-time monitoring (hence the name RT-QuIC) of the fluorescence emitted by the amyloid-sensitive Thioflavin-T dye (ThT) during the aggregation process (2, 14).

Although PMCA and RT-QuIC are both highly sensitive and specific assays, they showed different accuracy in detecting sporadic and variant Creutzfeldt-Jakob disease (CJD), also depending on the nature of the biological samples analyzed (15–17). The success of RT-QuIC in diagnosing prion diseases, led to test this assay for the detection of synucleinopathies (5–7). For this purpose, an αSyn-PMCA assay, methodologically very similar to a RT-QuIC was also developed by Soto's group (4).

α-Synuclein and Synucleinopathies

α-syn is a small protein (∼14 kDa) largely present in the central nervous system at the pre-synaptic neuronal terminals (18, 19). Although α-syn was discovered almost 30 years ago, the physiological role carried out by this protein is not completely understood. It seems to be involved in the regulation of neurotransmitter release, synaptic plasticity and vesicle trafficking, in brain lipid metabolism, remodeling of the membranes, formation of membrane channels, and modification of their activity (20–23).

α-syn is composed of 140 amino acids and it is characterized by 3 distinct regions: N-terminal, central and C-terminal regions. The N-terminus (1–60 residues) contains seven highly conserved hexameric motifs, which form an amphipathic α-helix structure typical of the lipid binding domain of apolipoproteins (24), while the C-terminus (96–140 residues) contains multiple phosphorylation sites and it is enriched in acidic residues. The central domain of α-syn (61–95 residues), known as the non-amyloid-component (NAC), is highly aggregation-prone and plays a key role in cytotoxicity of α-syn (25–27).

At cellular level, α-syn is predominantly present as unfolded soluble monomer with not well-defined secondary or tertiary structures (28–30). Nevertheless, several factors like post-translational modifications (31–33), oxidative stress (28), fatty acids concentration (34–36), proteolysis (37, 38), phospholipids and metal ions (28, 29) can promote the misfolding of α-syn with the consequent formation of oligomers and amyloid-like fibrils (39, 40). α-syn amyloid-like fibrils are composed of several protofilaments containing cross β-sheet secondary structure in which individual β-strands run perpendicular to the fiber axis (41, 42). The α-syn aggregation kinetics is similar to that of the Aβ peptide (43, 44). It is characterized by an initial lag-phase which reflects the seed formation (nucleation phase) and a subsequent growth phase that culminates in a steady state (45).

Aggregated α-syn is involved in the pathogenesis of different neurodegenerative disorders known as synucleinopathies (46–48), which include Parkinson's disease (PD) (49), dementia with Lewy bodies (DLB) (50) and multiple system atrophy (MSA) (51). Fibrillary α-syn is the major constituent of Lewy bodies (LBs) and Lewy neurites (LNs), which represent the main histopathological hallmarks of PD and DLB (46, 47). Differently, in MSA, aggregated α-syn is found in oligodendrocytes as glial cytoplasmic inclusions (48).

The diagnostic value of α-syn as biomarker of synucleinopathies has been extensively investigated (52–56). Several studies have been performed to measure the levels of α-syn species (total, oligomeric and phosphorylated) in body fluids using different techniques: ELISA (57–60), multiplex immunoassays (61, 62), and Förster's resonance energy transfer (63). The heterogeneity of the applied methods partly justifies some ambiguous outcome obtained so far from the available studies. Furthermore, the lower concentration of the oligomeric/fibrillary α-syn species with respect to the monomeric α-syn form and the complexity to develop selective antibodies having high affinity and avidity to the misfolded α-syn species, make it difficult the detection of these species by using the most common antibodies-based assays (52, 64, 65).

The detection of pathogenic aggregates could help in diagnosis, both in terms of specificity and timeliness of diagnosis, since α-syn aggregation is an early phenomenon preceding the onset of clinical symptoms (66).

RT-QuIC AND PMCA ASSAYS: BASIC CONCEPTS

The RT-QuIC and PMCA techniques are based on the amplification of a preformed quantity of misfolded proteins present in biological fluids or tissue samples. Samples are incubated, at a defined temperature, in a buffer solution containing the monomeric substrate. Preformed aggregates (seeds) work as templates polymerizing at their extremities at the expense of the monomer (**Figure 1A**). By introducing a shaking/sonication step, the grown aggregates are then fragmented to generate more polymerization points (67). Incubation and fragmentation cycles are repeated multiple times to achieve an exponential amplification of the aggregates. Apart from the basic polymerization and fragmentation processes, also surface catalyzed nucleation should be considered in the aggregation kinetics (68). This mechanism consists in the formation of new nuclei of misfolded proteins on the surface of preformed fibrils and it has been recently proposed for PrP^{Sc} (69), Aβ peptides (68, 70), and α-syn (71).

In PMCA, WB analysis is used to detect the amplified PrP^{Sc} (10), while in the RT-QuIC and αSyn-PMCA the detection of the misfolded aggregates is performed by recording the fluorescence of the ThT dye. ThT fluorescence (excitation at 450 nm and emission at 480 nm) is enhanced upon binding to fibrils. Compared to WB, ThT fluorescence assay has the limitation to be sensitive only to fibrillary aggregates rich in cross-beta sheet motifs (72). However, ThT assay in multi-well plates has the advantage to be less time-consuming; moreover, the intermittent shaking can be directly performed inside fluorometers and thus easily automated. The recorded fluorescence of ThT in RT-QuIC and αSyn-PMCA is proportional to the mass of fibrillary aggregates present in the sample and its trend gives information about the aggregation kinetics of the monomer. Fluorescence acquisition allows mapping an aggregation curve describing a lag-phase (time with stationary fluorescence), an exponential phase (increase in fluorescence) and a plateau. A simulated example of an ideal output of a RT-QuIC experiment is shown in **Figure 1B**. The process produces sigmoid-like profiles (73, 74) whose lag-times, slopes and stationary points depend on the experimental conditions (temperature, shaking cycles and strength, pH, buffer, etc.). Particularly, the length of the lag-phase correlates to the amount of seeds in the samples (75). However, since the lag-phase is a threshold value established by the investigator, the t50, named the time necessary to reach the 50% of the maximum fluorescence, is often used as a quantitative and objective measurement of the amplification process. The approximate linear relation between the t50 (or the lag-time) and the logarithm of the seed quantities has been shown for different pathogenic proteins like PrP^{sc} (75) α-syn (4, 7, 76), Aβ1-40 (77), and Aβ1-42 (78). Sometimes, deviations from the ideal lineshape, like multiple inflection points or a decrease of the signal at the end of the reaction are present (6, 79). These abnormalities might be caused by sample heterogeneity (amyloids tend to form a suspension in aqueous solution) or by the entrapment of ThT in large aggregates, respectively (80). Thus, most of the authors prefers to define a lag-phase threshold, in which controls do not exhibit aggregation, while positive samples display an increase in fluorescence intensity that exceed the established threshold (e.g., 5–10 times higher than average baseline fluorescence) (4–7, 75, 81). Apart from the length of the lag-phase, Kang et al. (82) suggested that also differences in amyloid formation rate, ThT fluorescence maxima and integrated area under the curve show discrimination between seeded and unseeded samples, thus these features could be also suitable for αSyn-PMCA and RT-QuIC data analysis.

Protocols

Several physical (temperature and sonication/shaking), chemical (ionic strength, pH, monomer concentration, detergents), and exogenous factors were described to affect α-syn aggregation kinetics (83, 84). The most recent implementations in PMCA and RT-QuIC protocols, specifically applied to the detection of α-syn aggregates for the diagnosis of synucleinopathies, are reported in **Table 1** and discussed below.

αSyn-PMCA and RT-QuIC Substrate

In vitro aggregation assay usually requires large amounts of highly purified monomeric α-syn as reaction substrate for fibrils polymerization. Large quantities of recombinant α-syn are obtained by using *Escherichia coli* cultures. The expressed protein can be purified by different chromatographic procedures (7, 87–89). The purity of α-syn preparations can be evaluated by SDS-PAGE followed by silver staining and then confirmed by mass spectrometry. The quality of the initial α-syn monomer solution is a critical factor in determining the successful application of αSyn-PMCA and RT-QuIC techniques. α-syn monomer solution can be filtered with a 100 kDa cutoff filter device (4) in order to remove any preformed aggregates generated during the purification process. To use the optimal amount of substrate in αSyn-PMCA or RT-QuIC, the concentration of the purified α-syn is assessed by spectrophotometric measurement of absorbance at 280 nm (83, 86).

Temperature, pH, and Buffer Composition

Reaction temperature is one of the most well established factors driving α-syn aggregation (39, 90). Generally, in PMCA or RT-QuIC assay, the temperature is set at 37°C. Thirty-seven degree celsius is compatible with a balance between obtaining a short lag-phase, a stable elongation rate, and a minor evaporation of the sample. Similarly, the decrease of pH values toward the isoelectric point of α-syn (pI = 4.67) contributes to the neutralization of protein net charge, that enhances hydrophobicity and boosts the fibrillization process (91). Moreover, the rate of aggregates formation is enhanced by the increase in ionic strength of the reaction buffer (84).

Interestingly, Shahnawaz et al. reported an inhibitory effect of CSF for α-syn aggregation (4); the causes of this behavior are not yet well understood, although Padayachee et al. observed a similar effect also for Aβ (92). Shahnawaz et al. introduced the buffer with the best results in terms of α-syn aggregation timescales and sensitivity in the presence of CSF. By using this buffer, they were able to reduce significantly the lag-phase for positive samples and to decrease the detection

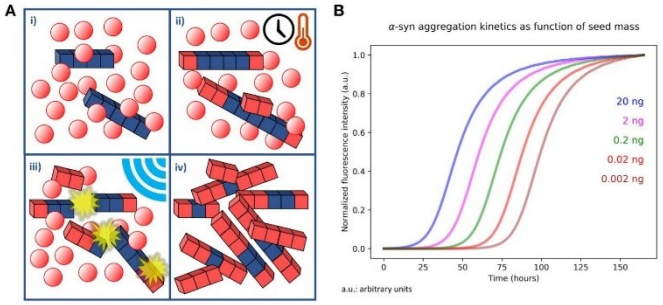

FIGURE 1 | (A) Outline of PMCA and RT-QuIC kinetic assays. (i) An aliquot of tissue homogenate or a biological fluid containing a quantity of aggregates (blue cubes) is dissolved in a buffer containing abundant monomer in solution (red spheres). (ii) The sample is incubated for a defined time at specific temperature. In this phase the preformed aggregates undergo polymerization at their extremities and catalyze the formation of new nuclei on their surfaces. Monomers that undergo misfolding are depicted as red cubes. (iii) The number of available points for polymerization is increased by performing sonication or shaking of the sample, thus fragmenting the fibrils grown in the previous step. The steps (ii) and (iii) are repeated several times. (iv) At the end of the procedure the initial quantity of misfolded and aggregated protein is exponentially amplified at the expense of the monomer present in solution. **(B)** Simulation of a PMCA or RT-QuIC experiment. The simulation was performed by integrating differential equations describing polymerization, secondary catalyzed nucleation and fragmentation kinetics in presence of different quantities (20, 2, 0.2, 0.02, and 0.002 ng) of preformed aggregates (seeds). The simulation consisted in cycles of 30 min in which fragmentation kinetics was kept active only for 1 min (shaking) and turned off for 29 min (incubation). The cycles were repeated for a total time of 150 h. Normalized fluorescence intensity was calculated by considering it proportional to the total mass of fibrillary aggregates formed at a certain time.

sensitivity threshold to femtograms of preformed α-syn seeds. In addition, detergents can be added to reaction buffers to ensure the complete recovery of insoluble amorphous aggregates, together with soluble forms of α-syn fibrils when sonication rather than shaking is used (80, 85). Notably, generation of different species of α-syn aggregates is likely to be linked to different synucleinopathies (93, 94). The application of PMCA protocol allows to amplify brain-derived fibrils with conserved conformation of the original seed (85).

Incubation and Agitation Cycles

The introduction of incubation and agitation cycles played a key-role from the first implementation of PMCA to the last RT-QuIC. In the first version of PMCA (10) the sample was sonicated every hour (five pulses of 1 s each), while in the last RT-QuIC implementations, the sonication step has been replaced by automatic shaking in well plates. Particularly, in the works regarding α-syn, Jung et al. (85), Herva et al. (80), and Roostaee et al. (86) performed sonication on their samples for non-diagnostic applications (**Table 1**). Conversely, Fairfoul et al. (5), Shahnawaz et al. (4), Sano et al. (6), and Groveman et al. (7) applied the following cycles: 1 min shaking (200 rpm) with 14 min of incubation, 60 s shaking (432 rpm) with 2 min of incubation, 40 s shaking (500 rpm) with 29 min of incubation, and 1 min shaking (400 rpm) with 1 min of incubation, respectively. Shaking is one of the most important promoting factors of α-syn aggregation (83, 84). Nevertheless, it is also important to let the sample rest for some time to promote elongation phase: Herva et al. (80) noticed that alternating cycles of incubation and agitation produced a shorter lag-phase compared to continuous agitation. Furthermore, the addition of zirconia/silica beads to the samples increases the fragmentation and diffusion rates and improves the reproducibility of the assay (5, 80, 83).

αSyn-PMCA AND RT-QuIC STUDIES IN DIAGNOSTIC COHORTS

Currently, only a few studies have been performed to test the accuracy of PMCA and RT-QuIC as diagnostic tools for synucleinopathies. Groveman et al. performed RT-QuIC on CSF samples from 29 patients affected by synucleinopathies (12 PD and 17 DLB) and 31 non-synucleinopathy controls [including 16 patients affected by Alzheimer's disease (AD)] (7). Almost all synucleinopathy CSF samples (27 out of 29) gave positive RT-QuIC, whereas none of the non-synucleinopathy controls met the criteria to be considered positive (93% sensitivity and 100% specificity). In this work, an end-point dilution assay was also performed to quantify the RT-QuIC seeding activity in PD ($n = 1$) and DLB ($n = 3$) BH and DLB ($n = 5$) CSF samples by calculating the concentration of seeding activity units (SD_{50}). The estimated SD_{50} was 10^5-10^6 per mg of brain tissue and 4–54 per 15 µl of CSF. These results indicate that CSF samples have seeding activities higher than the minimum detectable level of 1 SD_{50}.

Fairfoul et al. tested the RT-QuIC technology on BH from patients affected by DLB, AD, CJD, and control subjects (5). None of the reactions seeded with BH from patients affected by CJD or AD as well as from control subjects gave positive results after 120 h from the beginning of the reaction. The same group analyzed CSF samples from the OPTIMA (Oxford Project to Investigate Memory and Ageing) cohort with the aim to investigate RT-QuIC sensitivity. The study included patients

TABLE 1 | PMCA and RT-QuIC assays protocols.

Assay	Sample	α-syn concentration (mg/ml)	Buffer	Sonication/ shaking	Temperature (°C)	Beads[a]	Sample volume/ final volume (µl)	Sample readout	Number of samples (cases/ controls)	Sensitivity (%)	Specificity (%)	Detection limits[b]	References
RT-QuIC	BH; CSF	0.1	40 mM phosphate (pH 8.0), 170 mM NaCl, 10 µM ThT, 0.0015% SDS (only for CSF)	1 min (400 rpm) 1 min rest (Sh)	42	6 beads (0.8 mm)	BH 2/100; CSF 15/100	ThT	29/31	93	100	BH 10^{-6}; CSF 0.2 µl α-syn fibrils 100 ag	(7)
RT-QuIC	BH	0.1–0.15	50 mM HEPES (pH 7.5), 10 µM ThT	40 s (432 rpm), 2 min rest (Sh)	40	–	BH (diluted) 5/100	ThT	13/2	–	100	BH 5×10^{-6}	(6)
RT-QuIC	BH; CSF	0.1	100 mM phosphate (pH 8.2), 10 µM ThT	1 min (200 rpm), 14 min rest (Sh)	30	37 ± 3 mg (0.5 mm)	BH (1:20,000) 2/100; CSF 5–15/100	ThT	BH, 15/3; CSF, 102/35	92 DLB, 95 PD	100	–	(5)
PMCA	CSF	0.1 or 1	PBS (pH 7.4) or 100 mM PIPES (pH 6.5), 500 mM NaCl, 5 µM ThT	1 min (500 rpm), 29 min rest (Sh)	37	–	CSF 40/200	ThT	96/97	100 DLB, 88.5 PD, 80 MSA	94–96.9	150 amol	(4)
PMCA	BH	0.723	10 mM Tris (pH 7.5), 150 mM NaCl	10 s every 29 min 50 s (So)	37	10 beads (1 mm)	BH 1%	ThT	1/1	–	–	100 amol	(76)
PMCA	–	0.38 or 1.28	150 mM NaCl, 1% triton X-100, complete protease inhibitors in PBS	20 s every 30 min (So)	37	37 ± 3 mg (1 mm)	200	ThT; WB	–	–	–	–	(80)
PMCA	–	0.28	150 mM NaCl, 1% triton X-100	20 s every 29 min 40 s (So)	37	–	100	ThT; WB	–	–	–	–	(85)
PMCA	–	4.3	Physiological buffer (pH 7.4)	30 s every 10 min (x6) (So); 10 min (300 rpm, x6), 10 h constant, 10 min (x6) (Sh)	37	–	300	WB	–	–	–	–	(86)

BH, brain homogenates; CSF, cerebrospinal fluid; SDS, sodium dodecyl sulfate; HEPES, (4-(2-hydroxyethyl)-1-piperazineethanesulfonic acid); ThT, Thioflavin T; PIPES, Piperazine-N,N′-bis(ethansulfonic acid); PBS, phosphate-buffered saline; So, sonication; Sh, shaking; WB, western blot; DLB, dementia with Lewy bodies; PD, Parkinson's disease; MSA, multiple system atrophy; ag, attograms; amol, attomoles.

[a] *Number/mg of zirconia/silica beads per reaction.*

[b] *Detection limits as reported in the original papers.*

with clinically and neuropathologically confirmed diagnosis of DLB ($n = 12$), PD ($n = 2$), progressive supranuclear palsy (PSP) ($n = 2$), corticobasal degeneration (CBD) ($n = 3$), DLB with AD pathology ($n = 17$), AD with incidental LBs ($n = 13$), pure AD ($n = 30$), and controls ($n = 20$). DLB and PD patients were diagnosed with a 92 and 95% sensitivity, respectively, and with a specificity of 100%. A sensitivity of 65% was observed for patients affected by mixed AD/DLB pathology. None of the patients affected by PSP, CBD, or pure AD, resulted positive to RT-QuIC. A validation study was also carried out in CSF samples from 20 patients diagnosed as PD, 15 control subjects, and 3 subjects affected by rapid eye movement sleep behavior disorder (RBD), a condition at high risk of developing synucleinopathies. Out of 20, 19 PD patients resulted positive (sensitivity = 95%, specificity = 100%), whereas all controls were found negative. The three RBD also showed a positive RT-QuIC response, suggesting the suitability of this approach for early diagnosis.

Shahnawaz et al. used the αSyn-PMCA for detecting α-syn aggregates in CSF samples from different synucleinopathies (PD $n = 76$, DLB $n = 10$, MSA $n = 10$) and other miscellaneous neurological disorders ($n = 97$) including other neurodegenerative diseases not belonging to synucleinopathies (AD, frontotemporal dementia, PSP, ataxia) (4). Out of 76 PD patients, 67 (88%) resulted positive to αSyn-PMCA, whereas 61 out of 65 (94%) patients affected by other neurological disorders resulted negative. Notably, two samples, which were clinically diagnosed as PD after some years from sample collection, resulted positive, indicating the ability of αSyn-PMCA to identify patients even at the prodromal stage. All DLB patients and 8 out of 10 MSA cases were positive at αSyn-PMCA. Out of 14 AD patients, 5 showed positive results. This result might not be considered as false-positive, since α-syn inclusions are not rare in AD brain (95, 96). For this reason, sensitivity and specificity were calculated by excluding AD patients from the analysis. Sensitivity was 88.5% for PD, 100% for DLB and 80% for MSA. Specificity was 94%, reaching 97% when considering patients affected by neurological, but not neurodegenerative, disorders. In this study, the possible correlation between the disease severity and αSyn-PMCA kinetic parameters was also investigated in PD group. A significant negative correlation between the t50 in αSyn-PMCA and the Hoehn and Yahr scale was found. The reduction of the lag-phase suggests the presence of higher concentration of α-syn aggregates in CSF samples of advanced PD cases, thus allowing the monitoring of disease progression. However, these data need to be confirmed in a larger cohort.

Finally, Nishida's group investigated the presence of prion-like seeding of misfolded α-syn in brain samples from patients affected by DLB ($n = 7$), CJD ($n = 3$), Gerstmann-Sträussler-Scheinker disease ($n = 1$), pure AD ($n = 2$), and controls. They found positive results only in BH from DLB patients (6).

CONCLUSION AND FUTURE DIRECTIONS

The first trials of PMCA on PrP^{Sc} date back to 2001 but only recently the αSyn-PMCA and RT-QuIC techniques have been applied for the amplification and detection of aggregates of misfolded α-syn. The positive results obtained from different studies confirm that αSyn-PMCA and RT-QuIC are suitable assays for detecting α-syn aggregates in CSF samples. Furthermore, the high sensitivity and specificity of these techniques in detecting synucleinopathies, even at the pre-clinical stage, suggest their possible use as diagnostic tools. Although the combined analysis of α-syn aggregates with other CSF biomarkers (e.g., Aβ42, t-Tau and p-Tau) can be used in the cases of uncertain diagnosis (e.g., patients affected by mixed AD/DLB pathology), in-depth investigations are still necessary to perform a differential diagnosis among different synucleinopathies. The study of α-syn aggregation kinetics, the characterization of the fibrillary aggregate structure (e.g., by PK digestion, WB analysis, X-ray scattering and solid-state NMR) (42, 97–100), as well as the detection of other soluble or insoluble α-syn non-fibrillary aggregates might be suitable to this purpose (42, 94, 97, 98, 101).

Furthermore, the possibility to assess the SD_{50} in CSF samples, might be relevant for determining prognosis in patients even at the early stage of disease (4, 7). So far, αSyn-PMCA and RT-QuIC has been performed mainly in CSF samples; however, based on the encouraging results obtained in the diagnosis of prion disease in both human and animals (102–107), other more "easily accessible" biological fluids like blood, plasma, serum, urine and saliva, as well as peripheral tissues obtained from biopsies (e.g., nasal mucosa, gastrointestinal tract and skin) have the potential to be used as samples for the detection of misfolded α-syn.

Further developments are still needed to standardize operating procedures, decrease the duration of the assays, and increase their sensitivity. To this purpose, testing different shaking cycles and incubation temperatures will be crucial. The reproducibility of the method has also to be improved in order to uniform lag-times, maximum of fluorescence intensity and lineshapes among replicates.

In conclusion, αSyn-PMCA and RT-QuIC have the potential to be effective tools for the diagnosis of synucleinopathies. It will be exciting to follow the growth of scientific reports about this goal in the next future.

AUTHOR CONTRIBUTIONS

SP, GB, LG, and LP wrote the paper. GB prepared illustrations. LP revised the text.

REFERENCES

1. Soto C. Unfolding the role of protein misfolding in neurodegenerative diseases. *Nat Rev Neurosci.* (2003) **4**:49–60. doi: 10.1038/nrn1007
2. Atarashi R, Sano K, Satoh K, Nishida N. Real-time quaking-induced conversion: a highly sensitive assay for prion detection. *Prion* (2011) **5**:150–3. doi: 10.4161/pri.5.3.16893
3. Properzi F, Pocchiari M. Identification of misfolded proteins in body fluids for the diagnosis of prion diseases. *Int J Cell Biol.* (2013) **2013**:839329. doi: 10.1155/2013/839329
4. Shahnawaz M, Tokuda T, Waragai M, Mendez N, Ishii R, Trenkwalder C, et al. Development of a biochemical diagnosis of parkinson disease by detection of α-synuclein misfolded aggregates in cerebrospinal fluid. *JAMA Neurol.* (2017) **74**:163–72. doi: 10.1001/jamaneurol.2016.4547

5. Fairfoul G, McGuire LI, Pal S, Ironside JW, Neumann J, Christie S, et al. Alpha-synuclein RT-QuIC in the CSF of patients with alpha-synucleinopathies. *Ann Clin Transl Neurol.* (2016) **3**:812–8. doi: 10.1002/acn3.338
6. Sano K, Atarashi R, Satoh K, Ishibashi D, Nakagaki T, Iwasaki Y, et al. Prion-like seeding of misfolded α-synuclein in the brains of dementia with Lewy body patients in RT-QUIC. *Mol Neurobiol.* (2017) **55**:3916–30. doi: 10.1007/s12035-017-0624-1
7. Groveman BR, Orrù CD, Hughson AG, Raymond LD, Zanusso G, Ghetti B, et al. Rapid and ultra-sensitive quantitation of disease-associated α-synuclein seeds in brain and cerebrospinal fluid by αSyn RT-QuIC. *Acta Neuropathol Commun.* (2018) **6**:7. doi: 10.1186/s40478-018-0508-2
8. Bernis ME, Babila JT, Breid S, Wüsten KA, Wüllner U, Tamgüney G. Prion-like propagation of human brain-derived alpha-synuclein in transgenic mice expressing human wild-type alpha-synuclein. *Acta Neuropathol Commun.* (2015) **3**:75. doi: 10.1186/s40478-015-0254-7
9. Tamgüney G, Korczyn AD. A critical review of the prion hypothesis of human synucleinopathies. *Cell Tissue Res.* (2017). doi: 10.1007/s00441-017-2712-y. [Epub ahead of print].
10. Saborio GP, Permanne B, Soto C. Sensitive detection of pathological prion protein by cyclic amplification of protein misfolding. *Nature* (2001) **411**:810–3. doi: 10.1038/35081095
11. Soto C, Anderes L, Suardi S, Cardone F, Castilla J, Frossard M-J, et al. Pre-symptomatic detection of prions by cyclic amplification of protein misfolding. *FEBS Lett.* (2005) **579**:638–42. doi: 10.1016/j.febslet.2004.12.035
12. Haley NJ, Seelig DM, Zabel MD, Telling GC, Hoover EA. Detection of CWD prions in urine and saliva of deer by transgenic mouse bioassay. *PLoS ONE* (2009) **4**:e4848. doi: 10.1371/journal.pone.0004848
13. Atarashi R, Wilham JM, Christensen L, Hughson AG, Moore RA, Johnson LM, et al. Simplified ultrasensitive prion detection by recombinant PrP conversion with shaking. *Nat Methods* (2008) **5**:211–2. doi: 10.1038/nmeth0308-211
14. Atarashi R, Satoh K, Sano K, Fuse T, Yamaguchi N, Ishibashi D, et al. Ultrasensitive human prion detection in cerebrospinal fluid by real-time quaking-induced conversion. *Nat Med.* (2011) **17**:175–8. doi: 10.1038/nm.2294
15. Orrù CD, Groveman BR, Hughson AG, Manca M, Raymond LD, Raymond GJ, et al. RT-QuIC assays for prion disease detection and diagnostics. *Methods Mol Biol.* (2017) **1658**:185–203. doi: 10.1007/978-1-4939-7244-9_14
16. Rubenstein R, Chang B. Re-assessment of PrP(Sc) distribution in sporadic and variant CJD. *PLoS ONE* (2013) **8**:e66352. doi: 10.1371/journal.pone.0066352
17. Henderson DM, Manca M, Haley NJ, Denkers ND, Nalls AV, Mathiason CK, et al. Rapid antemortem detection of CWD prions in deer saliva. *PLoS ONE* (2013) **8**:e74377. doi: 10.1371/journal.pone.0074377
18. Jakes R, Spillantini MG, Goedert M. Identification of two distinct synucleins from human brain. *FEBS Lett.* (2001) **345**:27–32. doi: 10.1016/0014-5793(94)00395-5
19. Spinelli KJ, Taylor JK, Osterberg VR, Churchill MJ, Pollock E, Moore C, et al. Presynaptic alpha-synuclein aggregation in a mouse model of Parkinson's disease. *J Neurosci.* (2014) **34**:2037–50. doi: 10.1523/JNEUROSCI.2581-13.2014
20. Maroteaux L, Scheller RH. The rat brain synucleins; family of proteins transiently associated with neuronal membrane. *Mol Brain Res.* (1991) **11**:335–43. doi: 10.1016/0169-328X(91)90043-W
21. Marques O, Outeiro TF. Alpha-synuclein: from secretion to dysfunction and death. *Cell Death Dis.* (2012) **3**:e350. doi: 10.1038/cddis.2012.94
22. Varkey J, Isas JM, Mizuno N, Jensen MB, Bhatia VK, Jao CC, et al. Membrane curvature induction and tubulation are common features of synucleins and apolipoproteins. *J Biol Chem.* (2010) **285**:32486–93. doi: 10.1074/jbc.M110.139576
23. Ottolini D, Calì T, Szabò I, Brini M. Alpha-synuclein at the intracellular and the extracellular side: functional and dysfunctional implications. *Biol Chem.* (2017) **398**:77–100. doi: 10.1515/hsz-2016-0201
24. Clayton DF, George JM. The synucleins: a family of proteins involved in synaptic function, plasticity, neurodegeneration and disease. *Trends Neurosci.* (1998) **21**:249–54. doi: 10.1016/S0166-2236(97)01213-7
25. Luk KC, Song C, O'Brien P, Stieber A, Branch JR, Brunden KR, et al. Exogenous α-synuclein fibrils seed the formation of Lewy body-like intracellular inclusions in cultured cells. *Proc Natl Acad Sci USA.* (2009) **106**:20051–56. doi: 10.1073/pnas.0908005106
26. Han H, Weinreb PH, Lansbury PT. The core Alzheimer's peptide NAC forms amyloid fibrils which seed and are seeded by β-amyloid: is NAC a common trigger or target in neurodegenerative disease? *Cell Chem Biol.* (1995) **2**:163–9. doi: 10.1016/1074-5521(95)90071-3
27. Uéda K, Fukushima H, Masliah E, Xia Y, Iwai A, Yoshimoto M, et al. Molecular cloning of cDNA encoding an unrecognized component of amyloid in Alzheimer disease. *Proc Natl Acad Sci USA.* (1993) **90**:11282–6. doi: 10.1073/pnas.90.23.11282
28. Hashimoto M, Hsu LJ, Xia Y, Takeda A, Sisk A, Sundsmo M, et al. Oxidative stress induces amyloid-like aggregate formation of NACP/alpha-synuclein *in vitro*. *Neuroreport* (1999) **10**:717–21. doi: 10.1097/00001756-199903170-00011
29. Weinreb PH, Zhen W, Poon AW, Conway KA, Lansbury PT. NACP, a protein implicated in alzheimer's disease and learning, is natively unfolded. *Biochemistry* (1996) **35**:13709–15. doi: 10.1021/bi961799n
30. Theillet FX, Binolfi A, Bekei B, Martorana A, Rose HM, Stuiver M, et al. Structural disorder of monomeric α-synuclein persists in mammalian cells. *Nature* (2016) **530**:45–50. doi: 10.1038/nature16531
31. Ruzafa D, Hernandez-Gomez YS, Bisello G, Broersen K, Morel B, Conejero-Lara F. The influence of N-terminal acetylation on micelle-induced conformational changes and aggregation of α-Synuclein. *PLoS ONE* (2017) **12**:e0178576. doi: 10.1371/journal.pone.0178576
32. Andringa G, Lam KY, Chegary M, Wang X, Chase TN, Bennett MC. Tissue transglutaminase catalyzes the formation of alpha-synuclein crosslinks in Parkinson's disease. *FASEB J.* (2004) **18**:932–4. doi: 10.1096/fj.03-0829fje
33. Paleologou KE, Oueslati A, Shakked G, Rospigliosi CC, Kim H-Y, Lamberto GR, et al. Phosphorylation at S87 is enhanced in synucleinopathies, inhibits α-synuclein oligomerization, and influences synuclein-membrane interactions. *J Neurosci.* (2010) **30**:3184–98. doi: 10.1523/JNEUROSCI.5922-09.2010
34. Takeda A, Hashimoto M, Mallory M, Sundsumo M, Hansen L, Sisk A, et al. Abnormal distribution of the non-Abeta component of Alzheimer's disease amyloid precursor/alpha-synuclein in Lewy body disease as revealed by proteinase K and formic acid pretreatment. *Lab Invest.* (1998) **78**:1169–77.
35. Perrin RJ, Woods WS, Clayton DF, George JM. Exposure to long chain polyunsaturated fatty acids triggers rapid multimerization of synucleins. *J Biol Chem.* (2001) **276**:41958–62. doi: 10.1074/jbc.M105022200
36. Sharon R, Bar-Joseph I, Frosch MP, Walsh DM, Hamilton JA, Selkoe DJ. The formation of highly soluble oligomers of alpha-synuclein is regulated by fatty acids and enhanced in Parkinson's disease. *Neuron* (2003) **37**:583–95. doi: 10.1016/S0896-6273(03)00024-2
37. Li W, West N, Colla E, Pletnikova O, Troncoso JC, Marsh L, et al. Aggregation promoting C-terminal truncation of alpha-synuclein is a normal cellular process and is enhanced by the familial Parkinson's disease-linked mutations. *Proc Natl Acad Sci USA.* (2005) **102**:2162–7. doi: 10.1073/pnas.0406976102
38. Dufty BM, Warner LR, Hou ST, Jiang SX, Gomez-Isla T, Leenhouts KM, et al. Calpain-cleavage of alpha-synuclein: connecting proteolytic processing to disease-linked aggregation. *Am J Pathol.* (2007) **170**:1725–38. doi: 10.2353/ajpath.2007.061232
39. Uversky VN, Li J, Fink AL. Evidence for a partially folded intermediate in alpha-synuclein fibril formation. *J Biol Chem.* (2001) **276**:10737–44. doi: 10.1074/jbc.M010907200
40. Volles MJ, Lansbury PT. Zeroing in on the pathogenic form of alpha-synuclein and its mechanism of neurotoxicity in Parkinson's disease. *Biochemistry* (2003) **42**:7871–8. doi: 10.1021/bi030086j
41. Serpell LC, Berriman J, Jakes R, Goedert M, Crowther RA. Fiber diffraction of synthetic alpha-synuclein filaments shows amyloid-like cross-beta conformation. *Proc Natl Acad Sci USA.* (2000) **97**:4897–4902. doi: 10.1073/pnas.97.9.4897
42. Vilar M, Chou HT, Lührs T, Maji SK, Riek-Loher D, Verel R, et al. The fold of alpha-synuclein fibrils. *Proc Natl Acad Sci USA.* (2008) **105**:8637–42. doi: 10.1073/pnas.0712179105

43. Lomakin A, Teplow DB, Kirschner DA, Benedek GB. Kinetic theory of fibrillogenesis of amyloid beta-protein. *Proc Natl Acad Sci USA*. (1997) **94**:7942–7.
44. Naiki H, Gejyo F. Kinetic analysis of amyloid fibril formation. *Methods Enzymol* (1999) **309**:305–18.
45. Wood SJ, Wypych J, Steavenson S, Louis JC, Citron M, Biere AL. alpha-synuclein fibrillogenesis is nucleation-dependent. Implications for the pathogenesis of Parkinson's disease. *J Biol Chem.* (1999) **274**:19509–12.
46. Spillantini MG, Schmidt ML, Lee VM, Trojanowski JQ, Jakes R, Goedert M. Alpha-synuclein in Lewy bodies. *Nature* (1997) **388**:839–40. doi: 10.1038/42166
47. Spillantini MG, Crowther RA, Jakes R, Hasegawa M, Goedert M. alpha-Synuclein in filamentous inclusions of Lewy bodies from Parkinson's disease and dementia with Lewy bodies. *Proc Natl Acad Sci USA.* (1998) **95**:6469–73.
48. Tu PH, Galvin JE, Baba M, Giasson B, Tomita T, Leight S, et al. Glial cytoplasmic inclusions in white matter oligodendrocytes of multiple system atrophy brains contain insoluble alpha-synuclein. *Ann Neurol.* (1998) **44**:415–22. doi: 10.1002/ana.410440324
49. Poewe W, Seppi K, Tanner CM, Halliday GM, Brundin P, Volkmann J, et al. Parkinson disease. *Nat Rev Dis Primer* (2017) **3**:17013. doi: 10.1038/nrdp.2017.13
50. McKeith IG, Boeve BF, Dickson DW, Halliday G, Taylor JP, Weintraub D, et al. Diagnosis and management of dementia with Lewy bodies: fourth consensus report of the DLB consortium. *Neurology* (2017) **89**:88–100. doi: 10.1212/WNL.0000000000004058
51. Whittaker HT, Qui Y, Bettencourt C, Houlden H. Multiple system atrophy: genetic risks and alpha-synuclein mutations. *F1000Research* (2017) **6**:2072. doi: 10.12688/f1000research.12193.1
52. Parnetti L, Cicognola C, Eusebi P, Chiasserini D. Value of cerebrospinal fluid α-synuclein species as biomarker in Parkinson's diagnosis and prognosis. *Biomark Med.* (2016) **10**:35–49. doi: 10.2217/bmm.15.107
53. Farotti L, Paciotti S, Tasegian A, Eusebi P, Parnetti L. Discovery, validation and optimization of cerebrospinal fluid biomarkers for use in Parkinson's disease. *Expert Rev Mol Diagn.* (2017) **17**:771–80. doi: 10.1080/14737159.2017.1341312
54. Simonsen AH, Kuiperij B, El-Agnaf OMA, Engelborghs S, Herukka SK, Parnetti L, et al. The utility of α-synuclein as biofluid marker in neurodegenerative diseases: a systematic review of the literature. *Biomark Med.* (2016) **10**:19–34. doi: 10.2217/BMM.14.105
55. Visanji NP, Mollenhauer B, Beach TG, Adler CH, Coffey CS, Kopil CM, et al. The Systemic Synuclein Sampling Study: toward a biomarker for Parkinson's disease. *Biomark Med.* (2017) **11**:359–68. doi: 10.2217/bmm-2016-0366
56. Shah A, Hiew KW, Han P, Parsons RB, Chang R, Legido-Quigley C. Alpha-synuclein in bio fluids and tissues as a potential biomarker for Parkinson's disease. *Alzheimers Park Dement.* (2017) **2**.
57. Compta Y, Valente T, Saura J, Segura B, Iranzo Á, Serradell M, et al. Correlates of cerebrospinal fluid levels of oligomeric- and total-α-synuclein in premotor, motor and dementia stages of Parkinson's disease. *J Neurol.* (2015) **262**:294–306. doi: 10.1007/s00415-014-7560-z
58. Hall S, Surova Y, Öhrfelt A, Zetterberg H, Lindqvist D, Hansson O. CSF biomarkers and clinical progression of Parkinson disease. *Neurology* (2015) **84**:57–63. doi: 10.1212/WNL.0000000000001098
59. Førland MG, Öhrfelt A, Oftedal LS, Tysnes OB, Larsen JP, Blennow K, et al. Validation of a new assay for α-synuclein detection in cerebrospinal fluid. *Clin Chem Lab Med.* (2017) **55**:254–60. doi: 10.1515/cclm-2016-0409
60. Magdalinou NK, Paterson RW, Schott JM, Fox NC, Mummery C, Blennow K, et al. A panel of nine cerebrospinal fluid biomarkers may identify patients with atypical parkinsonian syndromes. *J Neurol Neurosurg Psychiatry* (2015) **86**:1240–7. doi: 10.1136/jnnp-2014-309562
61. Wang Y, Shi M, Chung KA, Zabetian CP, Leverenz JB, Berg D, et al. Phosphorylated α-synuclein in Parkinson's disease. *Sci Transl Med.* (2012) **4**:121ra20. doi: 10.1126/scitranslmed.3002566
62. Hall S, Öhrfelt A, Constantinescu R, Andreasson U, Surova Y, Bostrom F, et al. Accuracy of a panel of 5 cerebrospinal fluid biomarkers in the differential diagnosis of patients with dementia and/or parkinsonian disorders. *Arch Neurol.* (2012) **69**:1445–52. doi: 10.1001/archneurol.2012.1654
63. Bidinosti M, Shimshek DR, Mollenhauer B, Marcellin D, Schweizer T, Lotz GP, et al. Novel one-step immunoassays to quantify α-synuclein: applications for biomarker development and high-throughput screening. *J Biol Chem.* (2012) **287**:33691–705. doi: 10.1074/jbc.M112.379792
64. Eusebi P, Giannandrea D, Biscetti L, Abraha I, Chiasserini D, Orso M, et al. Diagnostic utility of CSF α-synuclein species in Parkinson's disease: protocol for a systematic review and meta-analysis. *BMJ Open* (2016) **6**:e011113. doi: 10.1136/bmjopen-2016-011113
65. Mollenhauer B, El-Agnaf OMA, Marcus K, Trenkwalder C, Schlossmacher MG. Quantification of α-synuclein in cerebrospinal fluid as a biomarker candidate: review of the literature and considerations for future studies. *Biomark Med.* (2010) **4**:683–9. doi: 10.2217/bmm.10.90
66. Braak H, Bohl JR, Müller CM, Rüb U, de Vos RAI, Del Tredici K. Stanley Fahn Lecture 2005: the staging procedure for the inclusion body pathology associated with sporadic Parkinson's disease reconsidered. *Mov Disord* (2006) **21**:2042–51. doi: 10.1002/mds.21065
67. Pöschel T, Brilliantov NV, Frömmel C. Kinetics of prion growth. *Biophys J.* (2003) **85**:3460–74. doi: 10.1016/S0006-3495(03)74767-5
68. Linse S. Monomer-dependent secondary nucleation in amyloid formation. *Biophys Rev.* (2017) **9**:329–38. doi: 10.1007/s12551-017-0289-z
69. Orgel LE. Prion replication and secondary nucleation. *Chem Biol.* (1996) **3**:413–4. doi: 10.1016/S1074-5521(96)90087-3
70. Meisl G, Kirkegaard JB, Arosio P, Michaels TCT, Vendruscolo M, Dobson CM, et al. Molecular mechanisms of protein aggregation from global fitting of kinetic models. *Nat Protoc.* (2016) **11**:252. doi: 10.1038/nprot.2016.010
71. Gaspar R, Meisl G, Buell AK, Young L, Kaminski CF, Knowles TPJ, et al. Secondary nucleation of monomers on fibril surface dominates α-synuclein aggregation and provides autocatalytic amyloid amplification. *Q Rev Biophys.* (2017) **50**:e6. doi: 10.1017/S0033583516000172
72. Biancalana M, Koide S. Molecular mechanism of Thioflavin-T binding to amyloid fibrils. *Biochim Biophys Acta* (2010) **1804**:1405–12. doi: 10.1016/j.bbapap.2010.04.001
73. Ferrone F. Analysis of protein aggregation kinetics. *Methods Enzymol.* (1999) **309**:256–74.
74. Cohen SIA, Vendruscolo M, Welland ME, Dobson CM, Terentjev EM, Knowles TPJ. Nucleated polymerization with secondary pathways. I. Time evolution of the principal moments. *J Chem Phys.* (2011) **135**:065105. doi: 10.1063/1.3608916
75. Henderson DM, Davenport KA, Haley NJ, Denkers ND, Mathiason CK, Hoover EA. Quantitative assessment of prion infectivity in tissues and body fluids by real-time quaking-induced conversion. *J Gen Virol.* (2015) **96**:210–9. doi: 10.1099/vir.0.069906-0
76. Becker K, Wang X, Vander Stel K, Chu Y, Kordower J, Ma J. Detecting alpha synuclein seeding activity in formaldehyde-fixed MSA patient tissue by PMCA. *Mol Neurobiol.* (2018). doi: 10.1007/s12035-018-1007-y. [Epub ahead of print].
77. Du D, Murray AN, Cohen E, Kim HE, Simkovsky R, Dillin A, et al. A Kinetic aggregation assay enabling selective and sensitive Aβ amyloid quantification in cells and tissues. *Biochemistry* (2011) **50**:1607–17. doi: 10.1021/bi1013744
78. Arosio P, Cukalevski R, Frohm B, Knowles TPJ, Linse S. Quantification of the concentration of Aβ42 propagons during the lag phase by an amyloid chain reaction assay. *J Am Chem Soc.* (2014) **136**:219–25. doi: 10.1021/ja408765u
79. Peden AH, McGuire LI, Appleford NEJ, Mallinson G, Wilham JM, Orrú CD, et al. Sensitive and specific detection of sporadic Creutzfeldt–Jakob disease brain prion protein using real-time quaking-induced conversion. *J Gen Virol.* (2012) **93**:438–49. doi: 10.1099/vir.0.033365-0
80. Herva ME, Zibaee S, Fraser G, Barker RA, Goedert M, Spillantini MG. Anti-amyloid compounds inhibit α-synuclein aggregation induced by protein misfolding cyclic amplification (PMCA). *J Biol Chem.* (2014) **289**:11897–905. doi: 10.1074/jbc.M113.542340
81. Salvadores N, Shahnawaz M, Scarpini E, Tagliavini F, Soto C. Detection of misfolded Aβ oligomers for sensitive biochemical diagnosis of Alzheimer's disease. *Cell Rep.* (2014) **7**:261–8. doi: 10.1016/j.celrep.2014.02.031
82. Kang HE, Mo Y, Abd Rahim R, Lee HM, Ryou C. Prion diagnosis: application of real-time quaking-induced conversion. *BioMed Res Int.* (2017) **2017**:5413936. doi: 10.1155/2017/5413936
83. Giehm L, Otzen DE. Strategies to increase the reproducibility of protein fibrillization in plate reader assays. *Anal Biochem.* (2010) **400**:270–81. doi: 10.1016/j.ab.2010.02.001

84. Narkiewicz J, Giachin G, Legname G. *In vitro* aggregation assays for the characterization of α-synuclein prion-like properties. *Prion* (2014) **8**:19–32. doi: 10.4161/pri.28125
85. Jung BC, Lim Y-J, Bae E-J, Lee JS, Choi MS, Lee MK, et al. Amplification of distinct α-synuclein fibril conformers through protein misfolding cyclic amplification. *Exp Mol Med.* (2017) **49**:e314. doi: 10.1038/emm.2017.1
86. Roostaee A, Côté S, Roucou X. Aggregation and amyloid fibril formation induced by chemical dimerization of recombinant prion protein in physiological-like conditions. *J Biol Chem.* (2009) **284**:30907–16. doi: 10.1074/jbc.M109.057950
87. Volpicelli-Daley LA, Luk KC, Lee VMY. Addition of exogenous α-synuclein preformed fibrils to primary neuronal cultures to seed recruitment of endogenous α-synuclein to Lewy body and Lewy neurite-like aggregates. *Nat Protoc.* (2014) **9**:2135–46. doi: 10.1038/nprot.2014.143
88. Paslawski W, Lorenzen N, Otzen DE. Formation and characterization of α-synuclein oligomers. *Methods Mol Biol.* (2016) **1345**:133–50. doi: 10.1007/978-1-4939-2978-8_9
89. Huang C, Ren G, Zhou H, Wang C. A new method for purification of recombinant human alpha-synuclein in *Escherichia coli*. *Protein Expr Purif.* (2005) **42**:173–7. doi: 10.1016/j.pep.2005.02.014
90. Ariesandi W, Chang CF, Chen TE, Chen YR. Temperature-dependent structural changes of Parkinson's alpha-synuclein reveal the role of pre-existing oligomers in alpha-synuclein fibrillization. *PLoS ONE* (2013) **8**:e53487. doi: 10.1371/journal.pone.0053487
91. Gould N, Mor DE, Lightfoot R, Malkus K, Giasson B, Ischiropoulos H. Evidence of native α-synuclein conformers in the human brain. *J Biol Chem.* (2014) **289**:7929–34. doi: 10.1074/jbc.C113.538249
92. Padayachee ER, Zetterberg H, Portelius E, Borén J, Molinuevo JL, Andreasen N, et al. Cerebrospinal fluid-induced retardation of amyloid β aggregation correlates with Alzheimer's disease and the APOE ε4 allele. *Brain Res.* (2016) **1651**:11–6. doi: 10.1016/j.brainres.2016.09.022
93. Melki R. Role of different alpha-synuclein strains in synucleinopathies, similarities with other neurodegenerative diseases. *J Park Dis.* (2015) **5**:217–27. doi: 10.3233/JPD-150543
94. Peelaerts W, Bousset L, Van der Perren A, Moskalyuk A, Pulizzi R, Giugliano M, et al. α-Synuclein strains cause distinct synucleinopathies after local and systemic administration. *Nature* (2015) **522**:340–4. doi: 10.1038/nature 14547
95. Walker L, McAleese KE, Thomas AJ, Johnson M, Martin-Ruiz C, Parker C, et al. Neuropathologically mixed Alzheimer's and Lewy body disease: burden of pathological protein aggregates differs between clinical phenotypes. *Acta Neuropathol.* (2015) **129**:729–48. doi: 10.1007/s00401-015-1406-3
96. Hamilton RL. Lewy bodies in Alzheimer's disease: a neuropathological review of 145 cases using alpha-synuclein immunohistochemistry. *Brain Pathol.* (2000) **10**:378–84. doi: 10.1111/j.1750-3639.2000.tb00269.x
97. Guo JL, Covell DJ, Daniels JP, Iba M, Stieber A, Zhang B, et al. Distinct α-synuclein strains differentially promote tau inclusions in neurons. *Cell* (2013) **154**:103–17. doi: 10.1016/j.cell.2013.05.057
98. Peng C, Gathagan RJ, Lee VMY. Distinct α-Synuclein strains and implications for heterogeneity among α-Synucleinopathies. *Neurobiol Dis.* (2018) **109**:209–18. doi: 10.1016/j.nbd.2017.07.018
99. Kayed R, Head E, Sarsoza F, Saing T, Cotman CW, Necula M, et al. Fibril specific, conformation dependent antibodies recognize a generic epitope common to amyloid fibrils and fibrillar oligomers that is absent in prefibrillar oligomers. *Mol Neurodegener.* (2007) **2**:18. doi: 10.1186/1750-1326-2-18
100. Saverioni D, Notari S, Capellari S, Poggiolini I, Giese A, Kretzschmar HA, et al. Analyses of protease resistance and aggregation state of abnormal prion protein across the spectrum of human prions. *J Biol Chem.* (2013) **288**:27972–85. doi: 10.1074/jbc.M113.477547
101. Bousset L, Pieri L, Ruiz-Arlandis G, Gath J, Jensen PH, Habenstein B, et al. Structural and functional characterization of two alpha-synuclein strains. *Nat Commun.* (2013) **4**:2575. doi: 10.1038/ncomms3575
102. Escada PA, Lima C, da Silva JM. The human olfactory mucosa. *Eur Arch Otorhinolaryngol.* (2009) **266**:1675–80. doi: 10.1007/s00405-009-1073-x
103. Orrú CD, Bongianni M, Tonoli G, Ferrari S, Hughson AG, Groveman BR, et al. A test for Creutzfeldt-Jakob disease using nasal brushings. *N Engl J Med.* (2014) **371**:519–29. doi: 10.1056/NEJMoa1315200
104. Haley NJ, Motter AV de, Carver S, Henderson D, Davenport K, Seelig DM, et al. Prion-seeding activity in cerebrospinal fluid of deer with chronic wasting disease. *PLoS ONE* (2013) **8**:e81488. doi: 10.1371/journal.pone.0081488
105. Haley NJ, Carver S, Hoon-Hanks LL, Henderson DM, Davenport KA, Bunting E, et al. Detection of chronic wasting disease in the lymph nodes of free-ranging cervids by real-time quaking-induced conversion. *J Clin Microbiol.* (2014) **52**:3237–43. doi: 10.1128/JCM.01258-14
106. Haley NJ, Siepker C, Walter WD, Thomsen BV, Greenlee JJ, Lehmkuhl AD, et al. Antemortem detection of chronic wasting disease prions in nasal brush collections and rectal biopsy specimens from white-tailed deer by real-time quaking-induced conversion. *J Clin Microbiol.* (2016) **54**:1108–16. doi: 10.1128/JCM.02699-15
107. Haley NJ, Siepker C, Hoon-Hanks LL, Mitchell G, Walter WD, Manca M, et al. Seeded amplification of chronic wasting disease prions in nasal brushings and recto-anal mucosa-associated lymphoid tissues from elk by real-time quaking-induced conversion. *J Clin Microbiol.* (2016) **54**:1117–26. doi: 10.1128/JCM.02700-15

Conflict of Interest Statement: The authors declare that the research was conducted in the absence of any commercial or financial relationships that could be construed as a potential conflict of interest.

Copyright © 2018 Paciotti, Bellomo, Gatticchi and Parnetti. This is an open-access article distributed under the terms of the Creative Commons Attribution License (CC BY). The use, distribution or reproduction in other forums is permitted, provided the original author(s) and the copyright owner are credited and that the original publication in this journal is cited, in accordance with accepted academic practice. No use, distribution or reproduction is permitted which does not comply with these terms.

2.3 Impact of experimental factors on α-syn PMCA and RT-QuIC assays (manuscript in preparation)

Materials and Methods

α-synuclein expression and purification

Escherichia Coli BL21(DE3) Gold were transformed with pT7-7 vector cloned with the gene encoding α-syn. The overnight preculture of transformed cells was diluted 100-fold in LB medium and induced at an OD_{600} value of 0.6-0.8 with 1 mM Isopropyl-β-D-thiogalactoside and, after 5 hours incubation at 37 °C, the cells were harvested at 4000 rpm (JA-10, Beckman Coulter). The extraction was carried out through osmotic shock using 100 ml of buffer TRIS 30 mM, EDTA 2 mM and sucrose 40%, at pH 7.2 according to Shevchik et al.[62] and Huang et al.[63]. The suspension was then ultracentrifuged at 20000 rpm (Type 70 Ti rotor, Beckman Coulter) for 25 min and pellet was collected and resuspended with 90 ml precooled ultrapure water additioned with 38µl of $MgCl_2$ 1 M and then ultracentrifuged a second time. Surnatants derived from these two centrifugation steps, were joined and dialyzed against 4 liters of buffer 20 mM TRIS/HCl at pH 8.0. The protein then was loaded in the FPLC system and an anion exchange chromatography was carried out with 0-50% linear gradient NaCl 1 M (GE Healthcare HiPrep™ Q HP 16/10 Column). The collected fractions were lyophilized and resuspended in 10 mM TRIS/HCl, 1 mM EDTA and urea 8 M at pH 8.0 for the chemical denaturation. To eliminate all the protein formed aggregates, two size-exclusion chromatographies (HiLoad™ 16/600 Superdex™ 75 pg Column) were performed with 20 mM phosphate and 0.5 mM EDTA at pH 8.0 as elution buffer. Purified α-synuclein (α-syn) was dialyzed against Milli-Q water and lyophilized in batches for long-term storage. Roche cOmplete™ protease inhibitor cocktail was added only during the extraction step in the quantity suggested by the producer.

Setup of the RT-QuIC experiments

The lyophilized aliquots α-syn were resuspended in NaOH 3.5 mM (pH 11.54) right before the experiments to avoid the instantaneous formation of aggregates. At high pH, the negatively charged monomers (the isoelectric point of α-syn is 4.67) experience an electrostatic repulsion that impedes the aggregation and favors the dissociation of small aggregates.[64,65] The solution of α-syn and NaOH was brought to the desired pH by adding concentrated buffer. Thioflavin-T (ThT) was also added in a final concentration of 10 µM. To avoid the possible growth of bacteria during the experiment, a 0.08% of NaN_3 was

present in the reaction buffer. Each sample was then split in 3 replicates that were then put in a *TECAN* clear-bottom 96-well plate. We added acid-washed glass beads in each well, of different size and number depending on the experiment, to enhance the aggregation speed and increase homogeneity among replicates.[66] The plates were always sealed with a sealing tape to minimize evaporation during the experiments. Successively, plates were inserted in a BMG LABTECH ClarioStar fluorimeter and subjected to the incubation/shaking protocol of Shahnawaz et al.[52] (T = 310 K, 29 min. incubation, 1 min. shaking at 500 rpm) or to the one of Groveman *et al*..[54] Once every 30 minutes, the fluorescence was read from the bottom using an excitation and emission wavelength of 450 nm and 480 nm, respectively.

Preformed seeds preparation

Monomeric α-syn at the concentration of 2 mg/ml was incubated in PIPES buffer with 500 mM NaCl at 310 K in two wells (250 µl per well) under constant agitation at 500 rpm. One of the two wells contained 10 µM ThT in order to monitor the aggregation. Once the plateau of the aggregation ThT profiles was abundantly passed (usually after seven days), the sample without ThT was subjected to cycles of sonication, using an immersion sonicator, in order to obtain smaller aggregates. Usually 5 repetitions of cycles of 15 sec sonication (12 µM amplitude) and 15 seconds rest were enough for the purpose. The solution containing the preformed aggregates was then split in aliquots, diluted to the desired concentrations and stored at -80°C for later use.

Results & Discussion

Ab initio simulations

We started our analysis by making simulations to understand what kind of models could rely under the RT-QuIC/PMCA techniques. Before working on experimental data, we wanted to reproduce the linear relation observed by Shahnawaz et al.[52] and by Arosio et al.,[67] between the $t_{1/2}$ (time to the half of the maximum value) and the logarithm of the seed (preformed aggregates) mass concentration (mass of the preformed aggregates present in solution). A nucleated polymerization model (Eq. 2.3.1) with variable fragmentation (Fig. 2.3.1) was enough to reproduce an approximate linear relation (see Fig. 2.3.2). This result is in accord with the fact that, for α-syn, secondary nucleation can be neglected with respect to elongation and fragmentation at pH above 6.0.[68]

$$f_i(t) = +k_n m(t)^{n_0}\delta_{i,n_0} - k_{on}m(t)f_i(t) + k_{on}m(t)f_{i-1}(t) - k_{off}f_i(t) + k_{off}f_{i+1}(t)$$
$$- k_{frag}(t)(i-1)f_i(t) + 2k_{frag}(t)\sum_{j=i+1}^{\infty} f_j(t)$$

$$P_f(t) = \sum_{i=n_0}^{\infty} f_i(t) \quad ; \quad M_f(t) = \sum_{i=n_0}^{\infty} i f_i(t)$$

$$\begin{cases} \frac{dP_f(t)}{dt} = k_{frag}(t)\left[M_f(t) - (2n_0 - 1)P_f(t)\right] + k_n m(t)^{n_0} \\ \frac{dM_f(t)}{dt} = \left(m(t)k_{on} - k_{off} - k_{frag}(t)n_0(n_0-1)\right)P_f(t) + +n_0 k_n m(t)^{n_c} \end{cases} \quad (2.3.1)$$

$f_i(t) = population\ of\ fibrils\ made\ by\ i\ monomers;\ k_n = primary\ nucleation\ rate\ constant;$
$m(t) = monomer\ population; n_0 = size\ of\ smallest\ nucleus\ (2);\ \delta_{ij} = Kronecker's\ delta\ function;$
$k_{on} = fibril\ polymerisation\ rate\ constant;\ k_{off} = depolymerisation\ rate\ constant;$
$k_{frag}(t) = variable\ fragmentation\ rate;\ P_f(t) = fibril\ total\ population;\ M_f(t) = fibril\ total\ mass$

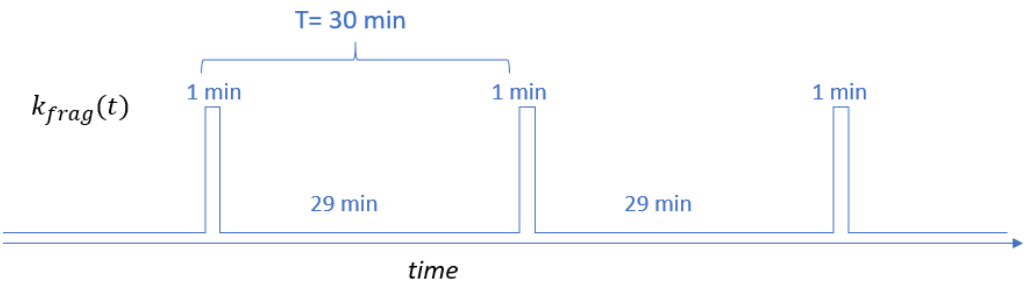

Fig. 2.3.1 The variable fragmentation constant, in the model of differential equations used for the simulations, varies according to the incubation/shaking cycles of a PMCA protocol.

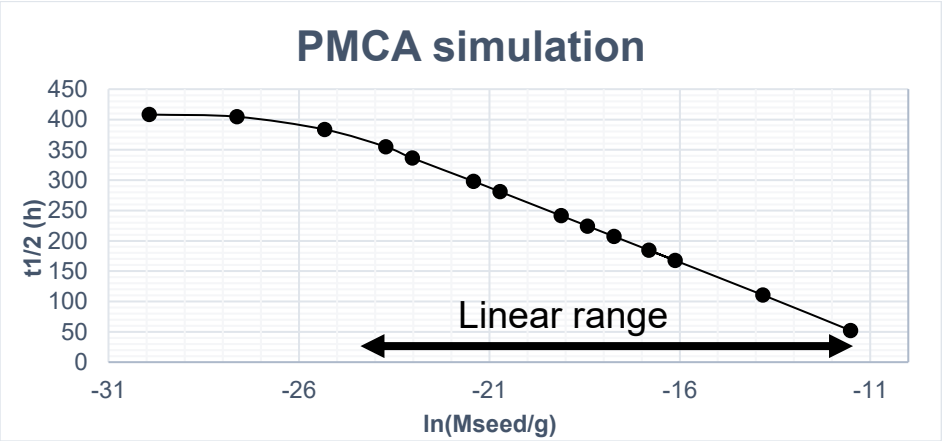

Fig. 2.3.2 By numerically integrating the differential equation system in Eq. 2.3.1 with a Runge-Kutta[69] routine, it was possible to extract the $t_{1/2}$. In this way, it was possible to demonstrate the existence of a range of preformed aggregates (seeds) concentrations (starting from arbitrary kinetic constants) in which the relation between the logarithm of the initial mass of the seeds and the $t_{1/2}$ of the "sigmoidal" growth of the fibrillary species is linear.

Obviously, the simulated linear range of seed masses in Fig. 2.3.2 is arbitrary and not related to experimental values. The range of seed masses, for which it is possible to obtain this linear relation depends on the kinetic constants of the processes, which themselves depend on the nature of the protein-protein interaction and on experimental variables like temperature, pH, shaking cycles, protein concentrations and ionic strength. Optimizing the experimental variables, in order to maximize the differentiation between seed masses, is nowadays the crucial part of the development of PMCA and RT-QuIC techniques for the diagnosis of synucleinopathies.

Variables influencing α-syn RT-QuIC

We evaluated the impact on α-syn aggregation of some experimental variables like the addition of glass beads, size and number of glass beads and the addition of human CSF. The addition of glass beads to wells containing ThT and monomeric α-syn is reported in literature to be beneficial for reducing the fibrillization time and for increasing the homogeneity among replicates.[66] Actually, by making tests on equivalent samples with and without glass beads, we found that is actually the case. In Fig. 2.3.3 are shown the ThT fluorescence profiles of α-syn samples with seeds, subjected to a PMCA protocol, with and without glass beads. The replicates in Fig. 2.3.3 A produced very different fluorescence lineshapes and, at 160 h, they still did not reach the final plateau of the aggregation profiles. The replicates in Fig. 2.3.3 B instead produced very similar fluorescence lineshapes and reached the final plateau of the aggregation profiles in about 100 h.

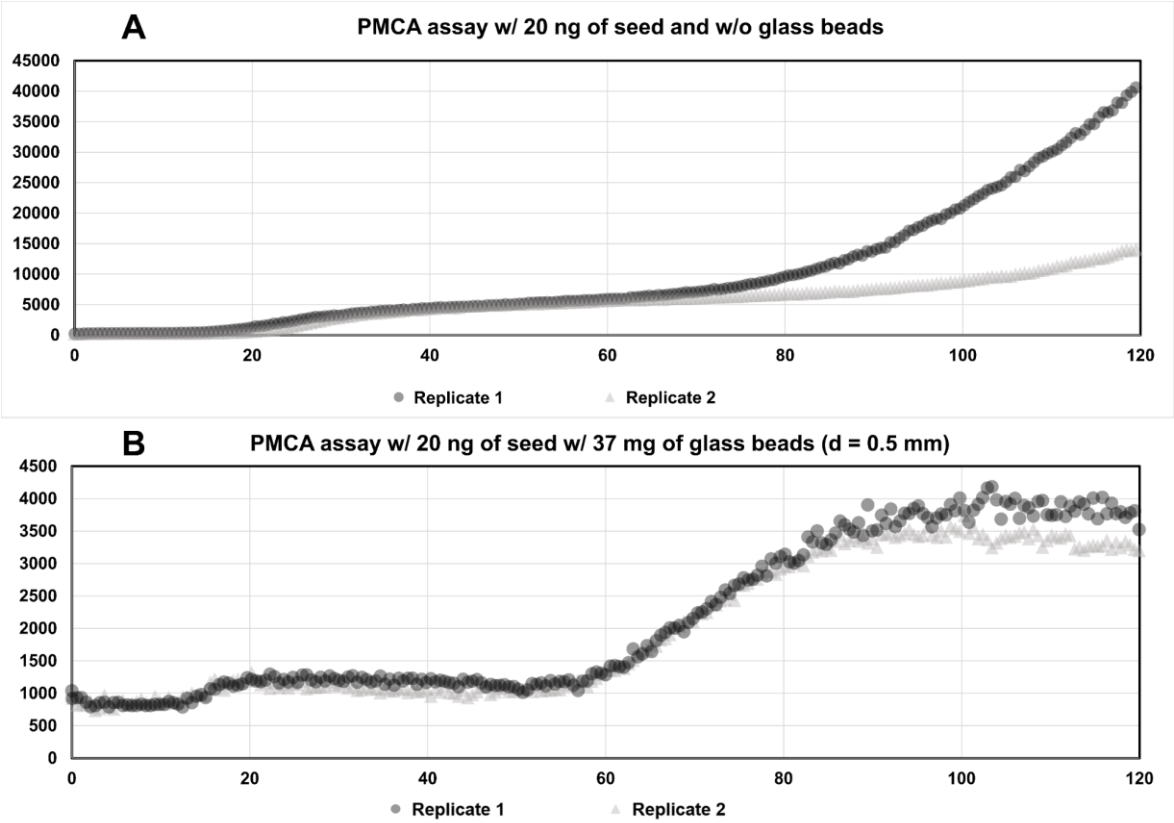

*Fig. 2.3.3 Monomeric α-syn 0.125 mg/ml (8.7 μM) was left aggregating in the presence of ThT 10 μM and 0.2 ng of preformed seeds. The experiments were performed in duplicate in a 96-wells plate in PIPES buffer pH 6.5 (with 500 mM NaCl). The plate was subjected to cycles of shaking (1 min. shaking 500 rpm, 29 min. rest) at 310 K, inside a BMG Labtech ClarioStar fluorimeter. In **A)** no glass beads were added while, in **B),** 37 mg of 0.5 mm diameter glass beads were added to the samples.*

A second experiment was performed to evaluate the impact of different size and number of glass beads in three different buffers, the results are shown in Fig. 2.3.4. From this image, it is possible to appreciate that a single bead of 3 mm of diameter produced a faster aggregation with respect to 17 beads with a diameter of 0.5 mm. moreover for any beads size and number, the buffers with higher pH produced a slower aggregation.

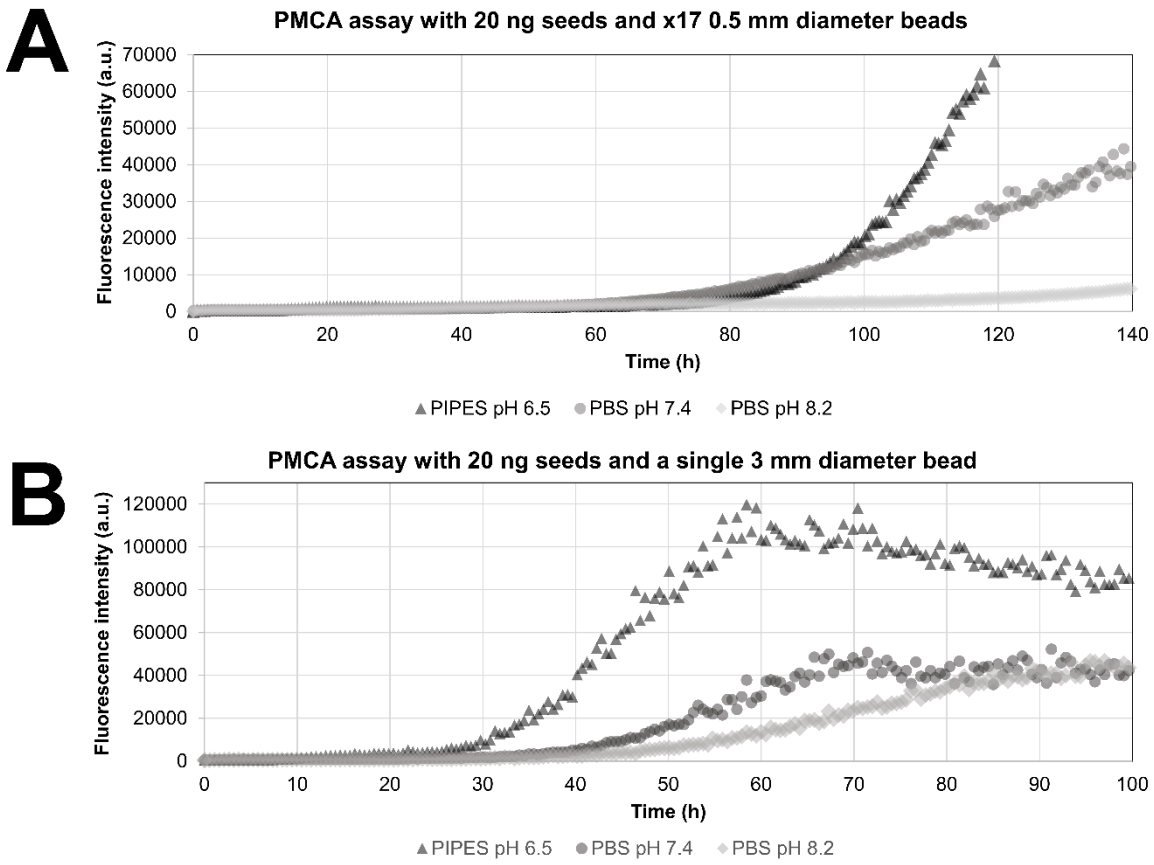

*Fig. 2.3.4 Monomeric α-syn 0.08 mg/ml (6.9 μM) was left aggregating in the presence of ThT 10 μM and 20 ng of preformed seeds. The experiments were performed in duplicate in a 96-wells plate in three different buffers: PIPES buffer pH 6.5 (with 500 mM NaCl), PBS buffer pH 7.4 and PBS buffer pH 8.2. The plate was subjected to cycles of shaking (1 min. shaking 500 rpm, 29 min. rest) at 310 K, inside a BMG Labtech ClarioStar fluorimeter. The displayed data is the result of average of the two replicates for each sample. In **A)** 17 glass beads with a diameter of 0.5 mm were added, in **B),** a single bead with a diameter of 3 mm was added to the samples.*

Among the tested experimental variables, one of the major effects on α-syn aggregation was due to the addition of human CSF. From α-syn aggregation experiments we observed that CSF is able to slow down reproducibly and significantly the aggregation process, probably due to the interaction of α-syn with some compounds present in the human biofluid. We tested the antiaggregatory effect of CSF on α-syn by RT-QuIC ThT fluorescence assays by adding aliquots of CSF of neurological controls (Fig. 2.3.5 A). Results similar to the one shown in Fig. 2.3.5 A were obtained also using PBS buffer and CSF from other controls subjects, PD patients and DLB patients.

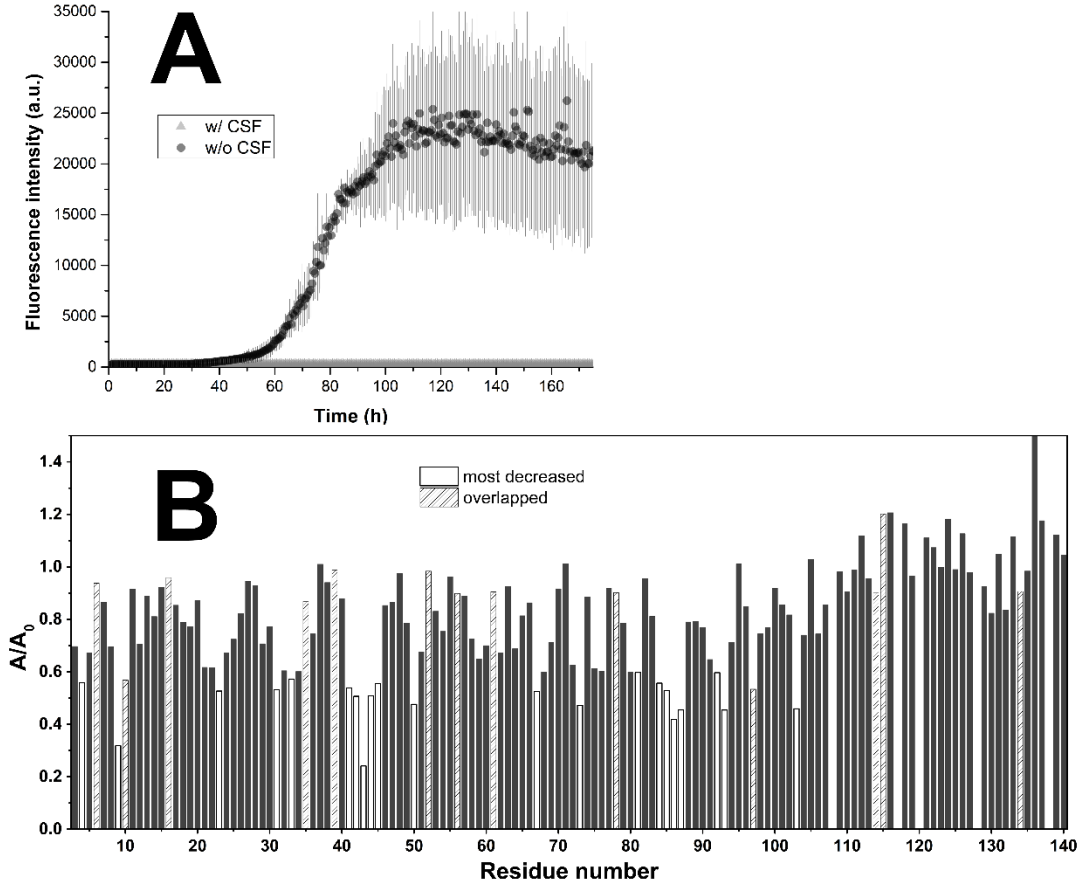

Fig. 2.3.5 ***A)*** *RT-QuIC assay performed using 0.8 mg/mL of recombinant α-syn in PIPES pH 6.5 (500 mM NaCl) with (light grey) and without (dark grey) 40 µl of hydrocephalus CSF (final volume of 200 µl). 21 glass beads with a diameter of 0.5 mm were added in each well. The data shown are the averages of three replicates on a 96-wells plate. The experiment was repeated in PBS buffer with 137 mM NaCl at pH 7.4 and at pH 8.0 with similar results.* ***B)*** *Amplitude ratios (corrected for dilution) of peaks coming from 2D ^{15}N-^{1}H HSQC NMR experiments performed at T = 283 K, using a Bruker 950 MHz NMR spectrometer. 100 µl of CSF were added to PBS buffer containing 50 µM of ^{15}N labelled α-syn. The smaller amplitude ratios at the N-terminus and at the NAC region of α-syn are a sign of interaction with unknown CSF constituents. The ratios highlighted as "most decreased" are the ones which are smaller by one or more standard deviation with respect to the average value. The ones highlighted as "overlapped" come from intensity measurements of partially overlapped peaks in the 2D ^{15}N-^{1}H HSQC spectrum and are less reliable.*

We also investigated the possible interaction of ^{15}N labelled α-syn monomers with human CSF with solution NMR (Fig. 2.3.5 B) and we found that the resonances relative to peaks in the N-terminus and NAC region of α-synuclein had decreased intensity in the presence of human CSF. The resonances relative to the amide protons of the C-terminus increased their intensities suggesting an increased mobility in the presence of CSF. No relevant changes in chemical shifts were observed, suggesting that the interacting compounds might be of high molecular weight. The inhibitory effect of CSF on α-syn aggregation was

previously reported by Shahnawaz, Soto and coworkers[52] but was not further investigated. In 2016 Linse and coworkers[30] observed a similar effect produced by human CSF on the Aβ aggregation kinetics, they found that possible candidates for that inhibition could be high-density lipoproteins (HDL). However, as can be seen from paragraph 3.2, we found that the addition of human HDL (from human plasma), although it significantly reduced the quantity of both oligomeric and fibrillary aggregates, could not produce the intensity decrease observed by NMR experiments resulting from the addition of human CSF. However, there is the possibility that the effect on monomeric α-syn and the effect on the aggregation can be two distinct phenomena, since it is known that aggregation inhibitors can interact with oligomeric and prefibrillar species and not with the monomer.[70] In this respect, we cannot exclude that lipoproteins may be responsible for the antiaggregatory effect of human CSF.

RT-QuIC tests with preformed seeds

PMCA and RT-QuIC protocols were tested by using CSF coming from a hydrocephalus subjects not suffering from neurodegenerative diseases. This choice was made because we had abundant aliquots from these types of patients and because CSF samples of healthy subjects and PD patients are very rare and must be used only for validation tests, once the protocols have been already optimized. The sensitivity and the differentiation capability of the assays were tested by adding in-lab made preformed aggregates (seeds) in different quantity in each well, the protocol used to produce α-syn seeds is reported in the Materials and Methods section. The incubation/agitation protocol and the reaction buffer (PIPES buffer pH 6.5 with NaCl 500 mM) of Shahnawaz, Soto and coworkers (29 minutes agitation, 1 minute shaking at 500 rpm) were used for all the experiments described in Fig. 2.3.4, 2.3.5, 2.3.6 and Fig. 2.3.7. In Fig 2.3.4 A are reported the kinetic traces, averaged on three replicates for each seed quantity, relative to an RT-QuIC experiment performed with 37 mg of glass beads (diameter of 0.5 mm) per well. From the figure it can be appreciated the fact that for samples containing seeds the fluorescence profiles have two inflection points: a first inflection point, situated between 0 h and 25 h and a second one, situated between 60 h and 70 h. The unseeded samples instead showed only one inflection point, at ~30 h for the sample without CSF and at ~70 h for the sample with CSF. The fact that the second inflection point of the seeded samples precedes of few hours the one of the unseeded sample without CSF made us hypothesize that the increase in fluorescence in correspondence of the first inflection point is due to the growth of the oligomeric/fibrillary

seeds while the second increase of fluorescence happens because of the spontaneous nucleation (and consequent fibrillization) of the free monomer in solution. The decrease of the fluorescence after having reached the maximum value is probably produced by the formation of macroscopic insoluble aggregates, which are able to entrap the molecules of ThT. To accurately measure the position of the first inflection point (t_0), the first parts of the aggregation profiles were fitted with a Boltzmann's sigmoidal function (Eq. 2.3.2), using *OriginPro 9.0*. In the non-linear curve fitting procedure used, the parameters A_1, A_2, t_0 and dt of Eq. 2.3.2 were let free.

$$y(t) = A_2 + \frac{A_1 - A_2}{1 + \exp\left(\frac{t - t_0}{dt}\right)} \qquad (2.3.2)$$

The results of the fitting are shown in Fig. 2.3.4 B. The measured t_0 parameters were then plotted against the natural logarithm of the mass (in ng) of the added seed. From the linear regression shown in Fig. 2.3.4 C we can see that there is a good linearity between the t_0 parameters ($R^2 \sim 1$) and the logarithm of the seed mass, as was expected from simulations and literature.[52,67] The linear response was maintained up to 0.02 pg (0.1 pg/ml) of seed, which coincides with upper detection limit for this protocol.

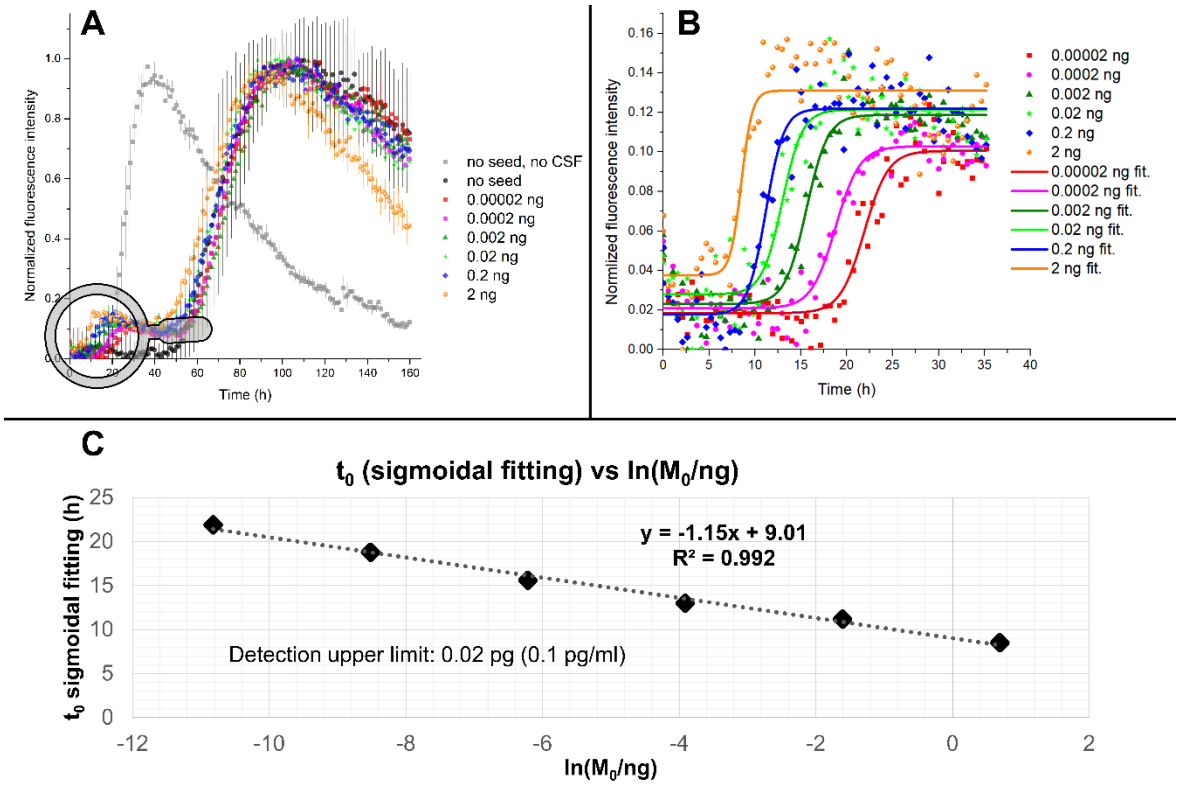

Fig. 2.3.4 ***A)*** *RT-QuIC assay performed using 0.125 mg/mL of recombinant α-syn in PIPES pH 6.5 (500 mM NaCl) with 40 µl of CSF (final volume of 250 µl) in the presence of different quantities of preformed aggregates and 37 mg of glass beads with a diameter of 0.5 mm. The data shown are the*

averages of three replicates on a 96-wells plate while the error bars were calculated as the standard deviations of the averages. ***B)*** *The first part of the aggregation curves was fitted with a Boltzmann's sigmoidal function, using OriginPro 9.0, to extract the position t_0 of the inflection point.* ***C)*** *The measured t_0 values were plotted against the logarithm of the added quantity of seed and fitted with a line with the linear regression tool of Microsoft Excel.*

What we learnt from this experiment is that, to optimize the assay, it is necessary to promote the "seeded" aggregation and limit the spontaneous aggregation of the free monomer in order to obtain the maximum possible differentiation of the masses of the added seeds. From the linear regression of Fig. 2.3.4 B, it is possible to notice that, although the R^2 coefficient is almost 1, the slope of the line is pretty low, which represent the fact that the first inflection point of the aggregation profiles lays in in a short range of time (5 h - 20 h) for all the curves. In the second trial we lowered the monomer concentration from 1.25 mg/ml to 0.8 mg/ml. This choice was made to discourage the primary nucleation kinetics, which is thought to depend on the square of the monomer concentration while the polymerization kinetics of the fibrils is thought to depend linearly from that. We also decreased the amount of glass beads per well from 37 mg to a fixed number of 15, this was made because we noticed that with the previous quantity, the beads arranged in a way that limited their motion during the shaking, thus probably diminishing the impact of the fragmentation kinetics produced by agitation. As before, we analyzed the first part of the aggregation curves extracting the t_0 parameters with the sigmoidal fitting (Fig. 2.3.5 A) but we tried also to estimate the so-called *lag-time* to quantify the time at which the fluorescence starts to deviate significantly from its initial value. We defined it, in a way similar to the one used by Groveman et al.,[54] as the time at which the fluorescence (F) of each well becomes higher than the average fluorescence of the first 10 h ($\overline{F(t)}_{t<10\,h}$) of the sample without seeds plus 5 standard deviations (5σ) for 5 consecutive measurements:

$$F\left(t_{lag}+i\Delta t\right) \geq \overline{F(t)}_{t<10\,h} + 5\sigma\left(F(t)\right)_{t<10\,h};\ \forall\, i \in (0,1,2,3,4) \qquad (2.3.3)$$

Where Δt is the time between two consecutive measurements (30 minutes in this case). The inverse of the lag-time, the lag-rate, is usually used in the RT-QuIC literature to visualize the data since it provides a faster and easier way to examine together the outcome of multiple experiments with respect of plotting the fluorescence profiles for all the samples in the same graph (an example of this representation is provided in Fig. 2.3.5 C). The averages of the lag-times (estimated with the threshold method of Eq. 2.3.3) on the three replicates were plotted against the natural logarithm of the seed masses, the result of the linear regression procedure is shown in Fig. 2.3.5 D.

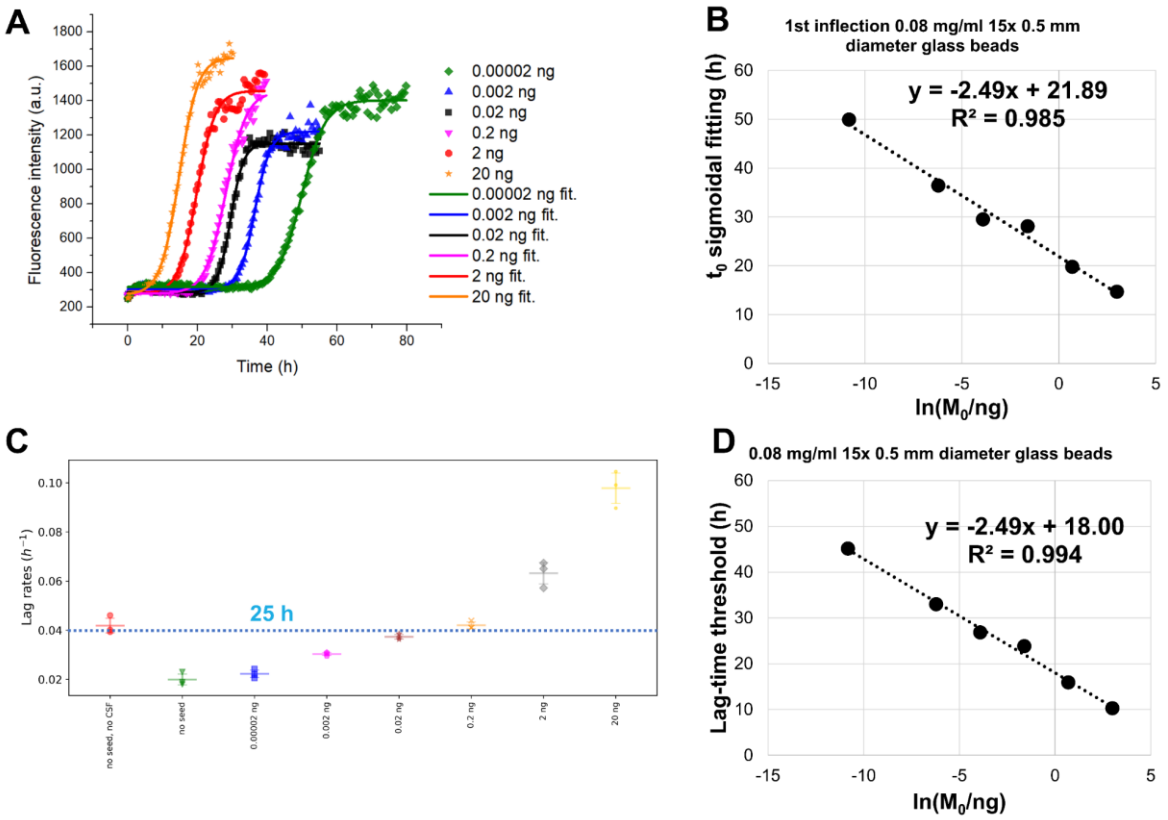

Fig. 2.3.5 RT-QuIC assay performed using 0.08 mg/mL of recombinant α-syn in PIPES pH 6.5 (500 mM NaCl) with 40 µl of CSF (final volume of 250 µl) in the presence of different quantities of preformed aggregates and 15 glass beads with a diameter of 0.5 mm. ***A)*** *The first part of the aggregation curves, averaged on the three replicates, was fitted with a Boltzmann's sigmoidal function, using OriginPro 9.0, to extract the position t_0 of the inflection point.* ***B)*** *The measured t_0 values were plotted against the logarithm of the added quantity of seed and fitted with a line with the linear regression tool of Microsoft Excel.* ***C)*** *The lag-rates are calculated as the inverse of the lag-times for each sample.* ***D)*** *The measured lag-times, averaged on the three replicates, were plotted against the logarithm of the added quantity of seed and fitted with a line with the linear regression tool of Microsoft Excel.*

The R^2 values and the slopes of the linear regressions for the t_0 values and the lag-times were similar, as expected, with the slope being more than twice the one calculated in Fig. 2.3.4 C. The tested protocol was still able to differentiate seed masses with an upper detection limit of 0.02 pg. In Fig. 2.3.6 is reported a summary of the measured t_0 value for different bead size and initial monomer concentrations. The t_0 parameter was calculated both on the first and on the second inflection point in the same conditions in Fig. 2.3.6 A and in Fig.2.3.6 B.

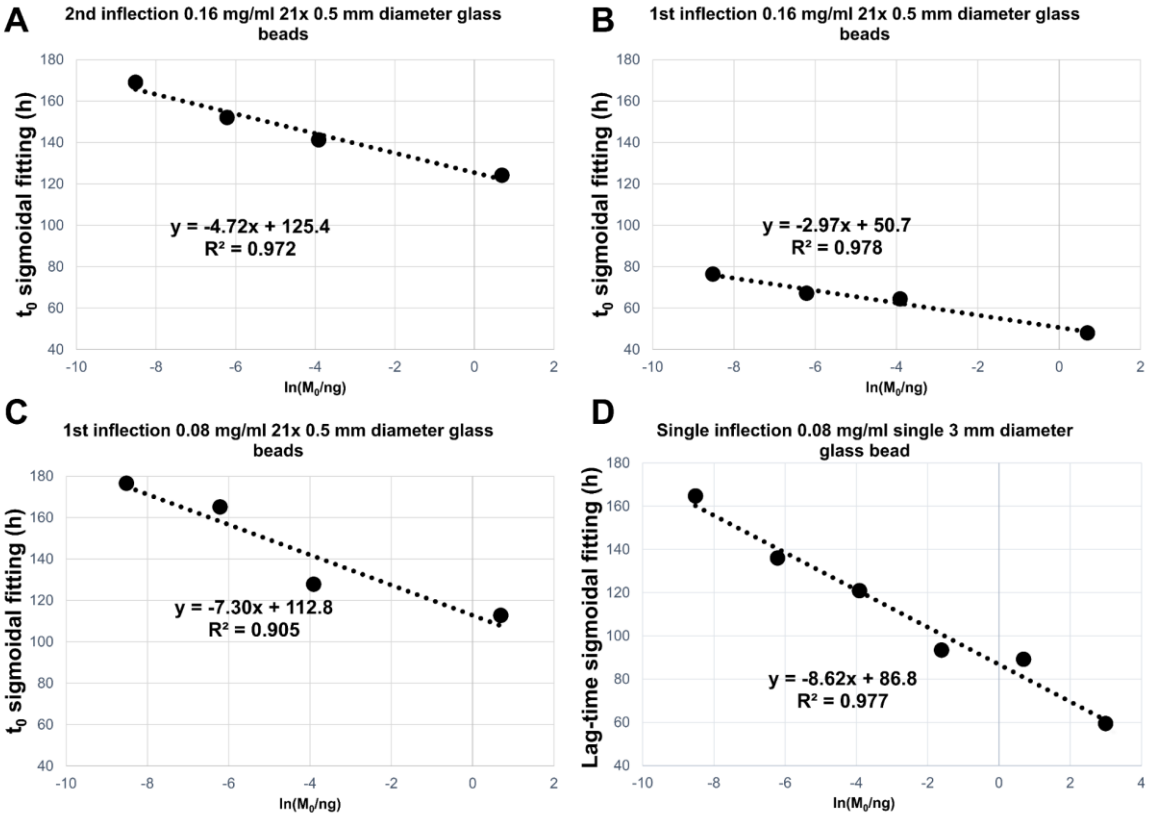

*Fig. 2.3.6 Linear regression analyses, performed with the linear regression tool of Microsoft Excel, of the t_0 relative to RT-QuIC assays performed in in PIPES pH 6.5 (500 mM NaCl) with 40 µl of CSF (final volume of 250 µl) in the presence of different quantities of preformed aggregates. The t_0 parameters were obtained by fitting the first or the second part of the normalized and averaged fluorescence profiles with Boltzmann's sigmoidal functions in OriginPro 9.0. In **A)** a starting concentration of 0.16 mg/mL monomeric α-syn was used together with 21 glass beads with a diameter of 0.5 mm. The t_0 parameters were obtained by fitting the second part of the normalized and averaged fluorescence profiles. In **B)** a starting concentration of 0.16 mg/mL monomeric α-syn was used together with 21 glass beads with a diameter of 0.5 mm. The t_0 parameters were obtained by fitting the first part of the normalized and averaged fluorescence profiles. In **C)** a starting concentration of 0.08 mg/mL monomeric α-syn was used together with 21 glass beads with a diameter of 0.5 mm. The t_0 parameters were obtained by fitting the first part of the normalized and averaged fluorescence profiles. In **D)** a starting concentration of 0.08 mg/mL monomeric α-syn was used together with 1 glass bead with a diameter of 3 mm. The t_0 parameters were obtained by fitting the normalized and averaged fluorescence profiles.*

All the tested conditions produced satisfactory differentiations between seed masses with a good linear correlation between the measured t_0 parameters and the logarithm of the added seed masses. By looking at Fig. 2.3.6 B and Fig. 2.3.6 C it is possible to notice that, as expected from the considerations on the nucleation and polymerization kinetics, the samples with a monomer starting concentration of 0.08 mg/ml produced an increased slope compared to the ones with 0.16 mg/ml; although the overall experiment duration was also longer. The second inflection point showed also to be discriminative for the 0.16 mg/ml monomer concentration, as can be seen from Fig. 2.3.6 A, while for the 0.08 mg/ml monomer concentration it was still not reached after 250 h. The increased number of beads,

with respect to Fig. 2.3.5 C, did not produce neither a significative increase in the aggregation speed nor seed mass discrimination, nor any effect on the presence of the two inflection points. However, by substituting the 21 beads with a diameter of 0.5 mm with a single bead with a diameter of 3 mm (the total bead mass is ~ 10 times greater) we observed the disappearance of the first inflection point (Fig.2.3.7 A). The t_0 values and the lag-times measured for this kinetics produced good results in terms of R^2 and slope of the linear regression, as can be seen from Fig. 2.3.6 D and from Fig. 2.3.7 B.

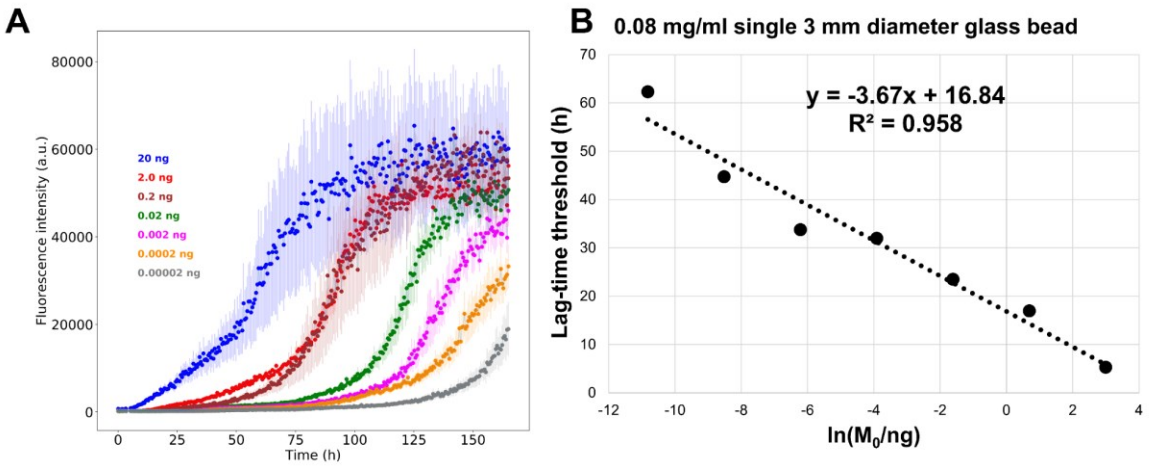

Fig. 2.3.7 RT-QuIC assay performed using 0.08 mg/mL of recombinant α-syn in PIPES pH 6.5 (500 mM NaCl) with 40 µl of CSF (final volume of 250 µl) in the presence of different quantities of preformed aggregates and 1 single glass bead with a diameter of 3 mm. The data shown are the averages of three replicates on a 96-wells plate while the error bars were calculated as the standard deviations of the averages.

Another variable that emerged in some protocols present in literature[53,54] is the presence of detergents, such as *Sodium Dodecyl Sulphate* (SDS), which is commonly used in the RT-QuIC protocols for the detection of PrP^{Sc}. The SDS-induced fibrillization of α-syn was extensively and accurately characterized by Otzen and coworkers[71] and it is currently used to increase the speed and reproducibility of screening assays to measure the effects of antiaggregatory compounds on α-syn fibrillization.[72]

SDS (%)	seed (pg)	lag-time (h)
0.00	0.00	> 120
0.05	0.00	> 120
0.25	0.00	18 ± 7
0.50	0.00	17 ± 5
0.00	0.01	> 120
0.05	0.01	39.0 ± 0.7
0.25	0.01	10 ± 3
0.50	0.01	7 ± 1

Table 2.3.1: Effect of the addition of different quantities of SDS to the reaction buffer. The lag times were evaluated for each well using the formula in Eq. 2.3.3 by considering the average fluorescence of the first 5 h instead of 10 h due to the high aggregation propensity of samples containing seeds and 0.5% SDS.

We tested the addition of SDS using α-syn 0.8 mg/ml in PBS pH 7.4, 6 x 1 mm diameter glass beads and 15 µl of pooled CSF from control subjects for a final volume of 100 µl per well. As can be evinced from Table 2.3.1, the addition of SDS dramatically accelerated the aggregation kinetics of α-syn both in seeded and unseeded experiments. The SDS-induced α-syn fibrils are known for containing a mixture of α-helix and β-sheet and their morphology differs from that of only agitation-induced α-syn fibrils. Anyway, the two morphologies can interconvert and, thanks to temperature and strong agitation, converge into ThT responsive structures rich in β-sheet motifs.[71]

Conclusions

The results of the experiments performed for this work showed the impact on RT-QuIC experiments of some experimental variables like monomer concentration, addition of glass beads, size and number of glass beads, buffer pH and composition and the effect of human CSF on seeded and unseeded experiments. For most of the seeded experiments we usually observed the presence of two inflection points. We associated the first one to the seeded aggregation (growth of preformed aggregates) and the second to the spontaneous nucleation of new aggregates from the monomer present in solution. The monomer starting concentration affects the speed of both the seeded and unseeded aggregation. Decreasing the starting monomer concentration increased the experiment duration but produced a greater slope in seeded aggregation experiments, thus increasing the differentiation between the masses of the added seeds. By taking into account nucleated-polymerization kinetic models for protein aggregation,[32] like the one described in Eq. 2.3.1, the monomer concentration dependence of the nucleation kinetics is of a higher order with respect of the

growth of preformed aggregates. Consequently, the decrease of the monomer concentration affects more the unseeded aggregation than the seeded one.

The addition of glass beads increased both the aggregation speed and the homogeneity among replicates of seeded experiments, a result that is in accord with the results previously published by Giehm and Otzen.[66] The size and the number of the beads showed to play a major role also in the differentiation of added seeds. Increasing the number and size of the beads, in a way that they were able to move and did not scatter the light too much, we found that the assay was able to better differentiate among seeds with greater slopes in linear regression analyses. These findings can be motivated by considering the fragmentation kinetics[10,73] of prion-like proteins: preformed aggregates, when fragmented, produce more template units, which can then act as new seeds for the fibrillization process. This result implies that RT-QuIC and PMCA experiments with α-syn may benefit from the use of beads inside samples to increase the reproducibility of the assay, decrease the experiment duration and increase the differentiation among CSF containing different quantities of preformed aggregates.

The addition of SDS in the reaction buffer significantly accelerated the aggregation of α-syn for the tested condition, this result is perfectly in accord with previous studies of Otzen and co-workers,[71,72] who accurately characterized the SDS-induced aggregation of α-syn.

Three reaction buffers were also tested: PIPES buffer 100 mM pH 6.5 with NaCl 500 mM, PBS buffer pH 7.4 and PBS buffer pH 8.2. we observed a decrease in the aggregation speed by moving to higher pH in seeded conditions. This is in accord to the fact that, at high pH, the negatively charged monomers of α-syn (isoelectric point: 4.67) experience an electrostatic repulsion that makes nucleation and the growth of aggregates energetically less favorable.[64,65]

Among the tested experimental variables, the addition of CSF showed to have one of the major impacts. The addition of CSF, also in small quantities (15% of the total volume), is sufficient to slow down the aggregation process of dozens of hours. This slowdown was observed for different buffers and the interaction between α-syn and CSF was confirmed by solution NMR with ^{1}H ^{15}N HSQC experiments. This finding implies that the presence of aggregates may not be the only variable influencing the outcome of PMCA and RT-QuIC assays for the diagnosis of synucleinopathies and that there are unknown compounds present in CSF that physiologically interacts with monomeric or oligomeric α-syn and slow down its aggregation.

2.4 Tests with CSF coming from patients and controls (preliminary results)

The good results obtained while testing RT-QuIC assays allowed us to start performing tests on patients with the knowledge of some of the experimental variables influencing these assays. To perform tests on CSF coming from patients we scaled the total sample volume from 250 µl to 200 µl to decrease the amount of protein needed for the experiments but maintaining the CSF added volume of 40 µl. The increased CSF/buffer ratio brought us to increase also the monomer concentration in order to obtain a reasonable experimental time for this diagnostic assay. We continued to use the buffer and incubation/shaking protocol of Shahnawaz, Soto and co-worker[52] with the addition of glass beads, a combination which showed to be able to detect seed masses below $2 \cdot 10^{-14}$ g. In Fig. 2.4.1 A are present the results, in terms of lag-rates, of a preliminary test performed in quadruplicate on CSF of 2 PD patients, 2 normal-pressure hydrocephalic (NPH) patients and 2 patients with other neurological disease (OND). In this test, 21 glass beads were used in each sample and a monomer concentration of 0.5 mg/ml was used. In Fig. 2.4.1 B are present the results of another preliminary test performed in triplicate on CSF of 2 PD patients, 1 DLB patient, 1 NPH patient and 1 OND patient. In this test, 21 glass beads were used in each sample while the monomer concentration was risen to 0.67 mg/ml. All the lag-rates were calculated as the inverse of the lag-times calculated as described in Eq. 2.4.3.

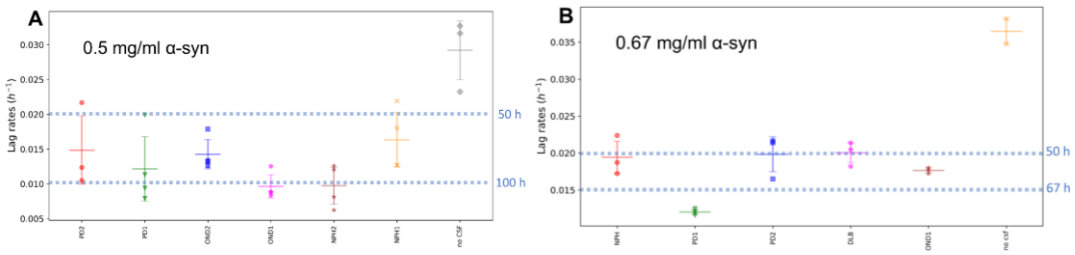

*Fig. 2.4.1 RT-QuIC assay performed using 0.5 mg/mL **(A)** and 0.67 mg/mL **(B)** of recombinant α-syn in PIPES pH 6.5 (500 mM NaCl) with 40 µl of CSF (final volume of 200 µl) coming from PD, DLB, OND and NPH patients in the presence of 21 glass beads with a diameter of 0.5 mm. The lag-rates were calculated as inverse of lag-times calculated as described in Eq. 2.4.3.*

The differentiation between CSF of PD and DLB from the CSF of OND and NPH, appear very poor and the only sample which is showing a significantly higher lag-rate with respect to OND and NPH samples (considering the internal variability among replicates) is the sample without CSF, Thus confirming that CSF constituents different from preformed α-syn

aggregates plays a major role in these kind of assays. To diminish the spontaneous nucleation of α-syn aggregates with respect to the growth of preformed ones we brought the monomer concentration to 0.2 mg/ml and used 6 glass beads with a diameter of 1 mm in each well to further promote the fragmentation kinetics (we increased the total volume of glass beads of more than 2 times). For this last test, the CSF of 9 OND, 5 PD and 4 DLB patients was used. The measured lag-rates for this experiment are shown in Fig. 2.4.2 A.

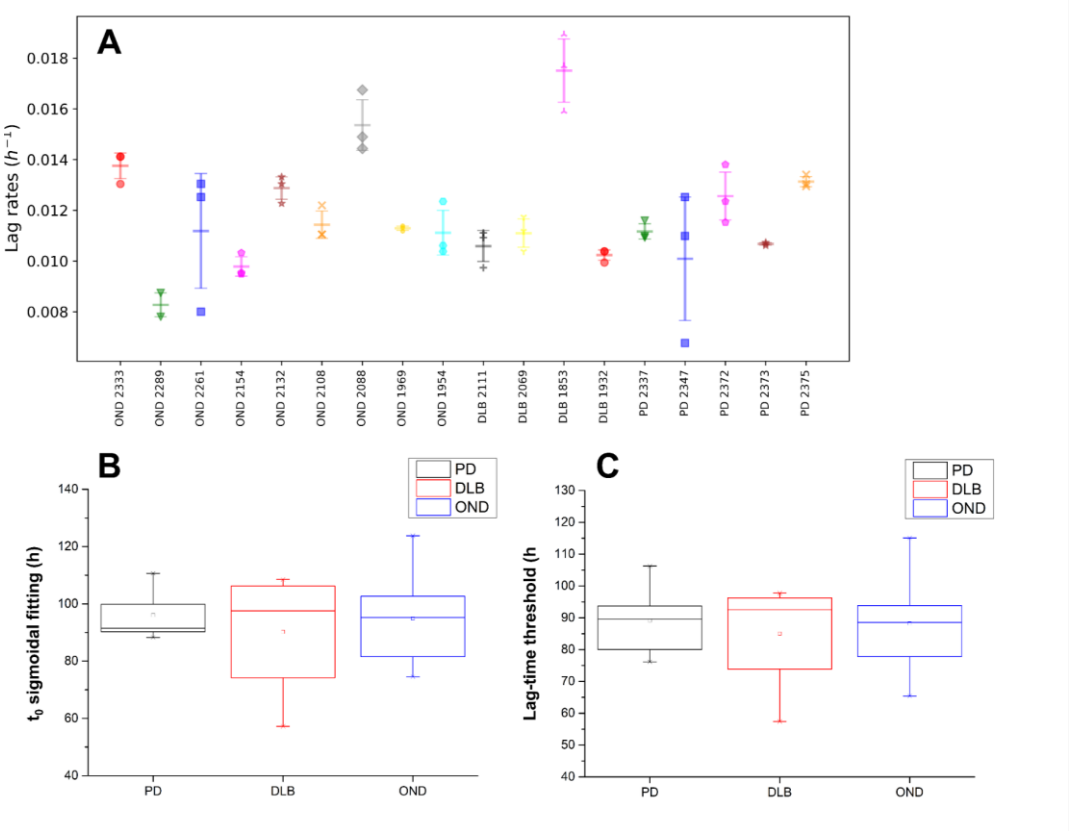

*Fig. 2.4.2 RT-QuIC assay performed using 0.16 mg/mL of recombinant α-syn in PIPES pH 6.5 (500 mM NaCl) with 40 µl of CSF (final volume of 200 µl) coming from PD, DLB, OND and NPH patients in the presence of 6 glass beads with a diameter of 1.0 mm. In **A)** the lag-rates relative to all the samples are shown, while in **B)** and **C)** the summary box plots relative to the t_0 parameters and lag-times are shown. The t_0 parameters were obtained by fitting the first part of the normalized and averaged fluorescence profiles.*

As can be noticed from the box charts of Fig. 2.4.2 B and C, the RT-QuIC protocol used for this test did not provide a good performance in differentiating patients affected by synucleinopathies (PD and DLB) from OND. In fact, none of the three groups showed a significative difference for all the parameters analyzed. Considering these results, we switched to the incubation/shaking protocol and buffer of Groveman et al.[54] These changes consisted in decreasing the reaction volume to 100 µl, with 85 µl of reaction buffer and 15

µl of CSF. The final solution consisted in 40 mM phosphate buffer (pH 8.0), 170 mM NaCl with 0.1 mg/ml monomeric α-syn and 10 µM ThT. The only differences with the published protocol were the absence of SDS, the use of wild-type α-syn instead of the mutated form K23Q which the scientists used in their work and the monomerization procedure with NaOH that is described in paragraph 2.3. In each well we also put 6 glass beads with a diameter of 1 mm each. The incubation/shaking protocol of Groveman et al.[54] consists of cycles of 1 minute shaking at 400 rpm and 1 minute rest at the temperature of 42°C. In our experiments we did not observe any increase of fluorescence in any sample containing CSF within 140 h. We performed again this test by substituting the reaction buffer with PBS at pH 7.4 (with the same concentrations of ThT and α-syn), this time some of the wells produced fluorescence and the results are shown in Fig. 2.4.3. Although some of the wells produced fluorescence, not all CSF from PD patients reacted to the added α-syn monomer while other samples, in which the CSF of OND subjects was inserted, reacted earlier. At this pH, still we detected poor aggregation and the samples which produced relevant amounts of fibrils were the ones without CSF and the ones with a preformed quantity of synthetic seeds.

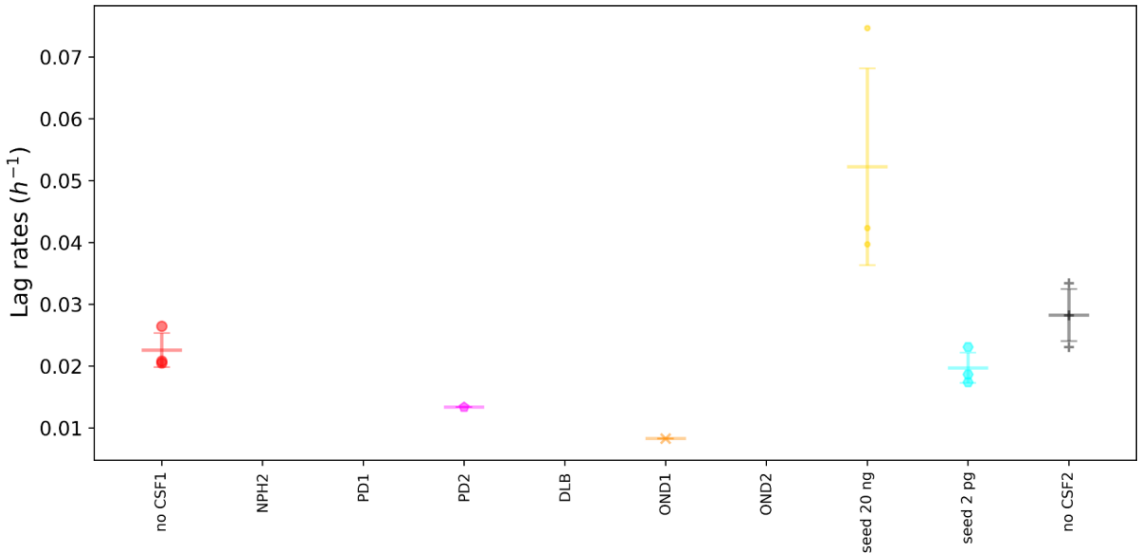

Fig. 2.4.3 RT-QuIC assay performed using 0.08 mg/mL of recombinant α-syn in PBS pH 7.4 with 15 µl of CSF (final volume of 100 µl) coming from PD, DLB, OND and NPH patients in the presence of 6 glass beads with a diameter of 1.0 mm. The lag-rates relative to all the samples are shown.

The experiment was successively repeated on four patients and four controls (OND) by adding with respect to this last case 0.015% SDS and bringing the final NaCl concentration to 500 mM. The protein concentration was also raised from 0.08 to 0.3 mg/ml. A box-plot relative to this last set of experiments is shown below in Fig. 2.4.4.

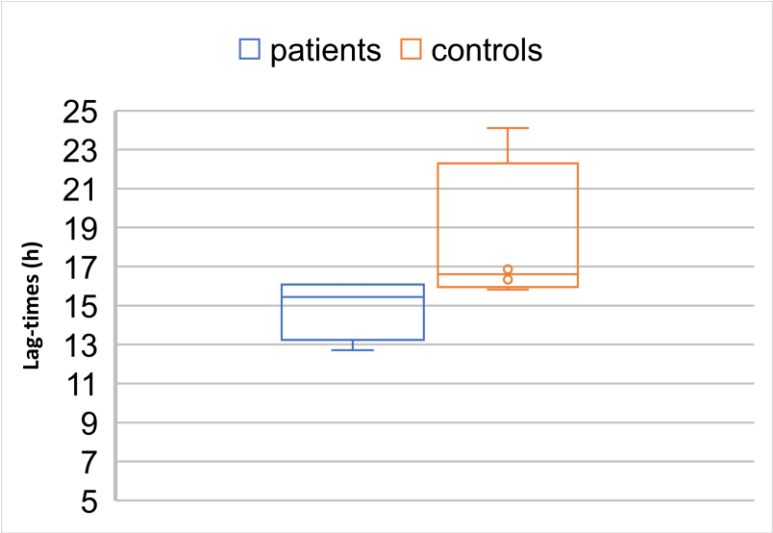

Fig. 2.4.4 The lag-times relative to patients and controls, averaged on replicates were calculated by the formula in Eq. 2.3.3 by using the average fluorescence on the first 5 h instead of 10 h. the RT-QuIC assay was performed using 0.1 mg/mL of recombinant α-syn in PBS pH 7.4 with 15 µl of CSF (final volume of 100 µl) coming from 2 PD and 2 DLB patients and 4 OND controls in the presence of 6 glass beads with a diameter of 1.0 mm. The lag-times relative to all the samples are shown. The samples were subjected to incubation/shaking protocol of cycles of 1-minute shaking at 400 rpm and 1-minute rest at the temperature of 42°C.

Although the changes on the experimental condition accelerated too much the aggregation of α-syn, this last trial produced a better discrimination between samples containing CSF coming from patients affected by synucleinopathies and OND controls.

Discussion and perspectives

Although in the last set of experiments we obtained a better differentiation in a small number of CSFs coming from patients and controls (Fig. 2.4.4), still we cannot explain why other tests we performed did not provide such differentiation. Among all the groups working on these techniques in Italy (Bologna, Milan, Perugia, Padova, Verona and Rome) no one is nowadays able to reproduce the results obtained by the three major groups working on PMCA[52] and RT-QuIC[53,54] for the diagnosis of synucleinopathies. In our experiments, we determined the antiaggregatory effect of CSF as one of the main variables affecting α-syn aggregation, this effect was previously observed by the group of Soto[52] but not investigated. The unknown compounds present in CSF that can modulate α-syn aggregation may be responsible to the high variability between the lag-times measured for different CSFs, the fact that some authors obtained good results also considering this effect may imply that certain experimental strategies (e.g. the addition of SDS, sample handling and storage) may be useful to compensate or normalize the antiaggregatory effect of human CSF. Apart from

increasing the number of CSFs in our tests and optimizing the experimental setup, due to the clinical importance of the development of this assay, for the future we hope to get more in contact with other groups working on RT-QuIC and PMCA to figure out the best strategies to optimize the sensitivity and specificity of the technique. The multiple variables influencing α-syn aggregation in the presence of biofluids imply that a global effort should be performed in order to test as many conditions as possible and standardize the experimental procedures. Although the antiaggregatory effect of CSF is dramatically important for the development of protein aggregation assays for the diagnosis of synucleinopathies, the isolation of the endogenous macromolecules able to interfere with the aggregation of α-syn, will provide information about the physiological proteostasis of α-syn in CSF and on novel possible targets for PD treatment or prevention strategies. The CSF plays a key role in the brain glymphatic system[74,75] and the deficiency of one of these components, with a consequent decreased waste-clearing ability of CSF,[76] may be implicated in the pathogenesis of PD and other synucleinopathies.[77]

3 Proteostasis of α-syn in biological fluids

3.1 Overview

Since 1995, when α-syn was recognized as amyloidogenic protein[78] and few years later as the main component of Lewy bodies,[40] the scientific community started to investigate its physiology in the cytosol (α-syn accounts for about 1% of the cytosolic proteins in brain cells[79]) and what changes or misfunctions in the cytosolic environment can lead to the onset of amyloidoses.[4] The interaction with membranes,[80,81] molecular chaperones[82–84] and the impairment of lysosomal[26,85] and proteasomal[17,86] functions showed to be some of the most important variables regulating the folding of α-syn and the removal of amyloidogenic aggregates inside the cell. Nowadays the spreading of α-syn misfolding in PD and other synucleinopathies is thought to be both systemic (produced by lysosomal and proteasomal dysfunctions) and *prionic* (spreading of the misfolding from cell to cell).[6,7,25,87] The prion-like transmission of α-syn misfolding was thought to be mostly exerted through axons and synaptic terminals.[77,88] Anyway, since almost a decade, the discovery of pathological α-syn aggregates in CSF[25,50] led to a better comprehension of other mechanism of transmission, like passive diffusion and exosomal pathways.[25,51,89] The presence of misfolded α-syn in CSF brought to development of protein aggregation assays for the detection of prone to aggregation α-syn in CSF. These assays opened new doors for the presymptomatic diagnosis of synucleinopathies,[24,52–55,90] while the discovery of the aggregates clearance ability of the CSF-related glymphatic system in amyloid related diseases[27,74,75] highlighted possible new therapeutic strategies.[91] In this context, the comprehension of the interaction of α-syn with CSF and other biofluids (the subject of the following chapter) becomes extremely important. The data presented in paragraph 2.3.1 showed that the human cerebrospinal fluid somehow interacts with monomeric α-syn and strongly inhibits its aggregation, suggesting the existence of physiological mechanisms of α-synuclein proteostasis in CSF. This chapter aims to unveil some of the endogenous compounds present in the human CSF that are responsible for the inhibitory effect and to characterize their interaction with monomeric and aggregated α-synuclein.

We started our analysis by measuring the effects on α-syn aggregation of HSA and human plasma-derived HDL, since some commercial products were easily accessible and because:

- HSA is the most abundant protein in serum and CSF (although is hugely diluted compared to serum) and recently showed an inhibitory effect on α-synuclein aggregation.
- CSF HDL showed anti-aggregation properties, inhibiting the aggregation of Aβ,[30] and it is also established that α-syn has many similarities with apolipoproteins and interacts with them.[92]

Solution NMR with ^{15}N labelled recombinant α-synuclein and protein aggregation assays were used to characterize the interaction and quantify the strength of the inhibitory effect of each selected commercially available compound on α-synuclein aggregation.

The outcome of this line of research will provide a better comprehension of the onset of neurological disorders and the impact of ageing on α-synuclein proteostasis in CSF and other biofluids, highlighting endogenous compounds that may be suitable targets for drug discovery. Moreover, a better understanding of the inhibitory effect of CSF would be of great interest for further developments of the RT-QuIC assay for the diagnosis of synucleinopathies, which mainly relies on the monitoring of the aggregation of α-synuclein in presence of CSF.

3.2 Human serum albumin and α-synuclein (accepted manuscript)

THE JOURNAL OF PHYSICAL CHEMISTRY B

Subscriber access provided by BUFFALO STATE

B: Biophysics; Physical Chemistry of Biological Systems and Biomolecules

Dissecting the Interactions between Human Serum Albumin and #-Synuclein: New Insights on the Factors Influencing #-Synuclein Aggregation in Biological Fluids

Giovanni Bellomo, Sara Bologna, Linda Cerofolini, Silvia Paciotti, Leonardo Gatticchi, Enrico Ravera, Lucilla Parnetti, Marco Fragai, and Claudio Luchinat

J. Phys. Chem. B, **Just Accepted Manuscript** • Publication Date (Web): 29 Apr 2019

Downloaded from http://pubs.acs.org on April 30, 2019

Just Accepted

"Just Accepted" manuscripts have been peer-reviewed and accepted for publication. They are posted online prior to technical editing, formatting for publication and author proofing. The American Chemical Society provides "Just Accepted" as a service to the research community to expedite the dissemination of scientific material as soon as possible after acceptance. "Just Accepted" manuscripts appear in full in PDF format accompanied by an HTML abstract. "Just Accepted" manuscripts have been fully peer reviewed, but should not be considered the official version of record. They are citable by the Digital Object Identifier (DOI®). "Just Accepted" is an optional service offered to authors. Therefore, the "Just Accepted" Web site may not include all articles that will be published in the journal. After a manuscript is technically edited and formatted, it will be removed from the "Just Accepted" Web site and published as an ASAP article. Note that technical editing may introduce minor changes to the manuscript text and/or graphics which could affect content, and all legal disclaimers and ethical guidelines that apply to the journal pertain. ACS cannot be held responsible for errors or consequences arising from the use of information contained in these "Just Accepted" manuscripts.

ACS Publications

is published by the American Chemical Society. 1155 Sixteenth Street N.W., Washington, DC 20036

Published by American Chemical Society. Copyright © American Chemical Society. However, no copyright claim is made to original U.S. Government works, or works produced by employees of any Commonwealth realm Crown government in the course of their duties.

Dissecting the Interactions between Human Serum Albumin and α-synuclein: New Insights on The Factors Influencing α-synuclein Aggregation in Biological Fluids

Giovanni Bellomo,[a] *Sara Bologna,[a] Linda Cerofolini,[a] Silvia Paciotti,[c] Leonardo Gatticchi,[c] Enrico Ravera,[a,b] Lucilla Parnetti,[d*] Marco Fragai[a,b*] and Claudio Luchinat[a,b*]*

[a]*Magnetic Resonance Center (CERM), University of Florence, Via L. Sacconi 6, 50019 Sesto Fiorentino, Italy*

[b]*Department of Chemistry "Ugo Schiff", University of Florence, Via della Lastruccia 3, 50019 Sesto Fiorentino, Italy*

[c]*University of Perugia, Department of Experimental Medicine, Piazzale Gambuli 1, 06132 Perugia, Italy*

[d]*Clinica Neurologica, Università degli Studi di Perugia, Piazzale Gambuli 1, 06132 Perugia, Italy*

**E-mail: claudioluchinat@cerm.unifi.it. Phone: +39 055 4574296*

**E-mail: fragai@cerm.unifi.it. Phone: +39 055 4574261*

**E-mail: lucilla.parnetti@unipg.it. Phone: +39 0755783545*

ABSTRACT: α-synuclein (α-syn) is found to be naturally present in biofluids such as cerebrospinal fluid (CSF) and serum. Human serum albumin (HSA) is the most abundant protein found in these biofluids and, beyond transporting hormones and drugs, it also exerts a chaperone-like activity binding other proteins in blood and inhibiting their aggregation. Contrasting results are reported in literature about the effects of albumin on α-syn aggregation. We characterized the binding region of HSA on α-syn by high-field solution Nuclear Magnetic Resonance (NMR) spectroscopy and the effect of HSA on α-syn aggregation by Thioflavin-T (ThT) fluorescence both in low ionic strength and physiological conditions at the albumin concentration in serum and CSF. We found that HSA, at the concentration found in human serum, slows the aggregation of α-syn significantly. α-syn interacts with HSA in an ionic strength and pH dependent manner. The binding is driven by hydrophobic interactions at the N-terminus in physiological experimental conditions, and by electrostatic interactions at the C-terminus at low ionic strength. This work provides novel information about the proteostasis of α-syn in biofluids and supports the hypothesis of a chaperone-like behavior of HSA.

INTRODUCTION

The misfolding and uncontrolled aggregation of α-synuclein (α-syn) is linked to the onset and progression of a branch of neurological disorders named synucleinopathies, which include Parkinson's disease (PD).[1] Monomeric and oligomeric α-syn have been found to be present in biological fluids[2] such as saliva,[3] cerebrospinal fluid (CSF),[4] serum and plasma.[5] Because α-syn is highly expressed in blood cells,[6] plasma levels of α-synuclein are about 30 folds higher than those of CSF[7] and α-syn showed to be able to cross the Brain-Blood Barrier (BBB) bidirectionally,[8] also involving exosomal pathways.[7] These findings suggest that both free and exosomal α-syn found in CSF may be originated from blood and *vice versa*. The implications of extracellular spreading of α-syn through biological fluids in the development of neurological disorders[9] raised doubts about the proteostasis of α-syn in biofluids, if the misfolding could start in these environments and if extracellular α-synuclein species could work as a biomarker for disease onset and progression. The interest on detecting exosomal, oligomeric and total α-syn in biological fluids (especially in CSF and serum), is increasing due to the need of identifying new biomarkers for an accurate and timely diagnosis.[10,11] However, modest results have been obtained so far by using ELISA detected α-syn species[10] and, nowadays, the diagnosis of PD and other synucleinopathies still relies mainly on clinical symptoms. In this respect, the recent developments of Real Time Quaking Induced Conversion (RT-QuIC) and α-syn Protein Misfolding Cyclic Amplification (PMCA)[12–15] opened new perspectives for the early-stage diagnosis of synucleinopathies. These assays work by amplifying a small amount of preformed aggregates by measuring the aggregation rate of recombinant α-syn monomers added to a solution containing an aliquot of a biological fluid. Thus, also for the optimization of these promising techniques, it is necessary to obtain information about α-syn proteostasis and its interaction with the most

abundant compounds or macromolecules present in biofluids, which can influence its aggregation. Human serum albumin (HSA) is the most abundant protein found in serum[16] (HSA average concentration ~640 μM) and CSF [16] (HSA average concentration ~4.5 μM). HSA is a 66.5 kDa transport protein that has multiple functions in human biofluids, among them, it helps in maintaining the oncotic pressure and transports thyroid hormones, fatty acids and drugs.[17] More recently, HSA was also found to exert a chaperone-like activity.[18] HSA binds Aβ peptides in blood plasma[19] and has been reported to inhibit Aβ fibrillization.[20] The mechanism of an inhibitory effect of HSA on α-syn aggregation and membrane damage, produced by α-syn aggregates, has been also characterized in 2018 by Thioflavin T (ThT) kinetic assay, transmission electron microscopy and with a hemolysis assay.[21] However, the experiments performed in this study were obtained in pure water, in ionic strength conditions far from the physiological ones. Moreover, these results appear in contrast with two previously published studies of 2002[22] and 2004,[23] which showed that Bovine Serum Albumin (BSA), which presents 76% sequence identity with HSA,[24] promotes the fibrillization of α-syn, due to excluded volume effects, in phosphate buffer with nearly physiological concentrations, pH and ionic strength. To shed light on these contradictions and to clarify the partnership between α-syn and the most common protein in serum and CSF, here we characterize the binding region of HSA on α-syn by high field solution NMR and the inhibitory effect of HSA on α-syn aggregation kinetics by ThT fluorescence assays both in low ionic strength environment and physiological conditions.

MATERIALS AND METHODS

α-synuclein Expression and Purification. Escherichia Coli BL21(DE3)Gold were transformed with pT7-7 vector cloned with the gene encoding α-synuclein. The overnight preculture of transformed cells was diluted 100-fold in LB medium and induced at an OD_{600} value of 0.6-0.8 with 1 mM Isopropyl-β-D-thiogalactoside and, after 5 hours incubation at 37 °C, the cells were harvested at 4000 rpm (JA-10, Beckman Coulter). The extraction was carried out through osmotic shock using 100 ml of buffer TRIS 30 mM, EDTA 2 mM and sucrose 40%, at pH 7.2 according to Shevchik et al. [25] and Huang et al.. [26] The suspension was then ultracentrifuged at 20000 rpm (Type 70 Ti rotor, Beckman Coulter) for 25 min and pellet was collected and resuspended with 90 ml precooled ultrapure water additioned with 38 µl of $MgCl_2$ 1 M and then ultracentrifuged a second time. Surnatants derived from these two centrifugation steps, were joined and dialyzed against 4 L of buffer 20 mM TRIS/HCl at pH 8.0. The protein then was loaded in the FPLC system and an anion exchange chromatography was carried out with 0-50% linear gradient NaCl 1 M (GE Healthcare HiPrep™ Q HP 16/10 Column). The collected fractions were lyophilized and resuspended in 10 mM TRIS/HCl, 1 mM EDTA and urea 8 M at pH 8.0 for the chemical denaturation. To eliminate all the protein formed aggregates, two size-exclusion chromatographies (HiLoad™ 16/600 Superdex™ 75 pg Column) were performed with 20 mM phosphate and 0.5 mM EDTA at pH 8.0 as elution buffer. Purified α-synuclein (α-syn) was dialyzed against Milli-Q water and lyophilized in batches for long-term storage. Roche cOmplete™ protease inhibitor cocktail was added only during the extraction step in the quantity suggested by the producer.

ThT aggregation experiments

The lyophilized aliquots α-syn were resuspended in NaOH 3.5 mM (pH 11.54) right before the experiments to avoid the instantaneous formation of aggregates. At high pH, the negatively charged monomers (the isoelectric point of α-syn is 4.67) experience an

electrostatic repulsion that impedes the aggregation and favors the dissociation of small aggregates.[27,28]

Setup of ThT Aggregation Experiments in KPi. The solution of α-syn and NaOH was brought to pH 6.0 and to desired α-syn concentration by diluting it with potassium phosphate buffer. The final samples, of 600 µL each, contained 20 mM KPi, 50 mM NaCl, 50 µM α-syn, 0.1% NaN_3, 10 µM ThT and 0, 50, and 640 µM HSA. Each sample was then split in 3 replicates of 200 µL that were then put in a TECAN clear-bottom 96-well plate. We added glass beads in each well (21x 0.5 mm dimeter glass beads), to enhance aggregation speed and increase homogeneity among replicates.[29] Successively, the plate was inserted in a BMG LABTECH ClarioStar® fluorimeter and subjected to an incubation/shaking protocol similar to the one used by Shahnawaz et al.[30] (T = 310 K, 29 min. incubation, 1 min. shaking at 500 rpm). At every cycle of 30 min. the fluorescence was read from the bottom using an excitation and emission wavelength of 450 nm and 480 nm, respectively.

Setup of ThT Aggregation Experiments in PBS. The solution containing α-syn and NaOH was brought to pH 7.4 and to the desired α-syn concentration with concentrated PBS buffer. The final samples, of 600 µL each, contained standard PBS, 100 µM α-syn, 0.1% NaN_3, 10 µM ThT and 0, 4.5, 100 and 640 µM HSA. Each sample was then split in 3 replicates of 200 µL that were then put in a TECAN clear-bottom 96-well plate. Analogous samples containing 4.5, 100 and 640 µM HSA without α-syn were also prepared to monitor the background fluorescence of ThT bound to HSA. We added glass beads in each well (6 x 1 mm dimeter glass beads), to enhance aggregation speed and increase homogeneity among replicates.[29] The plate was then inserted in a BMG LABTECH ClarioStar® fluorimeter and subjected to an incubation/shaking protocol similar to the one used by Shahnawaz et al.[30] (T = 310 K, 29 min. incubation, 1 min. shaking at 500 rpm). At every cycle of 30 min. the fluorescence was read from the bottom using an excitation and emission wavelength of

450 nm and 480 nm, respectively. In this sample we observed a progressive decrease of the background fluorescence produced by ThT bound to HSA that was not evident in KPi at pH 6.0 (see Fig. S1). The decrease of the offset fluorescence may be due to the change of oligomeric populations of HSA, which have an higher binding affinity for ThT compared to the monomer[31] and a partial dissociation of these multimers, due to the higher pH compared to the previous experiments in KPi, may be the cause of that slow decrease.

Definition of the t_0 and t_{lag} Parameters. To quantitatively estimate the lag-phase from ThT fluorescence profiles, we fit the data coming from each well (without removing the offset and without normalizing) with a Boltzmann's sigmoidal function (Eq. 1), using OriginPro 9. In the non-linear curve fitting procedure used, the parameters A_1, A_2, t_0 and dt of Eq. 1 were let free.

$$y(t) = A_2 + \frac{A_1 - A_2}{1 + \exp\left(\frac{t - t_0}{dt}\right)} \quad (1)$$

The parameter t_0 corresponds to the inflection point of the sigmoidal curves used to fit the data and can be used to quantify the time necessary to produce a consistent quantity of fibrillary aggregates.

Conversely, the t_{lag} parameter quantifies the time at which fibrils start to form. We defined it, in a way similar to the one used by Groveman *et al.*,[14] as the time at which the fluorescence (F) of a well becomes higher than its average fluorescence in the first 5 h ($\overline{F(t)}_{t<5\,h}$) plus 2 standard deviations (2σ), for 5 consecutive measurements:

$$F(t_{lag} + i\Delta t) \geq \overline{F(t)}_{t<5\,h} + 2\sigma(F(t))_{t<5\,h};\ \forall\, i \in (0, 1, 2, 3, 4) \quad (2)$$

Where Δt is the time between two consecutive measurements.

NMR Experiments. All the NMR spectra were acquired at 283 K with a Bruker Avance III HD NMR spectrometer operating at 950 MHz ^{1}H Larmor frequency, equipped with a cryogenically cooled probe. The spectra were processed with the Bruker TOPSPIN 4.0 software tools and analyzed by the program Computer Aided Resonance Assignment.[32] During the NMR titration of the protein with HSA, 3 aliquots of a concentrated 8 mM solution of HSA (same buffer conditions of the final samples) were added to the buffered solution containing ^{15}N isotopically enriched α-syn at the concentration of 100 μM. The tested buffered solutions were: [20 mM KPi, pH 6.0 with 50, 100 and 150 mM NaCl] and PBS (pH 7.4). For samples in PBS buffer we also added 0.5 mM of EDTA to block residual traces of metalloproteases. For the NMR experiments, standard 3 mm glass tubes were used with a final sample volume of 200 μL. The added volumes of the HSA solution (8 mM) were 2.5, 17.5 and 25.5 μL for the 100, 640 and 900 μM samples, respectively, in all the buffer used. While testing the electrostatic nature of the interaction between α-syn and HSA, also 2 μL and 4 μL of a solution of 20 mM KPi, pH 6.0 with 5 M NaCl were added in the NMR tube containing α-syn 100 μM and HSA 900 μM, to reach the final concentration of 100 and 150 mM NaCl, respectively.

RESULTS AND DISCUSSION

At first, to test the possible inhibitory effect of HSA on α-syn fibrillization, monomeric recombinant α-syn (at the concentration of 50 μM) was incubated alone or in the presence of different amounts of HSA (50 μM and 640 μM) in a potassium phosphate buffer (KPi, 20 mM potassium phosphate, 50 mM NaCl, pH 6.0). The protocols used for the expression, purification and resuspension of α-syn are present in *MATERIALS AND METHODS*. We applied a PMCA protocol[13] and added glass beads (21 x 0.5 mm diameter glass beads) inside the wells to increase the homogeneity among replicates[29] and speed up the

aggregation of α-syn. The outcome of the ThT fluorescence experiment performed in KPi is summarized in Fig. 1A. To better visualize the difference in the lag-phases in the figure, for each well, we removed the background fluorescence produced by ThT bound to HSA and averaged the results of the three replicates prepared for each HSA concentration. Both monomeric and multimeric HSA bind ThT with a K_D of ~140 μM and ~20 μM, respectively,[31] thus producing a background fluorescence. To remove this offset in fluorescence intensity, we subtracted the average fluorescence value of the first 10 h, where the fluorescence was constant and produced mostly by ThT bound to HSA (Fig. 1A).

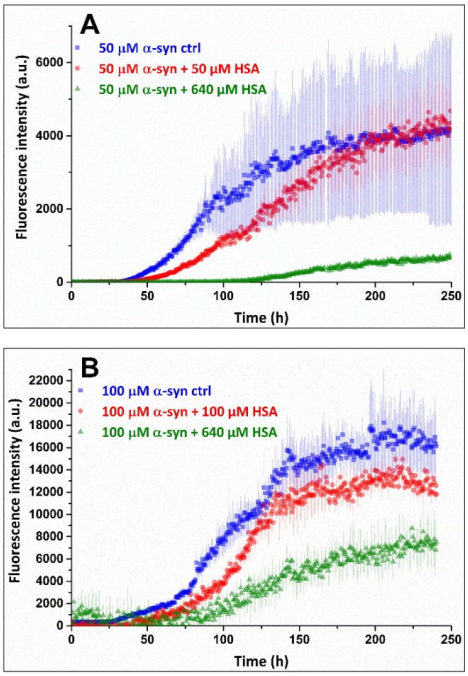

Fig. 1 A) *Monomeric α-syn 50 μM was left aggregating in the presence of ThT 10 μM and different HSA concentrations. The experiments were performed in triplicate in a 96-wells plate in KPi buffer (KPi 20 mM, 50 mM NaCl, pH 6.0, T = 310 K). 21 x 0.5 mm diameter glass beads were added to the samples.* ***B)*** *Monomeric α-syn 100 μM was left aggregating in the presence of ThT 10 μM and increasing HSA concentrations. The experiments were performed in triplicate in a 96-wells plate in PBS pH 7.4, T = 310 K. Glass beads (6 x 1mm diameter) were added to the samples. In both experiments, samples were subjected to cycles of shaking (1 min. shaking 500 rpm, 29 min. rest) inside a BMG Labtech ClarioStar fluorimeter. The shown kinetic profiles result from the averages and standard deviation of the averages made on the three replicates with offset removed.*

The measured t_0 parameters (defined in *MATERIALS AND METHODS*), averaged on the three replicates, are reported in Table 1. As can be evinced from the table, the estimated t_0 are longer for samples containing HSA in KPi, both at its physiological concentration in serum (640 μM) and in 1:1 ratio with α-syn (50 μM). Successively, the experiments were repeated in a different buffer under more physiological experimental conditions: phosphate buffered saline (PBS: 137 mM NaCl, 10 mM Na_2HPO_4, 2 mM KH_2HPO_4, 2.7 mM KCl, pH 7.4). In this second set of experiments, the concentration of α-syn was raised to 100 μM and the size and the number of the glass beads were changed from 21 x 0.5 mm diameter beads to 6 x 1 mm dimeter beads. The change in the experimental setup was made to further encourage the fibrillization of α-syn. Indeed, the higher pH value slowed down the whole aggregation process because of the electrostatic repulsion between α-syn monomers that become more negatively charged while increasing the pH.[33] For the PBS experiments, α-syn was incubated alone and with increasing quantities of HSA: 4.5 μM (shown in the SI, physiological concentration in CSF), 100 μM and 640 μM. At high HSA concentration (100

μM and 640 μM), we observed a progressive decrease of the background fluorescence of HSA over time (Fig. S1 in the SI). We hypothesize that this was due to a slight change in the oligomeric populations of HSA which have different binding affinity for ThT.[31] To overcome this problem, the average fluorescence of three replicates in wells containing HSA alone was subtracted from the fluorescence of the wells containing both HSA and α-syn. We measured the t_0 values of each well by fitting the data with the background removed. The averaged t_0 values are shown in Table 1, while the averaged ThT profiles with offset removed are shown in Fig. 1B. Also, in this last set of ThT aggregation experiments we observed an increased t_0 for samples containing HSA. A strong decrease in the amplitudes of the fitted sigmoids (A_1-A_2) was also observed for samples with 640 μM HSA (see Fig. 2 and Table S1 in the SI) but, although ThT is a good probe for fibril formation, caution should be used in interpreting this result, since HSA competes with α-syn fibrils in binding ThT. Another parameter which can be useful to characterize the speed of the aggregation is the time at which the fluorescence starts to deviate significantly from its initial value (t_{lag}) that we defined in *Materials and Methods*. The measured t_{lag} values are present in Table 1.

Table 1 t_0 and t_{lag} Parameters for the Experiments Performed with 50 μM α-syn in 20 mM KPi, 50 mM NaCl, pH 6.0, T = 310 K and 100 μM α-syn in PBS, pH 7.4, T = 310 K

Experiment	HS	t_0	t_{lag}
50 μM α-syn 20 mM KPi, 50 mM NaCl, pH 6	0	8	27
	50	1	29
	640	1	119
100 μM α-syn PBS, pH 7.4	0	1	28.
	4.5	1	30
	100	1	61
	640	1	130

The values present in the table result from the average on three replicates while their uncertainty corresponds to the standard deviation of the average value.

Although the physiological concentration of HSA in serum produced the most marked effects both on the t_0 and t_{lag} of the kinetic profiles, in our experiments, the physiological

HSA concentration in CSF still was able to generate a slight delay in the aggregation of 100 μM α-syn in PBS (Fig. S2 in the SI). It produced a t_{lag} of 30 h and a t_0 of 116 h on the aggregation of 100 μM α-syn, with the t_{lag} and t_0 of the control sample being 28 h and 105 h, respectively. This t_0 is comparable to that produced by 100 μM HSA, although this sample produced a longer t_{lag} (61 h).

To clarify the molecular basis of the inhibition of α-syn aggregation by HSA, the interaction between the two proteins was investigated through solution NMR. We added different aliquots of HSA (100 μM, 640 μM and 900 μM) to solutions of ^{15}N isotopically enriched α-syn (100 μM) and evaluated the changes in intensity of the resonances in 2D ^{1}H ^{15}N HSQC solution NMR spectra. We also tested lower amounts of HSA in the same conditions but negligible variations were observed up to 100 μM HSA (Fig. S6 in the SI). The experiments were performed on a Bruker Avance III HD 950 MHz NMR spectrometer, at 283 K in the same two buffers previously used for the fluorimetric assays. The data relative to the experiments performed at 100 and 640 μM HSA and the experimental details about the measurements are presented in the SI. In the presence of HSA, several signals in the 2D ^{1}H-^{15}N HSQC of α-syn experienced large decreases in intensity, because of a line broadening effect on these cross-peaks, arising after the interaction with HSA. In low ionic strength environment (Fig. 2A), the residues located on the C-terminus of α-syn are mainly affected by this decrease, indicating an interaction with HSA occurring at this level.

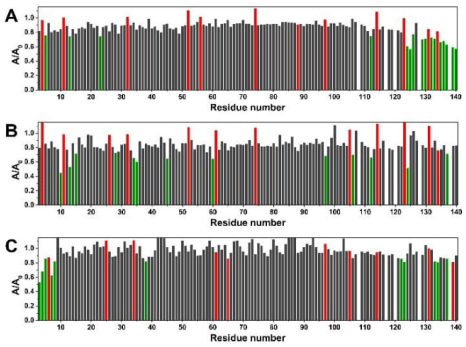

Fig. 2 Intensity decreases of the signals of 2D ^{15}N ^{1}H HSQC experiments acquired at 950 MHz on α-syn (100 μM) after the addition of HSA (900 μM) at T = 283 K in different buffer conditions: **A)** KPi 20 mM, NaCl 50 mM pH 6.0; **B)** KPi 20 mM, NaCl 150 mM pH 6.0; C) PBS (NaCl 137 mM) pH 7.4. The residues experiencing the largest decreases in signal intensity (smaller by one or more standard deviation with respect to the average value) are highlighted in green. The intensity ratios corresponding to overlapping peaks are highlighted in red (their values were not considered in the calculation of the average decreases and standard deviations).

We hypothesize that this interaction is mainly electrostatic: by calculating the charge of HSA with the APBS[34] plugin of PyMOL, we found a positively charged pocket (see Fig. 3) that may be an eligible site for the interaction with the negatively charged C-terminus of α-syn.

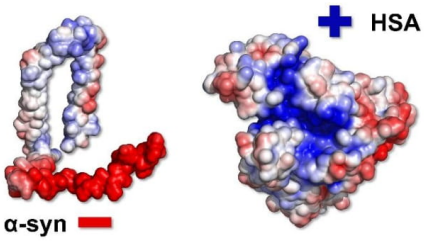

Fig. 3 Surface charge representation of α-syn (PDB code: 2KKW, conformer n°2) and HSA (PDB code: 4K2C), with blue and red representing regions of positive and negative electrostatic potential, respectively. All the electrostatic surfaces were generated with the APBS plugin of PyMOL. Different scales of dimensions of the two proteins are used in the figure.

As a support for the electrostatic interaction hypothesis, we also found that the effect on these resonances can be decreased by increasing the ionic strength of the solution (Fig. 2B). Nevertheless, also at higher ionic strength, α-syn interacts with HSA but mostly by residues located on its amphipathic N-terminus, as shown by the intensity decrease of the amide cross-peaks of residues Lys10, Glu13 and Val15 (Fig. 2B). Another different behavior was observed in PBS, at more physiological salt concentration and pH value. In this environment, α-syn is still able to slightly interact with HSA by its C-terminus but the interaction is mainly located at the N-terminus (Fig. 2C), with a pattern similar to that previously reported in the literature,[35] where the interaction of BSA with α-syn was evaluated in PBS buffer. The region Val3-Lys8 (there is no information available for residues 1,2) seems to be particularly involved in this interaction. The residues highlighted in Fig. 2C are different with respect to those highlighted in Fig. 2B, probably due to the pH change (from pH 6.0 to pH 7.4) and the slight difference in ionic strength.

CONCLUSIONS

In conclusion, HSA, at the concentration found in human serum, slows the aggregation of α-syn significantly, supporting the hypothesis of the chaperone-like behavior of HSA. α-syn is found to interact with HSA in an ionic strength and pH dependent manner.

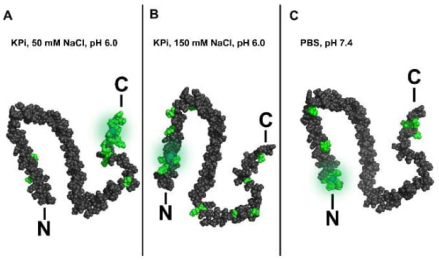

Fig. 4 The residues experiencing the largest effects are highlighted in green on α-syn structure (PDB code: 2KKW, conformer n°13). **A)** KPi buffer (50 mM NaCl, pH 6.0), **B)** KPi buffer (150 mM NaCl, pH 6.0) and **C)** PBS buffer (137 mM NaCl, pH 7.4).

In KPi buffer, pH 6.0, at low ionic strength (50 mM NaCl), α-syn binds HSA with its negatively charged C-terminus (Fig. 4A), especially involving the region from Glu123 to Ala140. Conversely, with the addition of 100 mM NaCl to the solution, the intensity of many signals belonging to the C-terminus is restored, and the dominant effect involves residues located in the N-terminus (Fig. 4B), with Lys10, Glu13 and Val15 being the residues with the most decreased signal intensities in the 2D ^{1}H ^{15}N HSQC spectrum. In physiological conditions (Fig. 4C), the interaction is mainly located at the amphipathic N-terminus of α-syn, in the region Val3-Lys8 with a weak residual interaction at the C-terminus involving Asn122-Glu123 and Tyr133-Glu137. The absence of relevant chemical shifts variations or appearance of new peaks in ^{15}N ^{1}H HSQC experiments, both in low and physiological ionic strength environments, suggests that the interaction between HSA and monomeric α-syn occurs in the intermediate exchange regime, thus with a dissociation constant in the low micromolar range, assuming a diffusion-controlled association regime.[36] However, the interactions involving intrinsically disordered proteins like α-syn are generally heterogeneous, difficult to characterize and only upper limits can be usually provided for affinity and dissociation constants.[37] We thus hypothesize that HSA, due to its high concentration, could bind monomeric α-syn in serum on its N-terminus and impede its aggregation, in a manner similar to the one observed for Aβ.[18,20,37] The extended t_0 and t_{lag} of the ThT aggregation profiles and the direct interaction with α-syn monomer observed by NMR imply a possible stabilization of α-syn monomers[38] that interferes with the primary nucleation and elongation of the aggregates.[39–41] However, the observed direct interaction

between HSA and monomeric α-syn does not exclude that other mechanisms involving oligomeric and prefibrillar intermediates may contribute to the observed antiaggregatory effect of HSA on α-syn fibrillization. The data reported in Fig. 1 and Table S1 show that, apart from the strong effect on t_0 and t_{lag}, the addition of HSA produced also a general decrease in the fitted A1-A2 parameter of Eq. 1, which may be a consequence of both the interaction of HSA with α-syn monomers and the interaction with oligomeric or prefibrillar intermediates. Generally, also the presence of negatively charged proteins at high concentration may lead to an overall increased repulsion in solution and increased solution stability, which may also contribute to α-syn aggregation inhibition, particularly in low ionic strength environments.[42] The characterization of the partnership between α-syn and HSA is not only a first step in the comprehension of the proteostasis of α-syn in biological fluids but should be also considered in the development of α-syn PMCA and RT-QuIC assays. The albumin content varies among CSF of patients, because of the different blood-brain barrier permeability and/or blood contamination of samples.[43] Altered HSA levels in CSF may modulate differently α-syn aggregation, increasing false negatives and positives in the clinical trials of these assays. Excluding blood-contaminated samples or normalizing the protein content of CSF samples prior to the analysis (by diluting samples with a higher protein content of or by adding HSA in samples with a lower protein content) may compensate for this effect.

The authors declare no competing financial interest.

Acknowledgments

This work was supported by ERA-NET NEURON ABETA ID, MIUR PRIN 2012SK7ASN, Fondazione Cassa di Risparmio di Firenze, MEDINTECH (CTN01_001177_962865), the University of Florence CERM-TT, Recombinant Proteins *JOYNLAB* and Instruct-ERIC, an ESFRI Landmark, supported by national member subscriptions. Specifically, we thank the Instruct-ERIC Core Centre CERM, Italy.

Supporting Information

ThT f profiles of α-syn in PBS in the presence of HSA and HSA alone, normalized on the unbound ThT fluorescence *Fig. S1;* ThT aggregation profile of α-syn in PBS in the presence of 4.5 μM of HSA *Fig. S2;* t_0, t_{lag} and A_2-A_1 parameters measured for the experiments performed *Table S1*; portions of 2D ^{15}N ^{1}H HSQC spectra performed in KPi and PBS *Fig. S3*; intensity ratios of peaks coming from 2D ^{15}N ^{1}H HSQC experiments performed in KPi at different concentrations of NaCl *Fig. S4*; intensity ratios of peaks coming from 2D ^{15}N ^{1}H HSQC experiments performed in KPi at 100 μM HSA *Fig. S5*; intensity ratios of peaks coming from 2D ^{15}N ^{1}H HSQC experiments performed in KPi and PBS at 640 μM HSA *Fig. S6*; intensity ratios of peaks coming from 2D ^{15}N ^{1}H HSQC experiments performed in KPi with native and fatty-acid free HSA *Fig. S7*;

REFERENCES

(1) Spillantini, M. G.; Schmidt, M. L.; Lee, V. M.; Trojanowski, J. Q.; Jakes, R.; Goedert, M. Alpha-Synuclein in Lewy Bodies. *Nature* **1997**, *388* (6645), 839–840. https://doi.org/10.1038/42166.

(2) Malek, N.; Swallow, D.; Grosset, K. A.; Anichtchik, O.; Spillantini, M.; Grosset, D. G. Alpha-Synuclein in Peripheral Tissues and Body Fluids as a Biomarker for Parkinson's Disease – a Systematic Review. *Acta Neurologica Scandinavica* **2014**, *130* (2), 59–72. https://doi.org/10.1111/ane.12247.

(3) Kang, W.; Chen, W.; Yang, Q.; Zhang, L.; Zhang, L.; Wang, X.; Dong, F.; Zhao, Y.; Chen, S.; Quinn, T. J.; et al. Salivary Total α-Synuclein, Oligomeric α-Synuclein and SNCA Variants in Parkinson's Disease Patients. *Sci Rep* **2016**, *6*. https://doi.org/10.1038/srep28143.

(4) Farotti, L.; Paciotti, S.; Tasegian, A.; Eusebi, P.; Parnetti, L. Discovery, Validation and Optimization of Cerebrospinal Fluid Biomarkers for Use in Parkinson's Disease. *Expert Rev. Mol. Diagn.* **2017**, *17* (8), 771–780. https://doi.org/10.1080/14737159.2017.1341312.

(5) El-Agnaf, O. M. A.; Salem, S. A.; Paleologou, K. E.; Curran, M. D.; Gibson, M. J.; Court, J. A.; Schlossmacher, M. G.; Allsop, D. Detection of Oligomeric Forms of Alpha-Synuclein Protein in Human Plasma as a Potential Biomarker for Parkinson's Disease. *FASEB J.* **2006**, *20* (3), 419–425. https://doi.org/10.1096/fj.03-1449com.

(6) Barbour, R.; Kling, K.; Anderson, J. P.; Banducci, K.; Cole, T.; Diep, L.; Fox, M.; Goldstein, J. M.; Soriano, F.; Seubert, P.; et al. Red Blood Cells Are the Major Source of Alpha-Synuclein in Blood. *Neurodegener Dis* **2008**, *5* (2), 55–59. https://doi.org/10.1159/000112832.

(7) Shi, M.; Liu, C.; Cook, T. J.; Bullock, K. M.; Zhao, Y.; Ginghina, C.; Li, Y.; Aro, P.; Dator, R.; He, C.; et al. Plasma Exosomal α-Synuclein Is Likely CNS-Derived and Increased in Parkinson's Disease. *Acta Neuropathol.* **2014**, *128* (5), 639–650. https://doi.org/10.1007/s00401-014-1314-y.

(8) Sui, Y.-T.; Bullock, K. M.; Erickson, M. A.; Zhang, J.; Banks, W. A. Alpha Synuclein Is Transported into and out of the Brain by the Blood–Brain Barrier. *Peptides* **2014**, *62*, 197–202. https://doi.org/10.1016/j.peptides.2014.09.018.

(9) Lee, H.-J.; Bae, E.-J.; Lee, S.-J. Extracellular α-Synuclein—a Novel and Crucial Factor in Lewy Body Diseases. *Nature Reviews Neurology* **2014**, *10* (2), 92–98. https://doi.org/10.1038/nrneurol.2013.275.

(10) Eusebi, P.; Giannandrea, D.; Biscetti, L.; Abraha, I.; Chiasserini, D.; Orso, M.; Calabresi, P.; Parnetti, L. Diagnostic Utility of Cerebrospinal Fluid α-Synuclein in Parkinson's Disease: A Systematic Review and Meta-Analysis. *Movement Disorders* **2017**, *32* (10), 1389–1400. https://doi.org/10.1002/mds.27110.

(11) Cerri, S.; Ghezzi, C.; Sampieri, M.; Siani, F.; Avenali, M.; Dornini, G.; Zangaglia, R.; Minafra, B.; Blandini, F. The Exosomal/Total α-Synuclein Ratio in Plasma Is Associated With Glucocerebrosidase Activity and Correlates With Measures of Disease Severity in PD Patients. *Front Cell Neurosci* **2018**, *12*. https://doi.org/10.3389/fncel.2018.00125.

(12) Paciotti, S.; Bellomo, G.; Gatticchi, L.; Parnetti, L. Are We Ready for Detecting α-Synuclein Prone to Aggregation in Patients? The Case of "Protein-Misfolding Cyclic Amplification" and "Real-Time Quaking-Induced Conversion" as Diagnostic Tools. *Front. Neurol.* **2018**, *9*. https://doi.org/10.3389/fneur.2018.00415.

(13) Shahnawaz, M.; Tokuda, T.; Waragai, M.; Mendez, N.; Ishii, R.; Trenkwalder, C.; Mollenhauer, B.; Soto, C. Development of a Biochemical Diagnosis of Parkinson

Disease by Detection of α-Synuclein Misfolded Aggregates in Cerebrospinal Fluid. *JAMA Neurol* **2017**, *74* (2), 163–172. https://doi.org/10.1001/jamaneurol.2016.4547.

(14) Groveman, B. R.; Orrù, C. D.; Hughson, A. G.; Raymond, L. D.; Zanusso, G.; Ghetti, B.; Campbell, K. J.; Safar, J.; Galasko, D.; Caughey, B. Rapid and Ultra-Sensitive Quantitation of Disease-Associated α-Synuclein Seeds in Brain and Cerebrospinal Fluid by ASyn RT-QuIC. *Acta Neuropathologica Communications* **2018**, *6*, 7. https://doi.org/10.1186/s40478-018-0508-2.

(15) Fairfoul, G.; McGuire, L. I.; Pal, S.; Ironside, J. W.; Neumann, J.; Christie, S.; Joachim, C.; Esiri, M.; Evetts, S. G.; Rolinski, M.; et al. Alpha-Synuclein RT-QuIC in the CSF of Patients with Alpha-Synucleinopathies. *Ann Clin Transl Neurol* **2016**, *3* (10), 812–818. https://doi.org/10.1002/acn3.338.

(16) Tibbling, G.; Link, H.; Öhman, S. Principles of Albumin and IgG Analyses in Neurological Disorders. I. Establishment of Reference Values. *Scandinavian Journal of Clinical and Laboratory Investigation* **1977**, *37* (5), 385–390. https://doi.org/10.1080/00365517709091496.

(17) Fanali, G.; di Masi, A.; Trezza, V.; Marino, M.; Fasano, M.; Ascenzi, P. Human Serum Albumin: From Bench to Bedside. *Molecular Aspects of Medicine* **2012**, *33* (3), 209–290. https://doi.org/10.1016/j.mam.2011.12.002.

(18) Finn, T. E.; Nunez, A. C.; Sunde, M.; Easterbrook-Smith, S. B. Serum Albumin Prevents Protein Aggregation and Amyloid Formation and Retains Chaperone-like Activity in the Presence of Physiological Ligands. *J Biol Chem* **2012**, *287* (25), 21530–21540. https://doi.org/10.1074/jbc.M112.372961.

(19) Kuo, Y.-M.; Kokjohn, T. A.; Kalback, W.; Luehrs, D.; Galasko, D. R.; Chevallier, N.; Koo, E. H.; Emmerling, M. R.; Roher, A. E. Amyloid-β Peptides Interact with Plasma Proteins and Erythrocytes: Implications for Their Quantitation in Plasma. *Biochemical*

and Biophysical Research Communications **2000**, *268* (3), 750–756. https://doi.org/10.1006/bbrc.2000.2222.

(20) Stanyon, H. F.; Viles, J. H. Human Serum Albumin Can Regulate Amyloid-β Peptide Fiber Growth in the Brain Interstitium IMPLICATIONS FOR ALZHEIMER DISEASE. *J. Biol. Chem.* **2012**, *287* (33), 28163–28168. https://doi.org/10.1074/jbc.C112.360800.

(21) Kakinen, A.; Javed, I.; Faridi, A.; Davis, T. P.; Ke, P. C. Serum Albumin Impedes the Amyloid Aggregation and Hemolysis of Human Islet Amyloid Polypeptide and Alpha Synuclein. *Biochim. Biophys. Acta* **2018**. https://doi.org/10.1016/j.bbamem.2018.01.015.

(22) Uversky, V. N.; Cooper, E. M.; Bower, K. S.; Li, J.; Fink, A. L. Accelerated α-Synuclein Fibrillation in Crowded Milieu. *FEBS Letters* **2002**, *515* (1–3), 99–103. https://doi.org/10.1016/S0014-5793(02)02446-8.

(23) Munishkina, L. A.; Cooper, E. M.; Uversky, V. N.; Fink, A. L. The Effect of Macromolecular Crowding on Protein Aggregation and Amyloid Fibril Formation. *Journal of Molecular Recognition* **2004**, *17* (5), 456–464. https://doi.org/10.1002/jmr.699.

(24) Carter, D. C.; Ho, J. X. Structure of Serum Albumin. *Adv. Protein Chem.* **1994**, *45*, 153–203.

(25) Shevchik, V. E.; Condemine, G.; Robert-Baudouy, J. Characterization of DsbC, a Periplasmic Protein of Erwinia Chrysanthemi and Escherichia Coli with Disulfide Isomerase Activity. *EMBO J* **1994**, *13* (8), 2007–2012.

(26) Huang, C.; Ren, G.; Zhou, H.; Wang, C. A New Method for Purification of Recombinant Human Alpha-Synuclein in Escherichia Coli. *Protein Expr. Purif.* **2005**, *42* (1), 173–177. https://doi.org/10.1016/j.pep.2005.02.014.

(27) Shammas, S. L.; Knowles, T. P. J.; Baldwin, A. J.; MacPhee, C. E.; Welland, M. E.; Dobson, C. M.; Devlin, G. L. Perturbation of the Stability of Amyloid Fibrils through Alteration of Electrostatic Interactions. *Biophys J* **2011**, *100* (11), 2783–2791. https://doi.org/10.1016/j.bpj.2011.04.039.

(28) Cohlberg, J. A.; Li, J.; Uversky, V. N.; Fink, A. L. Heparin and Other Glycosaminoglycans Stimulate the Formation of Amyloid Fibrils from Alpha-Synuclein in Vitro. *Biochemistry* **2002**, *41* (5), 1502–1511.

(29) Giehm, L.; Otzen, D. E. Strategies to Increase the Reproducibility of Protein Fibrillization in Plate Reader Assays. *Anal. Biochem.* **2010**, *400* (2), 270–281. https://doi.org/10.1016/j.ab.2010.02.001.

(30) Shahnawaz, M.; Tokuda, T.; Waragai, M.; Mendez, N.; Ishii, R.; Trenkwalder, C.; Mollenhauer, B.; Soto, C. Development of a Biochemical Diagnosis of Parkinson Disease by Detection of α-Synuclein Misfolded Aggregates in Cerebrospinal Fluid. *JAMA Neurol* **2017**, *74* (2), 163–172. https://doi.org/10.1001/jamaneurol.2016.4547.

(31) Rovnyagina, N. R.; Sluchanko, N. N.; Tikhonova, T. N.; Fadeev, V. V.; Litskevich, A. Yu.; Maskevich, A. A.; Shirshin, E. A. Binding of Thioflavin T by Albumins: An Underestimated Role of Protein Oligomeric Heterogeneity. *International Journal of Biological Macromolecules* **2018**, *108*, 284–290. https://doi.org/10.1016/j.ijbiomac.2017.12.002.

(32) Keller, R. L. J. Optimizing the Process of Nuclear Magnetic Resonance Spectrum Analysis and Computer Aided Resonance Assignment. Doctoral Thesis, ETH Zurich, 2005. https://doi.org/10.3929/ethz-a-005068942.

(33) Uversky, V. N.; Eliezer, D. Biophysics of Parkinson's Disease: Structure and Aggregation of α-Synuclein. *Curr Protein Pept Sci* **2009**, *10* (5), 483–499.

(34) Baker, N. A.; Sept, D.; Joseph, S.; Holst, M. J.; McCammon, J. A. Electrostatics of Nanosystems: Application to Microtubules and the Ribosome. *PNAS* **2001**, *98* (18), 10037–10041. https://doi.org/10.1073/pnas.181342398.

(35) Theillet, F.-X.; Binolfi, A.; Bekei, B.; Martorana, A.; Rose, H. M.; Stuiver, M.; Verzini, S.; Lorenz, D.; van Rossum, M.; Goldfarb, D.; et al. Structural Disorder of Monomeric α-Synuclein Persists in Mammalian Cells. *Nature* **2016**, *530* (7588), 45–50. https://doi.org/10.1038/nature16531.

(36) Roberts, G. C. K. The Determination of Equilibrium Dissociation Constants of Protein-Ligand Complexes by NMR. In *BioNMR in Drug Research*; John Wiley & Sons, Ltd, 2003; pp 309–319. https://doi.org/10.1002/3527600663.ch13.

(37) Milojevic, J.; Melacini, G. Stoichiometry and Affinity of the Human Serum Albumin-Alzheimer's Aβ Peptide Interactions. *Biophys J* **2011**, *100* (1), 183–192. https://doi.org/10.1016/j.bpj.2010.11.037.

(38) Carija, A.; Pinheiro, F.; Pujols, J.; Brás, I. C.; Lázaro, D. F.; Santambrogio, C.; Grandori, R.; Outeiro, T. F.; Navarro, S.; Ventura, S. Biasing the Native α-Synuclein Conformational Ensemble towards Compact States Abolishes Aggregation and Neurotoxicity. *Redox Biol* **2019**, *22*. https://doi.org/10.1016/j.redox.2019.101135.

(39) Padayachee, E. R.; Zetterberg, H.; Portelius, E.; Borén, J.; Molinuevo, J. L.; Andreasen, N.; Cukalevski, R.; Linse, S.; Blennow, K.; Andreasson, U. Cerebrospinal Fluid-Induced Retardation of Amyloid β Aggregation Correlates with Alzheimer's Disease and the APOE E4 Allele. *Brain Res* **2016**, *1651*, 11–16. https://doi.org/10.1016/j.brainres.2016.09.022.

(40) Bellomo, G.; Bologna, S.; Gonnelli, L.; Ravera, E.; Fragai, M.; Lelli, M.; Luchinat, C. Aggregation Kinetics of the Aβ1–40 Peptide Monitored by NMR. *Chem. Commun.* **2018**. https://doi.org/10.1039/C8CC01710G.

(41) Ahmed, R.; Melacini, G. A Solution NMR Toolset to Probe the Molecular Mechanisms of Amyloid Inhibitors. *Chem. Commun.* **2018**, *54* (37), 4644–4652. https://doi.org/10.1039/C8CC01380B.

(42) Molodenskiy, D.; Shirshin, E.; Tikhonova, T.; Gruzinov, A.; Peters, G.; Spinozzi, F. Thermally Induced Conformational Changes and Protein–Protein Interactions of Bovine Serum Albumin in Aqueous Solution under Different PH and Ionic Strengths as Revealed by SAXS Measurements. *Physical Chemistry Chemical Physics* **2017**, *19* (26), 17143–17155. https://doi.org/10.1039/C6CP08809K.

(43) Pisani, V.; Stefani, A.; Pierantozzi, M.; Natoli, S.; Stanzione, P.; Franciotta, D.; Pisani, A. Increased Blood-Cerebrospinal Fluid Transfer of Albumin in Advanced Parkinson's Disease. *J Neuroinflammation* **2012**, *9*, 188. https://doi.org/10.1186/1742-2094-9-188.

Table of Contents Image

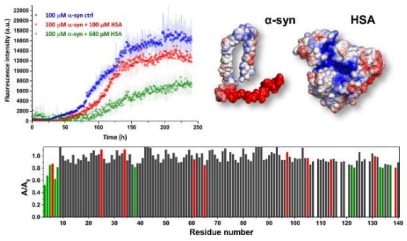

Supplementary Information

Dissecting the interactions between human serum albumin and α-synuclein: new insights on the factors influencing α-synuclein aggregation in biological fluids

Giovanni Bellomo,[a] *Sara Bologna,[a] Linda Cerofolini,[a] Silvia Paciotti,[c] Leonardo Gatticchi,[c] Enrico Ravera,[a,b] Lucilla Parnetti,[d*] Marco Fragai[a,b*] and Claudio Luchinat[a,b*]*

[a]*Magnetic Resonance Center (CERM), University of Florence, Via L. Sacconi 6, 50019 Sesto Fiorentino, Italy.*

[b]*Department of Chemistry "Ugo Schiff", University of Florence, Via della Lastruccia 3, 50019 Sesto Fiorentino, Italy.*

[c]*University of Perugia, Department of Experimental Medicine, Piazzale Gambuli 1, 06132 Perugia, Italy.*

[d]*Clinica Neurologica, Università degli Studi di Perugia, Piazzale Gambuli 1, 06132 Perugia, Italy.*

**E-mail: lucilla.parnetti@unipg.it. Phone: +39 0755783545.*

**E-mail: fragai@cerm.unifi.it. Phone: +39 055 4574261.*

**E-mail: claudioluchinat@cerm.unifi.it. Phone: +39 055 4574296.*

Contents

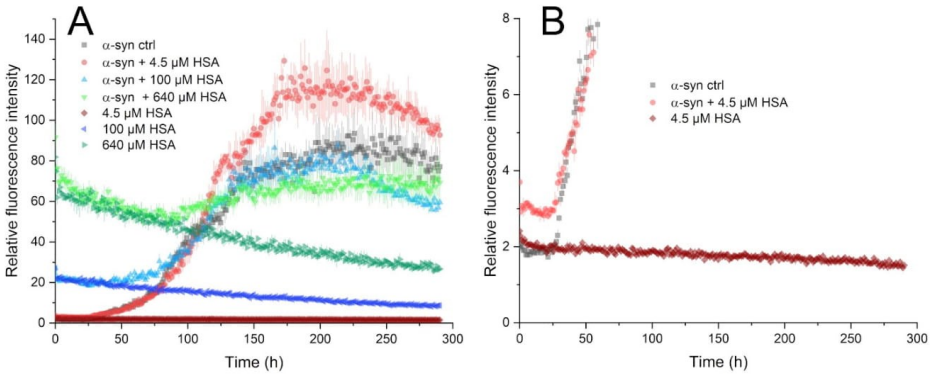

Fig. S1 *A) Monomeric α-syn 100 μM was left aggregating in the presence of ThT 10 μM and varying quantities of HSA. Wells containing only HSA and ThT were also prepared to measure the baseline fluorescence produced by ThT bound to HSA. The experiments were performed in triplicate in a 96-wells plate in PBS (NaCl 137 mM) pH 7.4, T = 310 K. 6x 1mm diameter glass beads were added in each well. The plate was subjected to cycles of shaking (1 min. shaking 500 rpm, 29 min. rest) inside a BMG Labtech ClarioStar fluorimeter. In this experiment in PBS we observed a progressive decay of fluorescence in the samples containing 100 μM and 640 μM HSA. The average fluorescence among replicates of samples with and without α-syn is shown in the image normalized on the average fluorescence value of the wells containing 10 μM of unbound ThT in PBS (195 a.u ± 8 a.u. constant for the whole duration of the experiment) to better appreciate the fluorescence enhancement. B) Zoom on the low fluorescence intensity to better visualize the behaviour of the 4.5 μM HSA samples.*

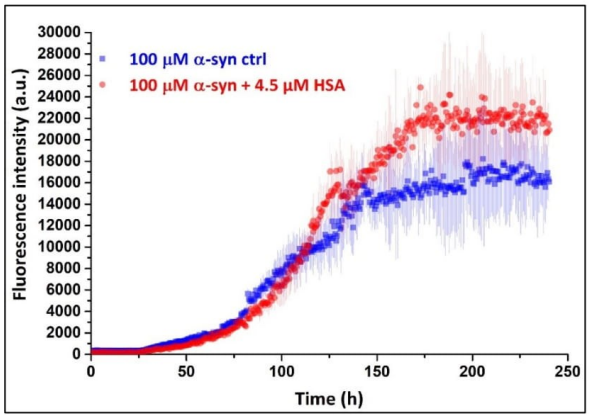

Fig. S2 *Monomeric α-syn 100 μM was left aggregating in the presence of ThT 10 μM and HSA 4.5 μM. The experiments were performed in triplicate in a 96-wells plate in PBS (NaCl 137 mM) pH 7.4, T = 310 K. 6x 1mm diameter glass beads were added to the samples. The plate was subjected to cycles of shaking (1 min. shaking 500 rpm, 29 min. rest) inside a BMG Labtech ClarioStar fluorimeter.*

The measured t_{lag}, t_0 and A_1-A_2 parameters are shown in Table S1. The values in this table were measured on not averaged and not normalized curves with the methods described in the main text, in particular the t_0 and A_1-A_2 parameters were measured by fitting the data with a sigmoidal function (Eq. 1 in the main text) and the t_{lag} values by applying a threshold on the experimental intensities. Apart from the increase in t_0 and t_{lag} values, also the levels of fluorescence, quantified by the A_1-A_2 parameter, appear lower in samples containing HSA 640 μM with respect to samples containing only α-syn (Fig. S3 and Table S1). Although ThT fluorescence is a good probe for fibril formation, caution should be use in interpreting this result, since HSA competes with α-syn fibrils in binding ThT.

Experiment	HSA (μM)	t_0 (h)	t_{lag} (h)	A_2-A_1 (a.u.)
KPi, pH 6.0 α-syn 50 μM	0	86 ± 6	27 ± 1	$(4.2 \pm 1.4)\cdot10^3$
	50	135 ± 9	29 ± 2	$(5 \pm 1)\cdot10^3$
	640	167 ± 4	119 ± 4	$(7.2 \pm 0.7)\cdot10^2$
PBS, pH 7.4 α-syn 100 μM	0	105 ± 2	28.3 ± 0.4	$(1.7 \pm 0.2)\cdot10^4$
	4.5	116 ± 3	30 ± 1	$(2.2 \pm 0.2)\cdot10^4$
	100	114 ± 2	61 ± 1	$(1.33 \pm 0.07)\cdot10^4$
	640	141 ± 6	130 ± 10	$(8 \pm 2)\cdot10^3$

Table S1 *t_0, t_{lag} and A_2-A_1 parameters for the experiments performed with 50 μM α-syn in 20 mM KPi, 50 mM NaCl, pH 6.0, T = 310 K and 100 μM α-syn in PBS, pH 7.4, T = 310 K. The values present in the table result from the average on three replicates while their uncertainty corresponds to the standard deviation of the average value.*

NMR experiments

All the NMR spectra were acquired at 283 K with a Bruker Avance III HD NMR spectrometer operating at 950 MHz ^{1}H Larmor frequency, equipped with a cryogenically cooled probe. The spectra were processed with the Bruker TOPSPIN 4.0 software packages and analysed by the program Computer Aided Resonance Assignment [8]. During the NMR titration of the protein with HSA, 3 aliquots of a concentrated 8 mM solution of HSA (same buffer conditions of the final samples) were added to the buffered solution containing ^{15}N isotopically enriched α-syn at the concentration of 100 μM. The tested buffered solutions were: [20 mM KPi, pH 6.0 with 50, 100 and 150 mM NaCl] and PBS (pH 7.4). For the NMR experiments, standard 3 mm glass tubes were used with a final sample volume of of 200 μL. The added volumes of the HSA solution were 2.5, 16 and 22.5 μL for the 100, 640 and 900 μM samples, respectively, in all the buffer used. While testing the electrostatic nature of the interaction between α-syn and HSA, also 2 μL and 4 μL of a solution of 20 mM KPi, pH 6.0 with 5 M NaCl were added in the NMR tube containing α-syn 100 μM and HSA 900 μM, to reach the final concentration of 100 and 150 mM NaCl, respectively. The data relative to the 100 mM NaCl sample are shown in Fig. S5B. At this ionic strength, the intensity reduction observed at the C-terminus of α-syn was less evident compared to the 50 mM NaCl sample but not completely disappeared as in the 150 mM sample.

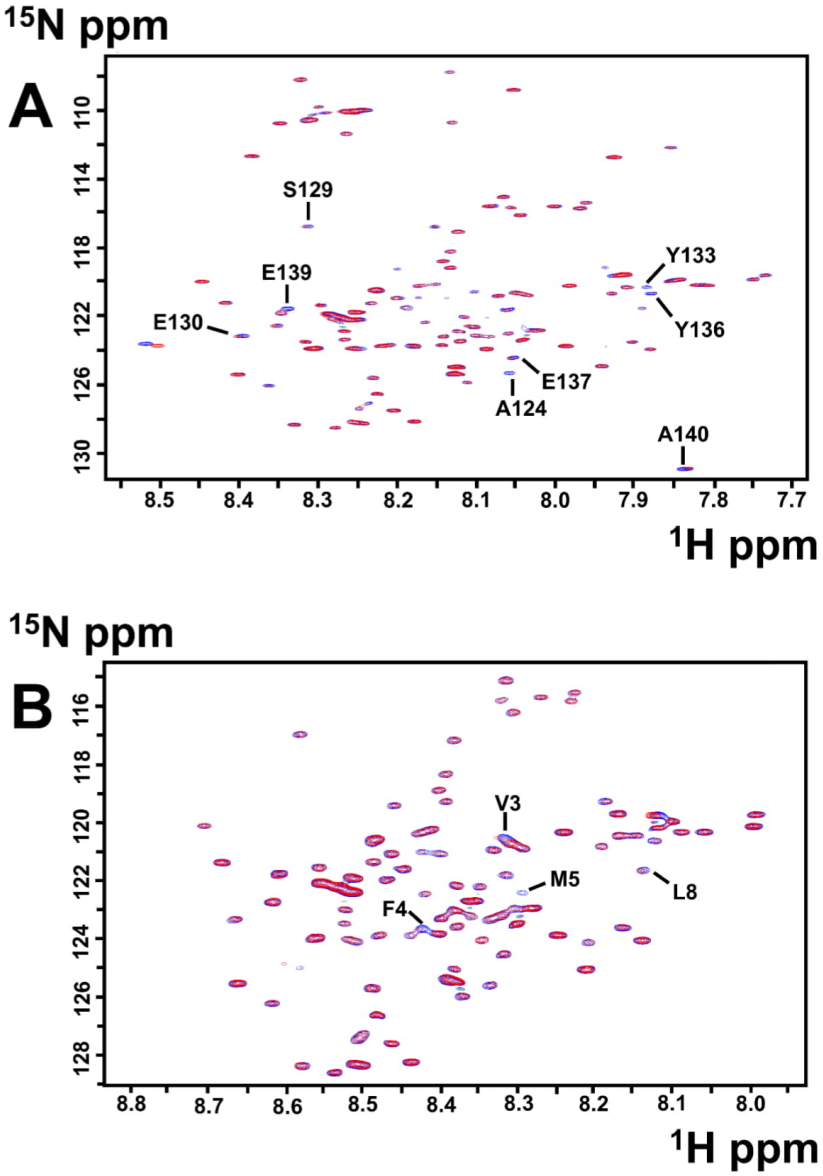

Fig. S3 *Portion of 2D ^{15}N ^{1}H HSQC experiments performed at T = 283 K using a Bruker 950 MHz NMR spectrometer in different buffer conditions. The spectra coloured in red correspond to samples containing α-syn 100 μM and HSA 900 μM while the ones in blue correspond to the reference samples containing α-syn 100 μM alone. A) Experiment performed in KPi 20 mM, NaCl 50 mM pH 6.0 with α-syn 100 μM and HSA 900 μM. C) Experiment performed PBS (NaCl 137 mM) pH 7.4 with α-syn 100 μM and HSA 900 μM. The residues which showed an evident decrease in intensity are displayed on the image.*

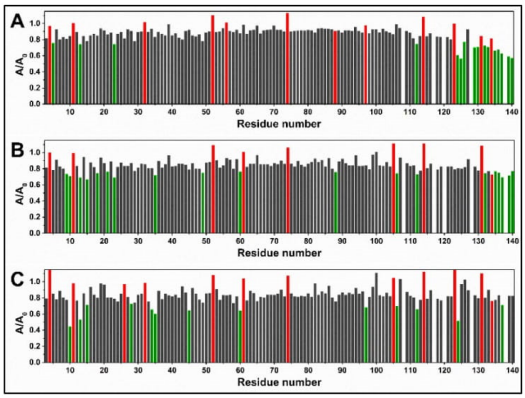

Fig. S4 *Intensity ratios of peaks coming from 2D ^{15}N ^{1}H HSQC experiments performed at T = 283 K using a Bruker 950 MHz NMR spectrometer at different NaCl concentrations. The intensity values were computed with CARA (Computer Aided Resonance Assignment). The ratios highlighted in green are the ones which are smaller by one or more standard deviation with respect to the average value. The ratios highlighted in red correspond to peaks in overlap, their values was not used to calculate averages and standard deviations. A) Experiment performed in KPi 20 mM, NaCl 50 mM pH 6.0 with α-syn 100 μM and HSA 900 μM. B) Experiment performed in KPi 20 mM, NaCl 100 mM pH 6.0 with α-syn 100 μM and HSA 900 μM. C) Experiment performed in KPi 20 mM, NaCl 150 mM pH 6.0 with α-syn 100 μM and HSA 900 μM.*

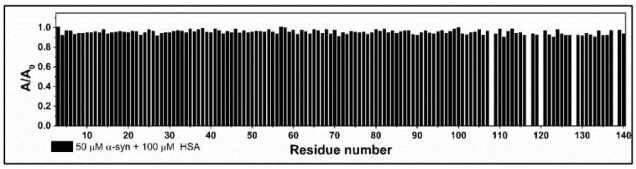

Fig. S5 *Intensity ratios of peaks coming from 2D ^{15}N ^{1}H HSQC experiments performed at T = 283 K using a Bruker 950 MHz NMR spectrometer. The intensity values were computed with CARA (Computer Aided Resonance Assignment). The experiment was performed in KPi 20 mM, NaCl 50 mM pH 6.0 with α-syn 100 μM and HSA 100 μM. No relevant drops in intensity were observed with respect to the reference spectrum.*

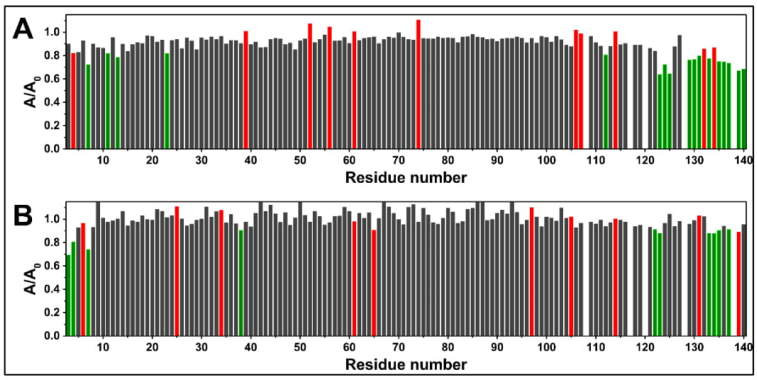

Fig. S6 *Intensity ratios of peaks coming from 2D ^{15}N ^{1}H HSQC experiments performed at T = 283 K using a Bruker 950 MHz NMR spectrometer in different buffer conditions. The intensity values were computed with CARA (Computer Aided Resonance Assignment). The ratios highlighted in green are the ones which are smaller by one or more standard deviation with respect to the average value. The ratios highlighted in red*

correspond to peaks in overlap, their values was not used to calculate averages and standard deviations. A) Experiment performed in KPi 20 mM, NaCl 50 mM pH 6.0 with α-syn 100 μM and HSA 640 μM. B) Experiment performed PBS (NaCl 137 mM) pH 7.4 with α-syn 100 μM and HSA 640 μM.

Test with fatty-acid free HSA

To test if the lipids naturally included in HSA may have a role in its interaction with α-syn, we repeated the NMR interaction experiment with fatty acid free HSA in KPi 20 mM, NaCl 50 mM pH 6.0 with α-syn 100 μM. The measured intensity ratios (Fig. S8) for fatty acid free HSA do not show significative differences with respect to the ratios obtained with native HSA. The rooted mean squared ratio difference is about 0.06 and mainly due to an almost negligible offset in intensity ratios which may be provoked by very small differences in the experimental setup (slightly different shims with respect to the reference spectrum, concentration differences, etc.).

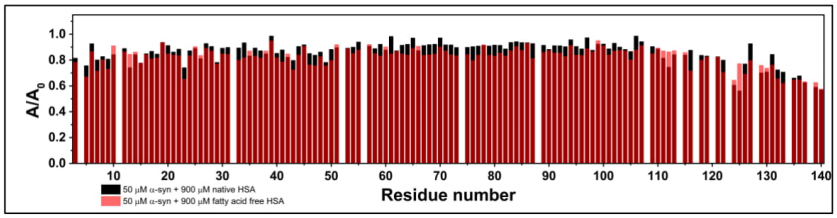

Fig. S7 *Intensity ratios of peaks coming from 2D ^{15}N ^{1}H HSQC experiments performed at T = 283 K using a Bruker 950 MHz NMR spectrometer. The intensity values were computed with CARA (Computer Aided Resonance Assignment). The ratios corresponding to peaks in overlap, were excluded from the graph. The experiment was performed in KPi 20 mM, NaCl 50 mM pH 6.0 with α-syn 100 μM and native (black) and fatty-acid free (red) HSA 900 μM.*

References

[1] V.E. Shevchik, G. Condemine, J. Robert-Baudouy, Characterization of DsbC, a periplasmic protein of Erwinia chrysanthemi and Escherichia coli with disulfide isomerase activity., EMBO J. 13 (1994) 2007–2012. https://www.ncbi.nlm.nih.gov/pmc/articles/PMC395043/ (accessed May 16, 2018).

[2] C. Huang, G. Ren, H. Zhou, C. Wang, A new method for purification of recombinant human alpha-synuclein in Escherichia coli, Protein Expr. Purif. 42 (2005) 173–177. doi:10.1016/j.pep.2005.02.014.

[3] S.L. Shammas, T.P.J. Knowles, A.J. Baldwin, C.E. MacPhee, M.E. Welland, C.M. Dobson, G.L. Devlin, Perturbation of the Stability of Amyloid Fibrils through Alteration of Electrostatic Interactions, Biophys. J. 100 (2011) 2783–2791. doi:10.1016/j.bpj.2011.04.039.

[4] J.A. Cohlberg, J. Li, V.N. Uversky, A.L. Fink, Heparin and other glycosaminoglycans stimulate the formation of amyloid fibrils from alpha-synuclein in vitro, Biochemistry. 41 (2002) 1502–1511.

[5] L. Giehm, D.E. Otzen, Strategies to increase the reproducibility of protein fibrillization in plate reader assays, Anal. Biochem. 400 (2010) 270–281. doi:10.1016/j.ab.2010.02.001.

[6] M. Shahnawaz, T. Tokuda, M. Waragai, N. Mendez, R. Ishii, C. Trenkwalder, B. Mollenhauer, C. Soto, Development of a Biochemical Diagnosis of Parkinson Disease by Detection of α-Synuclein Misfolded Aggregates in Cerebrospinal Fluid, JAMA Neurol. 74 (2017) 163–172. doi:10.1001/jamaneurol.2016.4547.

[7] N.R. Rovnyagina, N.N. Sluchanko, T.N. Tikhonova, V.V. Fadeev, A.Y. Litskevich, A.A. Maskevich, E.A. Shirshin, Binding of thioflavin T by albumins: An underestimated role of protein oligomeric

heterogeneity, Int. J. Biol. Macromol. 108 (2018) 284–290. doi:10.1016/j.ijbiomac.2017.12.002.
[8] R.L.J. Keller, Optimizing the process of nuclear magnetic resonance spectrum analysis and computer aided resonance assignment, Doctoral Thesis, ETH Zurich, 2005. doi:10.3929/ethz-a-005068942.

3.3 Human plasma HDL prevents the formation of α-synuclein oligomers and fibrils (manuscript in preparation)

Introduction

Lipoproteins are complex particles composed of multiple proteins that transport lipids around the body within the aqueous environment outside the cells. High-density lipoproteins (HDL) are the smallest particles among the five major groups of lipoproteins (10–22 nm),[93–95] they are also the most dense because the high protein content with respect to the lipid part. The most characterized and most abundant protein constituents of HDL are apolipoprotein-A1 (apoA1) and apolipoprotein-E (apoE).[96] The Central Nervous System apoE is completely brain-specific, and there is no exchange between plasma-derived apoE and brain apoE because of the boundary of the Brain-Blood Barrier (BBB).[97] Also due to the different composition in terms of apolipoproteins, the CSF HDL are bigger in size than plasma HDL and smaller than Low-Density Lipoproteins (LDL), their density is between LDL and HDL.[95,98,99] While apoE is found to be the main constituent of HDL particles in CSF (see Table 3.3.1), apoA1 is the main constituent of HDL in plasma.[94,100] However, apoA1 also contributes for lipid transportation and delivery in the brain and the apoA1 levels of CSF and plasma have been shown to be correlated.[101] Since there is no evidence of apoA1 synthesis in the brain, apoA1 or apoA1 rich HDL, in contrast to apoE, is thought to be able to cross the BBB.[96] HDL are reported have an impact in many neurodegenerative disorders. apoE plays a crucial role in AD, mild cognitive impairment[102] and Creutzfeldt-Jakob disease (CJD).[103,104] In particular, the APOE ε4 allele is strongly associated with the sporadic late-onset AD.[105–107] Conversely, no association was found between apoE and PD,[108] while lower levels of apoA1 were rather measured in the plasma of PD patients with respect to controls.[109–111] These findings were confirmed again in late 2015, when plasma apoA1 and high-density lipoprotein at baseline were measured in 254 research volunteers (154 patients with PD and 100 normal controls) enrolled in the Parkinson's Progression Markers Initiative (PPMI)[112] study (without any ongoing levodopa treatment). In this latter study, lower levels of apoA1 were found to be associated with the age of PD onset and severity of motor symptoms (p-values < 0.05),[113] suggesting that apoA1 or apoA1-rich lipoproteins may be both a protective factor and a candidate biomarker for PD. The mechanism underlying the protective role of HDL in neurodegenerative diseases remains unknown but, for AD, it seems to be intimately linked to increased risk of brain Aβ aggregation in ε4 carriers.[114]

Recently, CSF HDL was shown to retard Aβ42 aggregation in an apoE ε4-dependent manner.[30] In this study, the addition of CSF fractions containing HDL produced an extended lag-phase of the ThT fluorescence profiles, which implies an interference with the primary nucleation of the aggregates. Although the protective role of HDL was extensively investigated for AD, few previous studies have focused on the role of HDL in the context of PD and α-syn aggregation.[92] In this work we investigate the effect of plasma HDL, rich in apoA1 apolipoproteins, on α-syn aggregation and if the inhibitory effect of human CSF on α-syn aggregation, observed in a previous study (paragraph 2.3), may be produced by HDL. Our hypothesis is that these compounds naturally prevent the formation of fibrils and oligomers by interacting with α-syn aggregates and not directly with α-syn monomers.

Fluid matrix	apo E (mg/dl)	apo A1 (mg/dl)
CSF	0.3 ± 0.2[115]	0.3 ± 0.2[115]
	1.0 ± 0.1[116]	0.33 ± 0.05[116]
	0.4 ± 0.2[117]	0.4 ± 0.2[117]
	0.5 ± 0.3[118]	0.3 ± 0.2[118]
Plasma	7 ± 5[115]	140 ± 50[115]
	8 ± 1[118]	270 ± 20[118]

Table 3.3.1: Reported values of Apolipoprotein E and A1 levels in CSF and plasma of healthy individuals.

Materials and Methods

α-synuclein expression and purification

Escherichia Coli BL21(DE3)Gold were transformed with pT7-7 vector cloned with the gene encoding α-synuclein. The overnight preculture of transformed cells was diluted 100-fold in LB medium and induced at an OD_{600} value of 0.6- 0.8 with 1 mM Isopropyl-β-D-thiogalactoside and, after 5 hours incubation at 37 °C, the cells were harvested at 4000 rpm (JA-10, Beckman Coulter). The extraction was carried out through osmotic shock using 100 ml of buffer TRIS 30 mM, EDTA 2 mM and sucrose 40%, at pH 7.2 according to Shevchik et al.[62] and Huang et al.[63]. The suspension was then ultracentrifuged at 20000 rpm (Type 70 Ti rotor, Beckman Coulter) for 25 min and pellet was collected and resuspended with 90 ml precooled ultrapure water additioned with 38µl of $MgCl_2$ 1 M and then ultracentrifuged a second time. Surnatants derived from these two centrifugation steps, were joined and dialyzed against 4 L of buffer 20 mM TRIS/HCl at pH 8.0. The protein then was loaded in the FPLC system and an anion exchange chromatography was carried out with 0-50% linear gradient NaCl 1 M (GE Healthcare HiPrep™ Q HP 16/10 Column). The collected

fractions were lyophilized and resuspended in 10 mM TRIS/HCl, 1 mM EDTA and urea 8 M at pH 8.0 for the chemical denaturation. To eliminate all the protein formed aggregates, two size-exclusion chromatographies (HiLoad™ 16/600 Superdex™ 75 pg Column) were performed with 20 mM phosphate and 0.5 mM EDTA at pH 8.0 as elution buffer. Purified α-synuclein (α-syn) was dialyzed against Milli-Q water and lyophilized in batches for long-term storage. Roche cOmplete™ protease inhibitor cocktail was added only during the extraction step in the quantity suggested by the producer.

α-syn aggregation experiments

The lyophilized aliquots α-syn were resuspended in NaOH 3.5 mM (pH 11.54) right before the experiments to avoid the instantaneous formation of aggregates. At high pH, the negatively charged monomers (the isoelectric point of α-syn is 4.67) experience an electrostatic repulsion that impedes the aggregation and favors the dissociation of small aggregates.[64,65] The solution of α-syn and NaOH was brought to pH 7.4 and protein concentration of 100 μM by adding concentrated PBS buffer (e.g. 1 mL of NaOH solution with 1 mL of 2x PBS solution). Thioflavin-T was also added in a final concentration of 10 μM. To avoid the possible growth of bacteria during the experiment, a 0.08% of NaN_3 was present in the reaction buffer. We added different volumes of HDL derived from human plasma (LP3-5MG from SIGMA-ALDRICH, HDL concentration 11.64 mg/mL). Subsequently, each sample was split in 3 replicates of 200 μl each that were put in a *TECAN (REF: 30122306)* clear-bottom 96-well plate. We added 6 acid washed glass beads with a diameter of 1 mm in each well to enhance the aggregation speed and increase homogeneity among replicates.[66] The plates were always sealed with a sealing tape to minimize evaporation during the experiments. Successively, plates were inserted in a BMG LABTECH ClarioStar fluorimeter and subjected to the incubation/shaking protocol of Shahnawaz et al.[52] (T = 310 K, 29 min. incubation, 1 min. shaking at 500 rpm). Once every 30 minutes, the fluorescence was read from the bottom using an excitation and emission wavelength of 450 nm and 480 nm, respectively.

Dot blot assays

The dot blot assay was performed using A11 anti-oligomer antibodies (ThermoFisher Scientific) and OC anti-fibril antibodies (Sigma-Aldrich) on the samples used for the fluorimetric assay, by collecting together the replicates for each concentration of HDL and HSA. Volumes of 2 μl of each sample where dropped on a nitrocellulose membrane, previously soaked with TBS-T (0.1%) and were let dry for 60 minutes. The substrate was then fixed to the membrane by soaking it in PBS with 0.4% PFA for 30 minutes. The blocking

was subsequently performed by soaking the membrane in a solution of dry milk (2%) and TBS-T (0.1%) for 60 minutes at room temperature. The blocking buffer was then poured off and the membrane was incubated with A11/OC antibodies (1:1000) in a solution of dry milk (5%) and TBS-T (0.1%) at 4°C for 60 minutes. The membrane was then washed and incubated with HRP anti-rabbit secondary antibodies (1:5000) and a solution of dry milk (5%) and TBS-T (0.1%) for 30 minutes. The data were subsequently processed and analyzed using ImageJ.

NMR experiments

All the NMR spectra were acquired at 283 K with a Bruker Avance III HD NMR spectrometer operating at 950 MHz ^{1}H Larmor frequency, equipped with a cryogenically cooled probe. The spectra were processed with the Bruker TOPSPIN 4.0 software packages and analyzed by the program Computer Aided Resonance Assignment (ETH Zurich; Keller, 2004). During the NMR titration of α-syn with HDL, 1 aliquot (5 µl) of a concentrated 11.64 mg/mL solution of human HDL (LP3-5MG from SIGMA-ALDRICH) were added to the buffered solution containing ^{15}N isotopically enriched α-syn at the concentration of 100 µM in PBS (pH 7.4, 137 mM NaCl). For the NMR experiments, standard 3 mm glass tubes were used with a final sample volume of of 200 µl. We acquired a 1D ^{1}H experiment and 2D ^{1}H ^{15}N HSQC experiment[119] for both the sample containing HDL and the reference one.

Results and Discussion

To test the effects of HDL on α-syn aggregation we performed ThT aggregation experiments. In these kind of experiments, the ThT fluorophore reports the formation of fibril-like aggregates due to its affinity to the beta-sheet motifs typical of amyloid aggregates.[120] We applied the PMCA shaking/incubation protocol of Shahnawaz, Soto and coworkers[52] to speed-up the aggregation and added 6 glass beads (with a diameter of 1 mm) per well to further promote the aggregation process and increase the homogeneity among replicates (further details in the Materials and Methods section). The experiments were performed in well plates in triplicate (final volume of 200 µl per well), the control samples with α-syn alone consisted in 100 µM monomeric α-syn, 10 µM ThT and 0.08% of NaN_3 in PBS buffer. The samples containing HDL had the same composition except for the quantity of HDL that was of 12 mg/dl and 57 mg/dl respectively. We also prepared control samples containing 12 mg/dl and 57 mg/dl HDL without α-syn to subtract any possible background fluorescence. Although the background fluorescence was almost negligible, we subtracted the fluorescence data relative to samples containing only HDL (averaged on replicates) from the data relative to samples containing both α-syn and HDL (averaged on

replicates). By looking at the ThT fluorescence profiles of Fig. 3.2.1, it is evident that the addition of increasing quantities of HDL to the solution had an impact on α-syn aggregation.

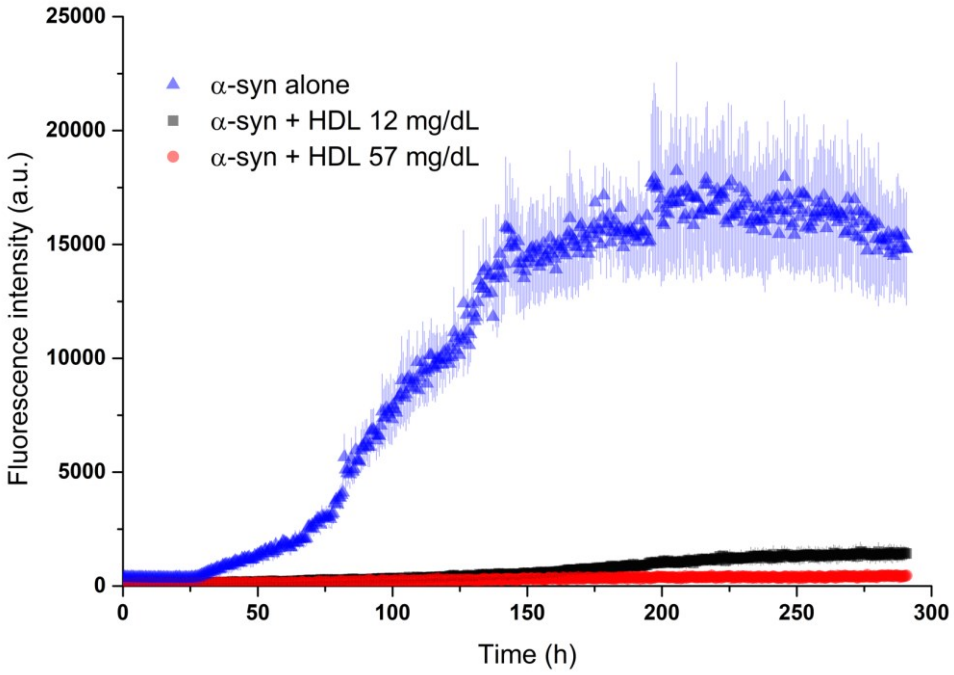

Fig. 3.3.1 Monomeric α-syn 100 μM was left aggregating in the presence of ThT 10 μM and increasing quantities of HDL. The experiments were performed in triplicate in a 96-wells plate in PBS pH 7.4, T = 310 K. Glass beads (6x 1mm diameter) were added to the samples. The plate was subjected to cycles of shaking (1 min. shaking 500 rpm, 29 min. rest) inside a BMG Labtech ClarioStar fluorimeter. The data shown are the averages of three replicates with background removed. The error bars were calculated as the standard deviation of the mean value calculated on the three replicates.

The kinetic profiles, which were used to produce the averaged curves depicted in Fig. 3.3.1, were fitted with Boltzmann's sigmoidal functions (Eq. 3.3.1), using *OriginPro 9*, in order to obtain an estimate of the aggregation time. In the non-linear curve fitting procedure used, the parameters A_1, A_2, t_0 and dt of Eq. 3.3.1 were let free.

$$y(t) = A_2 + \frac{A_1 - A_2}{1 + \exp\left(\frac{t - t_0}{dt}\right)} \tag{3.3.1}$$

The parameter t_0 corresponds to the inflection point of the sigmoidal curves used to fit the data and can be used to quantify the time necessary to produce a consistent quantity of fibrillary aggregates. Another parameter which can be useful to characterize the speed of the aggregation is the time at which the fluorescence starts to deviate significantly from its initial value (t_{lag}). This parameter quantifies the time at which fibrils start to form. We defined it, in the same way of Paragraph 3.2, as the time at which the fluorescence (F) of a well

becomes higher than the average fluorescence (on the same well) of the first 5 h ($\overline{F(t)}_{t<5\ h}$) plus 2 standard deviations (2σ) for 5 consecutive measurements:

$$F(t_{lag} + i\Delta t) \geq \overline{F(t)}_{t<5\ h} + 2\sigma\big(F(t)\big)_{t<5\ h};\ \forall\ i \in (0, 1, 2, 3, 4)$$

Where Δt is the time between two consecutive measurements. The measured t_0 and t_{lag} values, together with the A2-A1 values of the sigmoidal fitting, which report for the amplitude of the sigmoids, are reported in Table 3.3.2. In the Table, the values relative to the experiments performed in PBS with α-syn and HSA (Paragraph 3.1), Which were measured during the same acquisition, on the same plate and with the same batch of α-syn, are also reported for comparison.

Sample	t_{lag} (h)	t_0 (h)	A2 - A1 (a.u.)
α-syn alone	28.3 ± 0.5	105 ± 2	$(1.7 \pm 0.2) \cdot 10^4$
α-syn + 12 mg/dL HDL	44 ± 4	176 ± 6	$(1.4 \pm 0.3) \cdot 10^3$
α-syn + 58 mg/dL HDL	82 ± 7	119 ± 9	$(3.7 \pm 0.9) \cdot 10^2$
α-syn + 4.5 μM HSA	30 ± 1	116 ± 3	$(2.2 \pm 0.2) \cdot 10^4$
α-syn + 100 μM HSA	61 ± 1	114 ± 2	$(1.33 \pm 0.07) \cdot 10^4$
α-syn + 640 μM HSA	130 ± 10	141 ± 6	$(8 \pm 2) \cdot 10^3$

Table 3.3.2: Measured t_{lag}, t_0 and A1-A2 values for samples containing α-syn and different quantities of HDL and HSA.

While some differences on the t_0 parameters may be observed for samples containing HDL with respect for the samples containing α-syn alone, minor differences are present for the t_{lag} values. The most pronounced effect was rather the change of the maximum fluorescence value, quantified in Table 3.3.2 by the A2-A1 parameter. The measured amplitudes are also depicted in the column plot present in Fig. 3.3.2, which can better show the difference in the A2-A1 values of the sample containing α-syn and HDL from the ones containing α-syn and HSA or α-syn alone.

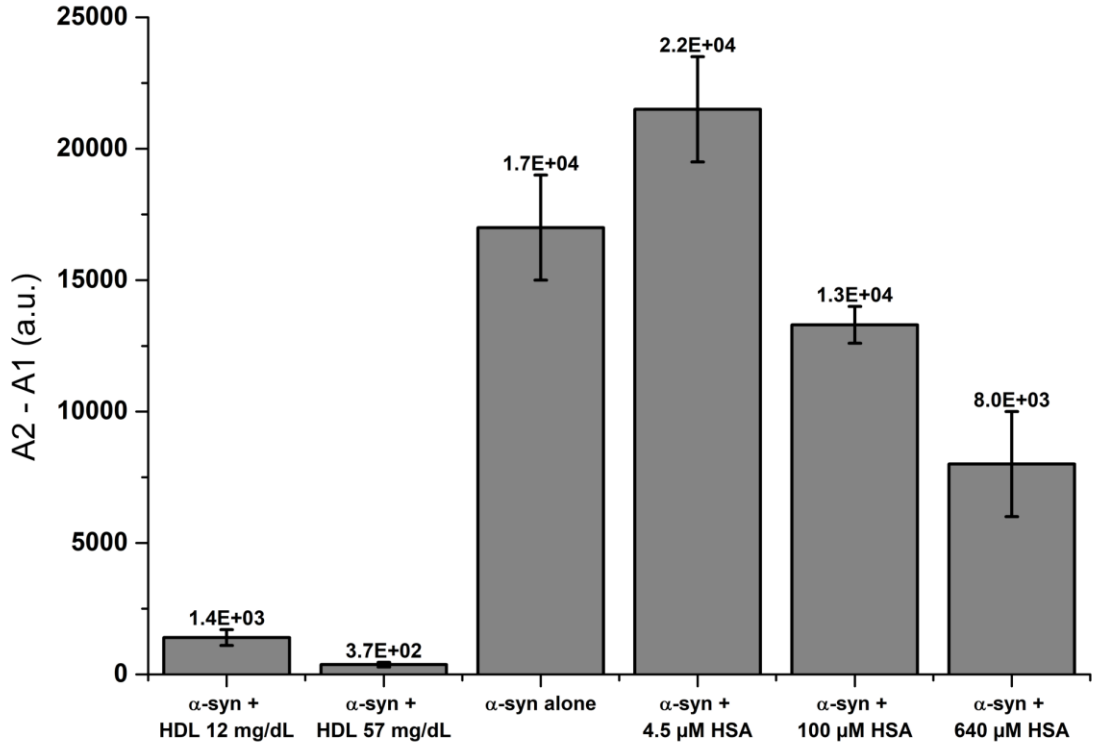

Fig. 3.3.2 Measured A1-A2 values coming from the sigmoidal fitting of the ThT profiles relative to samples containing α-syn and different quantities of HDL and HSA.

To better clarify if the much lower ThT intensity was produced by a lower quantity of aggregates we performed a dot blot on the samples containing HDL and HSA with OC and A11 antibodies.[107]
The OC and A11 antibodies bind to different oligomeric conformations: the OC antibody binds fibrils and fibrillary oligomers while the A11 is sensitive to more amorphous oligomeric aggregates. Particularly, A11 oligomers showed to be more toxic than the OC oligomers[122] and recently showed the ability to impair the proteasome function.[17] As can be seen from Fig. 3.3.3 and Fig. 3.3.4, control samples without α-syn did not bind to any of the two antibodies, while the samples containing α-syn and HDL produced some OC and A11 oligomers but in a much lower quantity with respect to the samples containing α-syn and HSA. This result is in accord with the ThT measurements which reported a lower quantity of fibrils for samples containing α-syn and HDL.

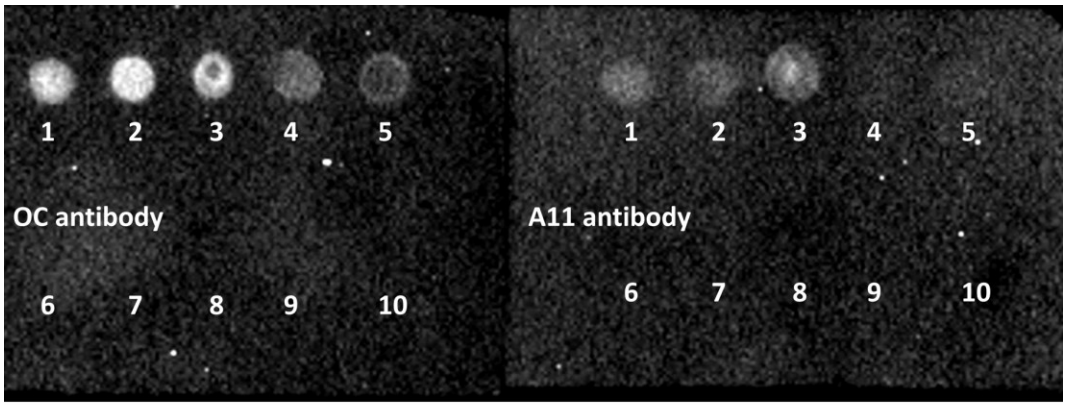

1 α-syn + 4.5 μM HSA **2** α-syn + 100 μM HSA **3** α-syn + 640 μM HSA
4 α-syn + 2 μL HDL (0.114 mg/ml) **5** α-syn + 10 μL HDL (0.57 mg/ml) **6** 4.5 μM HSA
7 100 μM HSA **8** 640 μM HSA **9** 2 μL HDL (12 mg/ml)
10 10 μL HDL (57 mg/dL)

Fig. 3.3.3 The dot blot assay was performed using A11 anti-oligomer antibodies and OC anti-fibril antibodies on the samples used for the fluorimetric assay which contained 100 μM α-syn and different amounts of HSA and HDL. The dot images were processed and analyzed with ImageJ. Control samples n° 6, 7, 8, 9 and 10 did not react with any of the two antibodies used.

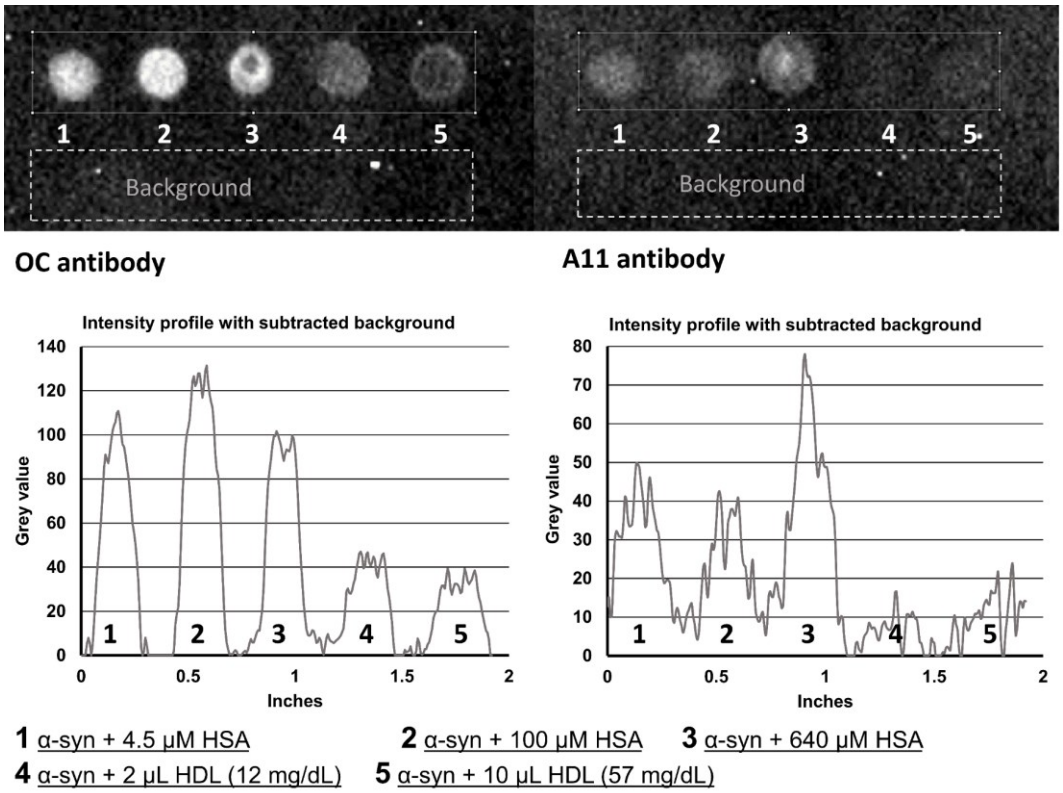

1 α-syn + 4.5 μM HSA **2** α-syn + 100 μM HSA **3** α-syn + 640 μM HSA
4 α-syn + 2 μL HDL (12 mg/dL) **5** α-syn + 10 μL HDL (57 mg/dL)

Fig. 3.3.4 The dot blot assay was performed using A11 anti-oligomer antibodies and OC anti-fibril antibodies on the samples used for the fluorimetric assay which contained 100 μM α-syn and different amounts of HSA and HDL. The dot images were processed (window/levels adjustments) and analyzed with ImageJ.

In 2017 Emamzadeh and Allsop[92] showed that α-syn, apoA1, apoJ and apoE could be detected by immunoprecipitation in plasma both with anti-α-syn and anti-apolipoprotein antibodies, suggesting a possible direct or indirect interaction between α-syn and plasma HDL. To test if the inhibitory effect of plasma HDL on α-syn aggregation could be produced by the direct interaction with α-syn monomer, we performed a 2D ^{15}N ^{1}H NMR HSQC experiment with ^{15}N isotopically enriched α-syn. After having acquired a reference spectrum with α-syn 100 μM in PBS pH 7.4 in a 3 mm diameter NMR tube (final sample volume 200 μl), we added 5 μl of human plasma HDL in the NMR tube (HDL final concentration 28.4 mg/dL, final sample volume 205 μl). No relevant shifts in the 2D ^{15}N ^{1}H NMR HSQC were observed so we evaluated the intensity ratios by dividing the amplitude of the crosspeaks relative to the experiment with HDL by the ones relative to the reference spectrum. The ratios calculated in this way (corrected for the dilution factor of α-syn) are shown in Fig. 3.3.5.

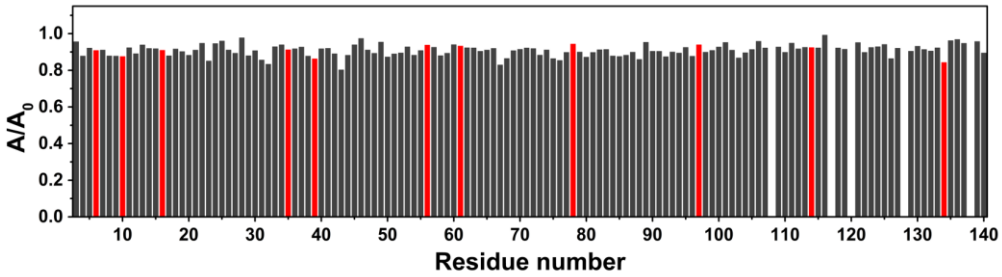

Fig. 3.3.5 Intensity decreases of the signals of 2D ^{15}N ^{1}H HSQC experiments acquired at 950 MHz on α-syn (100 μM) after the addition of 5 μl HDL (final concentration 28.5 mg/dL) at T = 283 K in PBS (NaCl 137 mM) pH 7.4. The intensity ratios corresponding to overlapping peaks are highlighted in red and should be not taken into account.

By considering the experimental uncertainties on the measure of the intensity of the crosspeaks, we can say, by looking at Fig. 3.3.5, that no relevant interactions were observed between the tested quantities of human plasma HDL particles and monomeric α-syn.

Conclusions

In our experiments human plasma HDL decreased significantly the quantity of fibrillary and oligomeric aggregates produced by α-syn. We did not observe any relevant interaction between monomeric α-syn and HDL from NMR experiments. These findings suggest that the interaction between HDL and α-syn may not involve the primary nucleation of the aggregates and we hypothesize that HDL may instead interact with α-syn oligomers

preventing them to grow and to convert into fibrillar amyloids. This observation is also in accord with the lag-time measurements, which are primarily influenced by primary nucleation effects[33] and showed lower t_{lag} values with respect to the experiments performed with HSA. ApoA1 is the main component of HDL in plasma but it is also necessary for cholesterol transportation in the central nervous system. The plasma level of apoA1 was found to be lower in PD patients than that in normal individuals, indicating a possible role for apoA1-deficency in the pathogenesis of PD.[109–111,113] We hypothesize that apoA1-containig HDL, may have a protective role against PD, impeding the transmission and the growth of α-syn aggregates from cell to cell. Since from other works it was also shown that HDL particles are able to bind α-syn,[102] and from our data it seems that monomeric α-syn is not able to bind plasma HDL, apoA1 rich HDL may also be responsible for the transportation of small α-syn aggregates out of the brain. The antiaggregatory effect of plasma HDL on α-syn probably contributes to the antiaggregatory effect observed for human CSF on α-syn aggregation[52] (Fig. 2.3.5). However, ApoA1 rich HDL is only one type of lipoproteins among the ones present CSF and we cannot exclude that VLDL, LDL or ApoE-rich HDL, may be involved in the antiaggregatory effect.

4 Automatic assignment of 3D NOESY ^{1}H-^{15}N HSQC for protein-ligand, protein-protein interaction studies. (manuscript in preparation)

4.1 Introduction

This last chapter of my PhD thesis involves the problematics of automatic assignment of ^{1}H-^{15}N HSQC (Heteronuclear Single Quantum Coherence spectroscopy)[119] which is a current crucial problem in the NMR and drug-discovery communities.[123] AD and PD, which are the two most common neurodegenerative disorders affecting humans, still lacks in therapeutic agents able to stop or decrease the protein accumulation and misfolding processes that lead to neurodegeneration. Many groups in the scientific community are investigating the role of small molecules in inhibiting α-syn[70,124] and Aβ[125–127] misfolding but nowadays some of them are considering also the therapeutic effect of proteins and antibodies.[128,129] Drug discovery and testing with NMR is usually conducted by performing ^{1}H-^{15}N HSQC experiments. ^{1}H-^{15}N HSQC is a powerful experiment to quickly test if there is an interaction between a ^{15}N labelled protein (e.g. an anti-Aβ antibody) and another ligand or an unlabeled protein/peptide (e.g. Aβ or α-syn). The amide protons are in fact very sensitive both to the variations of the chemical environment and the dynamics of complex formation, providing residue specific information (except for prolines). A limiting step of these kind of experiments is the assignment procedure, which is usually very time consuming and requires triple resonance experiments with expensive ^{13}C labelling, to obtain the backbone sequential assignment. Some programs, like FLYA[130] and MARS,[131] make use of ^{1}H-^{13}C HSQCs, ^{1}H-^{15}N HSQCs and 3D ^{13}C and ^{15}N NOESY experiments to perform automatic backbone assignment. For drug discovery purposes it will be very intriguing to perform faster experiments by using only ^{15}N labelled samples. A first trial of a program of this kind was made in 2004 by Langmead and Donald with the developing of NVR,[132] a MATLAB package for automatic assignment of HSQCs that makes use of protein X-ray structure, chemical shifts, Nuclear Overhauser Effects (NOEs), Residual Dipolar Couplings

(RDCs) and hydrogen/deuterium exchange rates to perform automatic backbone assignment using bipartite graph matching routines[133] and an expectation/minimization algorithm.

Our first attempt to obtain the automatic backbone assignment from only ^{15}N labelled samples was performed in 2017, the software was thought to use only RDCs and chemical shifts for the automatic assignment procedure. Although we obtained very good assignments for proteins with NMR refined structures[134] (more than 90% of the assignments were correct) the majority of other proteins with not refined (by NMR) X-ray structures had a too much high Q-factor to produce a reliable fitting of the alignment tensor. Therefore, we recycled most of the algorithms we already developed to build a new software that uses NOEs as the main source of information together with the X-ray structure and chemical shifts. The core algorithm that it is used in the current strategy is the so-called *Hungarian* method, which is a combinatorial optimization algorithm that exactly solves the assignment problem by the minimization of a global cost function in polynomial time.[135] In our case, we set the global cost function as the sum of the "distances" (see 4.3.2) between experimental and simulated peaks. The general strategy I followed for the development of this project consisted on simulating a 3D ^{1}H ^{15}N NOESY HSQC spectrum, by using published PDB files and predicted chemical shifts, and assigning the crosspeaks and the NOE strips of the simulated HSQC to the experimental ones by the Hungarian routine.

4.2 Scheme of the software

The current implementation of the Python 2.7 assignment software is summarized and schematized in the following paragraphs:

4.2.1 Input

The goal of the proposed assignment strategy is to "squeeze" as much information as possible from ^{1}H-^{15}N NMR spectra and published X-ray structures without relying on much more expensive ^{13}C labeled samples and more time-consuming NMR experiments. Thus, here are the requested inputs of the current implemented strategy:

Optional simulated NOEs (CORMA), RDCs

Required: protein PDB, experimental 3D ^{1}H ^{15}N NOESY HSQC peaklist, ShiftX2 simulated CS.

The major source of information of the current assignment procedure are the SHIFTX2 chemical shift predictions.[136] Other chemical shift predictors were tested (SPARTA+,[137] SHIFTX[138] and CAMSHIFT[139]) on a set of 2D ^{1}H ^{15}N HSQC spectra of GB3, ubiquitin, MMP12, S100β and lysozyme, but SHIFTX2 produced the best results in every trial in terms of root mean square deviation between simulated and experimental chemical shifts.

4.2.2 Assembly of the simulated 3D ^{1}H ^{15}N NOESY HSQC

The simulated NOEs are modelized by considering the atom coordinates and distances (from the protein PDB file) between the amide protons (NH) and all the other spin groups in the following way:

$$simulated\ NOE = \frac{m}{r^6} \tag{4.2.1}$$

Where *r* is the distance between the NHs and the spin groups and *m* is the number of spins composing the group (i.e. 3 for methyl groups). A threshold of $(4.5\ \text{Å})^{-6}$ is used to exclude too weak NOEs from the analysis. This simplistic way to describe NOEs neglects spin-diffusion and it is a current limit of the software. A more accurate description of the NOE should, and will be used in a next implementation. In a previous attempt, CORMA[140,141] was used to predict NOEs from a protein PDB knowing the mixing time of the experiment, however, the very old implementation of this software made it very impractical to be used for proteins with more than 100 residues.

The ^{1}H and ^{15}N frequencies are taken from the SHIFX2 output file (eventual missing frequencies are taken from the statistical BMRB values) and linked to the NOE values to form the simulated spectrum organized in a python list of lists.

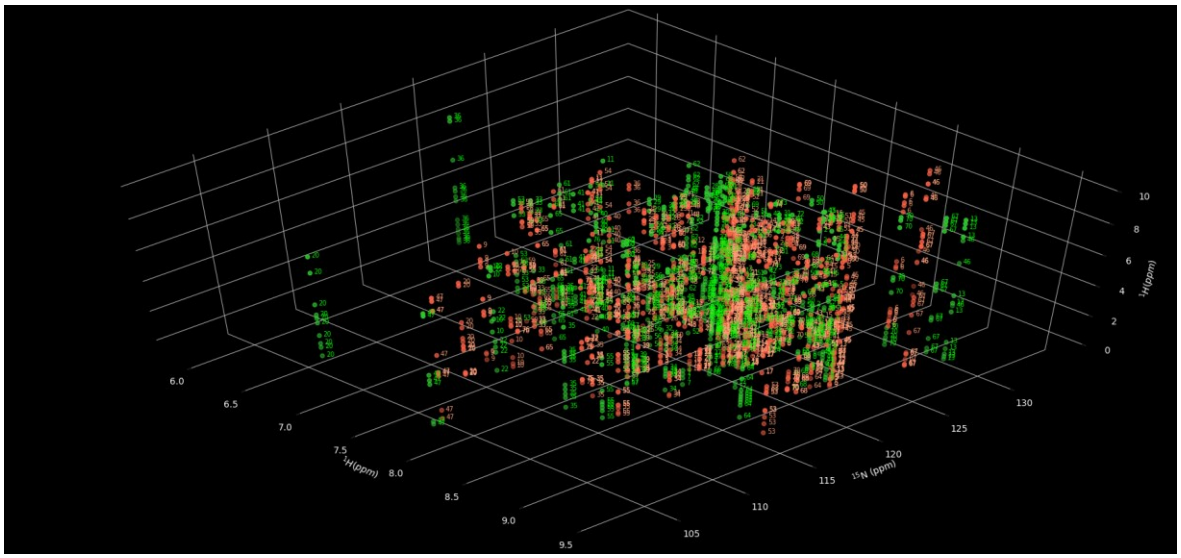

Fig 4.2.1 Graphical representation of simulated (green) and experimental (light red) 3D ^{1}H ^{15}N NOESY HSQC spectra of ubiquitin. The experimental spectrum was obtained at pH 7.0 at 293 K with a mixing time of 0.8 ms, the simulated one was originated from a crystallographic structure (PDB code: 3NHE).

↓

4.2.3 Filtering of datasets

The experimental peaklist is filtered by a static threshold of 10^{-4} that eliminates negative peaks and peaks originated from noise. Double peaks are also removed by discarding NOE duplicates originating from automatic peak picking, the double peak remover always includes at least one auto-peak. If a second peak is found, which differs from the HN frequency, within a tolerance of 0.055 ppm, then it is discarded. The difference in frequency between duplicated peaks is calculated in absolute value but also with sign in order to identify possible static biases. The crosspeaks intensities are then normalized to one.

Both the experimental NOE intensities and the simulated ones, calculated through Eq. 4.2.1, are clustered in 3 classes (3 = strong, 2 = medium, 1 = weak) by a K-means algorithm.[142] At the end of the clustering procedure, the crosspeaks intensities are replaced by the labels of the clusters (3, 2, 1).

4.2.4 Assignment

The experimental peaks in the HSQC are assigned to the peaks in the simulated spectrum with the Hungarian algorithm (Kuhn-Munkres algorithm[135]). This algorithm provides an optimal solution to assignment problems by minimizing a global cost function. In practice, it works by moving rows and columns of a distance matrix in order to find the global minimum of the trace, thus the assignment obtained in this way is an exact solution that depends only

on how the cost matrix was build. In this case each element D_{ij} of the distance matrix is evaluated by considering the differences in chemical shifts and magnitude of NOEs between the experimental i^{th} element and the simulated j^{th} element. The exact definition and implementation of the "distance" between experimental and simulated points of the 3D ^{1}H ^{15}N NOESY HSQC is described in paragraph 4.3.1.

4.2.5 Reliability

The reliability of the *Hungarian* assignment can be assessed with the gaussian density (fast execution) or STAUCSY (very accurate but slow execution) estimators. These original algorithms for assignment reliability estimation are described in the section 4.3.2.

4.3 Original Methods

4.3.1 Distance estimators

In order to perform the Hungarian assignment procedure, it is necessary to give an estimate of the "distance" between each simulated and experimental strip of the 3D ^{1}H ^{15}N NOESY HSQC. This distance that gave us the best results, that we dubbed d_{3D}, is computed in the following way:

$$f_s^k(x) = \sum_{i=0}^{N_{sim}^k} \frac{a_{i,k}}{\sqrt{2}\sigma_i} e^{\frac{(x-x_{i,k})^2}{2\sigma_i^2}} \; ; \; \sigma_i = \frac{\sigma_{i,BMRB}}{3}$$

$$f_e^l(x) = \sum_{i=0}^{N_{exp}^l} \frac{a_{i,l}}{\sqrt{2}\sigma} e^{\frac{(x-x_{i,l})^2}{2\sigma^2}} \; ; \; \sigma = \frac{\sigma_{avg,BMRB}}{3}$$

$$d_{NOE}(l,k) = \int |f_s^k(x) - f_e^l(x)| dx$$

$$d_{3D}(l,k) = (1-w_0)\sqrt{\frac{d_{HN}^2(\boldsymbol{x}_l,\boldsymbol{x}_k)}{\sigma_{HN,BMRB}^2} + \frac{d_N^2(\boldsymbol{x}_l,\boldsymbol{x}_k)}{\sigma_{N,BMRB}^2}} + w_0 d_{NOE}(l,k)$$

In the above formulae, d_{HN}^2 is the squared difference between the proton chemical shifts in the HSQC spectrum, d_N^2 is the squared difference between the proton chemical shifts in the HSQC spectrum, the $\sigma_{HN,BMRB}^2$ and $\sigma_{N,BMRB}^2$ are the variances for the amide proton and

nitrogen taken from the BMRB statistics. d_{NOE} is a distance obtained by calculating the integral of the absolute value of the difference between linear combination of gaussian functions built to represent the experimental and the simulated NOE crosspeaks. The amplitudes of the gaussians $a_{i,k}$ and $a_{i,l}$ are set to the values 1, 2, 3, which were assigned to the resonances by the K-means clustering of the simulated and experimental crosspeaks, the σ_i are the standard deviations for the simulated NOE crosspeaks, which are set to one third of standard deviation value taken from the BMRB statistics for the specific proton and type of residue, the σ are the standard deviations relative to the experimental NOE crosspeaks, since the assignment is not known, they are set to one third of the average standard deviation of proton chemical shifts values taken from the BMRB statistics, $x_{i,k}$ and $x_{i,l}$ are the chemical shifts relative to the simulated and experimental crosspeaks on which the gaussian functions are centered. The weight w_0, up to now, is empirically optimized but it can be also automatically set to a minimum cost value by applying a L-curve regularization approach.[143]

Another distance that was used in some tests, that we dubbed d_{3DH}, is computed in the following way:

$$d_{3DH}^2(\boldsymbol{x}_i;\boldsymbol{x}_j) = (1-w_0)\sqrt{\frac{d_{HN}^2(\boldsymbol{x}_i;\boldsymbol{x}_j)}{\sigma_{HN}^2}+\frac{d_N^2(\boldsymbol{x}_i;\boldsymbol{x}_j)}{\sigma_N^2}} + w_0 d_{NOE}^2(\boldsymbol{x}_i;\boldsymbol{x}_j)$$

$$d_{NOEH}^2(\boldsymbol{x}_i;\boldsymbol{x}_j) = \min_{l(k)}\left(\sum_k d_{H_{NOE}}^2(x_k;x_{l(k)}) + w_3 d_{rank}^2\left(x_k;x_{l(k)}\right)\right)$$

Where d_{HN}^2 is the squared difference between the proton CS in the HSQC, d_N^2 is the squared difference between the proton CS in the HSQC, σ_{HN}^2 and σ_N^2 the respective variances (calculated from the simulated CS) and w_0, w_1 and w_2 are weights empirically optimized. $d_{H_{NOE}}^2$ is the squared difference between the CS of a crosspeak present in the simulated strip with another in the experimental one, d_{rank}^2 is the difference in ranks (e.g. 3, 2 and 1 for strong, medium and weak) between the same crosspeaks and d_{NOEH}^2 is calculated as the minimum of the sum of $d_{H_{NOE}}^2 + w_3 d_{rank}^2$ obtained by performing an Hungarian algorithm to assign (the assignment is represented by the term $l(k)$ in the equations) the crosspeaks in the simulated strip to the experimental ones. Although this last strip to strip distance estimator d_{3DH}^2 provides some advantages, it is very time consuming and less robust than the d_{3D} estimator.

4.3.2 Reliability estimators

The Montecarlo STAUCSY algorithm was developed in order to find a way to estimate the reliability and consistent alternatives of an assignment without knowing the correct solution. The algorithm, was inspired by the Kendall's tau correlation coefficient[144] and the STOCSY[145] experiment (used in metabolomics). The instructions to perform the algorithm and the pseudocode of the Montecarlo STAUCSY are present below:

- Perturbate randomly n times both the ^{1}H and ^{15}N chemical shifts of the simulated dataset.
- Perform the chemical shift assignment for n times and build an assignment matrix **A** whose rows contains the assigned residues corresponding to the same peak identified by the row number, if you have m experimental 2D points to assign, **A** should be an $m\ x\ n$ matrix.
- Evaluate a "pseudo-Kendall's tau" between the rows of the assignment matrix **A** and build the Montecarlo STAUCSY matrix **S**:

$$
\begin{aligned}
&for\ i \in [0, m] \\
&\quad for\ j \in [0, m] \\
&\qquad c = 0 \\
&\qquad for\ \ k \in [0, n] \\
&\qquad\quad for\ \ l \in [0, n] \\
&\qquad\qquad if\ \ A_{ik} = A_{jl} \longrightarrow c = c + 1 \\
&\qquad S_{ij} = \frac{c}{n^2}
\end{aligned}
$$

The Montecarlo algorithm allow us to obtain a more robust assignment with alternatives. To better visualize the outcome of the STAUCSY algorithm the pseudo-tau values are organized in a matrix S_{ij} whose columns and rows are sorted with a reversed Cuthill–McKee algorithm[146] in order to minimize the bandwidth of this almost sparse matrix (see Fig. 4.3.1). By just looking at how many times during the Montecarlo procedure a certain experimental strip has been assigned to a simulated one it is possible to find alternatives to the minimum cost assignment. Moreover, by looking at the STUCSY matrix S_{ij}, if a row has a low tau value with itself and a non-zero tau with another row it might mean that the assignments of those rows can be exchanged with a minimum variation of the cost function.

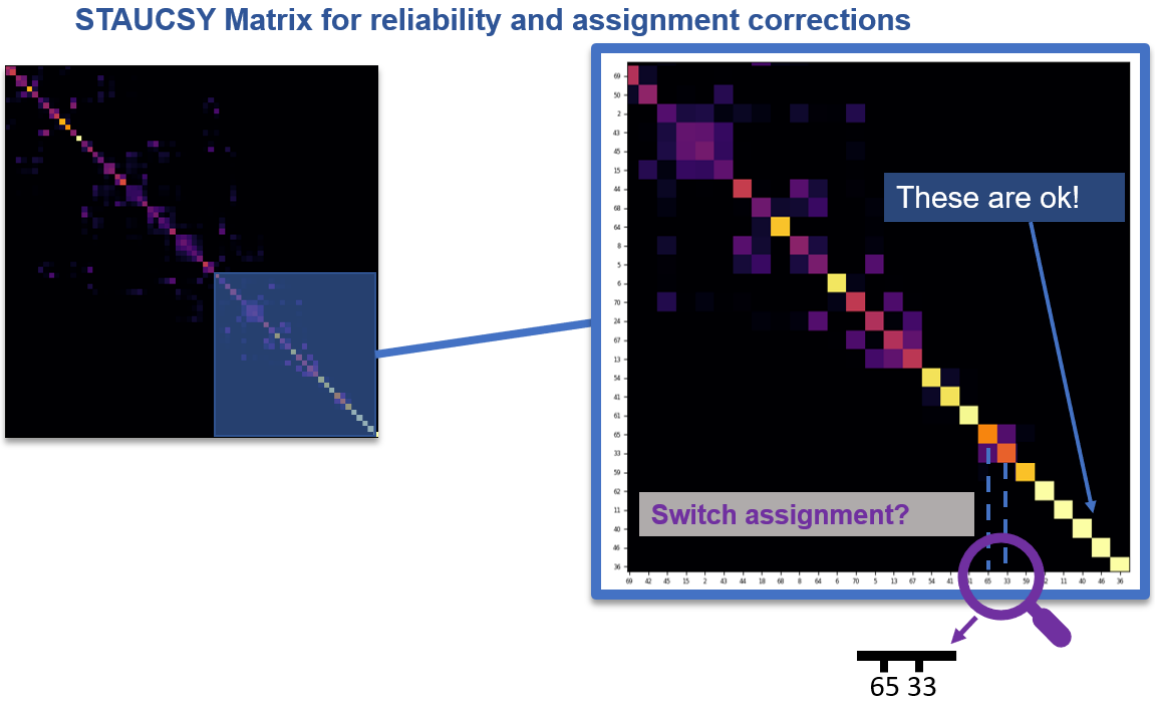

Fig. 4.3.1 Heatmap showing the STAUCSY matrix relative to an assignment performed on ubiquitin. White diagonal elements in the matrix never change their assignment during the Montecarlo perturbation, don't have any off-diagonal correlation and are placed on the bottom right side of the matrix, thanks to the reversed Cuthill–McKee algorithm. Darker elements instead are the ones that, during the Montecarlo perturbation change their assignment, a flux of exchange between assignment manifests as an off-diagonal correlation. If there is a single intense off-diagonal correlation, as in the example above for residues 65 and 33, may imply that the backbone assignment of these two residues can be exchanged with a minimum increase in the global cost.

Montecarlo STAUCSY is computational costly (up to 2 h of execution time with a performant laptop) and the random perturbation is arbitrary. If you are not interested in assignment alternatives, sometimes it can be better to give a fast reliability score with the "gaussian density score" that can be computed in this way:

$$\rho_j^{gauss} \propto \frac{e^{-d_{3D}^2(\boldsymbol{x}_{j,calc};\boldsymbol{x}_{j,exp})}}{\sum_{i=1,i\neq j}^{Ncalc} e^{-d_{3D}^2(\boldsymbol{x}_{j,calc};\boldsymbol{x}_{i,calc})} \sum_{i=1,i\neq j}^{Nexp} e^{-d_{3D}^2(\boldsymbol{x}_{j,exp};\boldsymbol{x}_{i,exp})}}$$

Where, the $\boldsymbol{x}_{j,calc}$ are the simulated points of a strip (containing both crosspeaks and HSQC frequencies) and the $\boldsymbol{x}_{j,exp}$ are the experimental ones. The higher is this score, the more the assignment is reliable. This "gaussian density" takes into account the distance between an experimental point and its assigned simulated ones considering that if the simulated and experimental point are in a dense region the assignment could be not so reliable. Although the *gaussian reliability* is faster than the Montecarlo STAUCSY, the latter one usually produces better discrimination between correct and incorrect assignments.

4.4 Results and Discussion

Up to now, this last version of the software, written in Python 2.7 on an Ubuntu virtual machine, has been tested only on ubiquitin and MMP12 providing 81% and 78% of maximum correct assignments, by optimizing the w_0 weights for each protein ($w_0^{MMP12} = 0.73; w_0^{ubi} = 0.87$), respectively. By using an average weight between the optimal weights for the two proteins ($w_0 = 0.8$), it is possible to obtain a 75% of correctly assigned residues for both proteins. The difference in the optimal w_0 parameter from MMP12 and ubiquitin depends on the fact that the spectra of the two proteins have different number of HSQC peaks (145 vs 67) and NOE crosspeaks (1466 vs 687). The distribution of reliability ranks of MMP12 and ubiquitin, from most reliable (1) to the least (145 or 67), obtained with the *Gaussian* and *STAUCSY* estimators is shown in the following pictures for both correctly assigned and incorrectly assigned residues, both for optimal weights and average weights, in order to compare the reliability estimators. For the STAUCSY algorithm a random perturbation of 25% of the standard deviation of the experimental NH proton chemical shifts was applied to all the proton frequencies, while a perturbation of 25% of the standard deviation of the experimental amide nitrogen chemical shifts was applied to the ^{15}N chemical shifts.

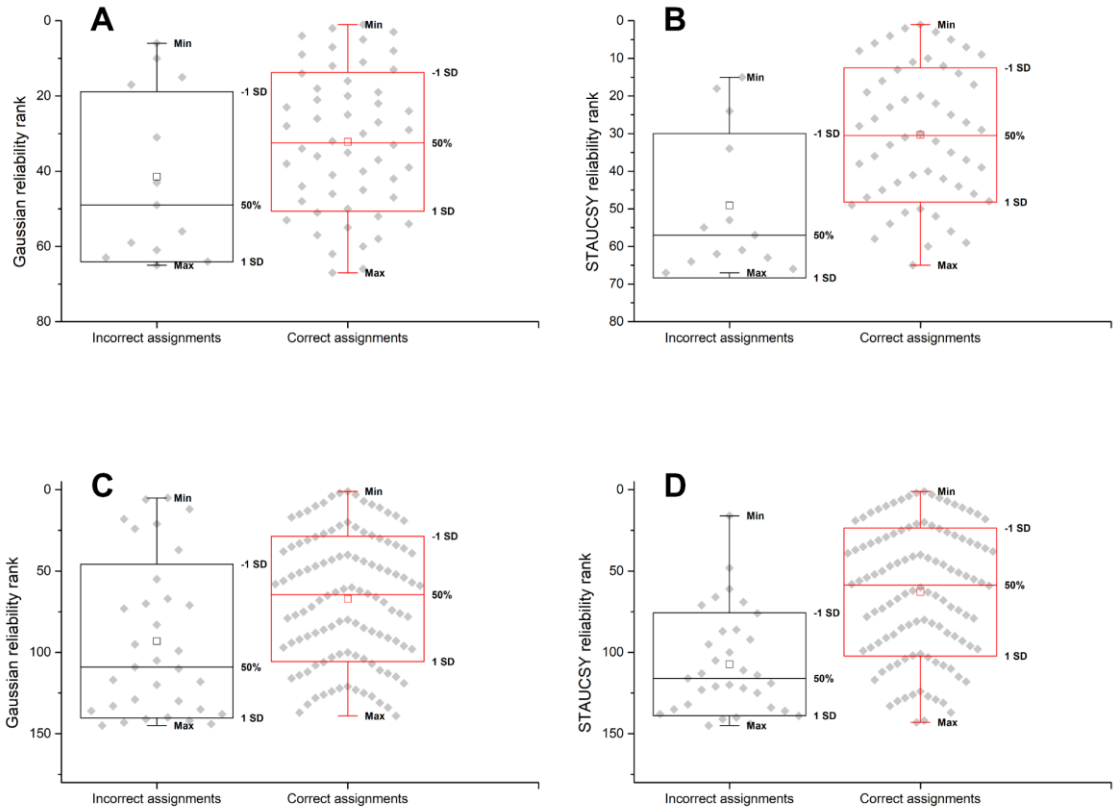

*Fig. 4.4.1: Rank distributions of correctly and incorrectly assigned residues for the "optimal weight" assignment ($w_0 = 0.73$ for MMP12 and $w_0 = 0.87$ for ubiquitin). **A)** Distribution of the reliability ranks for ubiquitin using the Gaussian reliability estimator. **B)** Distribution of the reliability ranks for ubiquitin using the STAUCSY reliability estimator. **C)** Distribution of the reliability ranks for MMP12 using the Gaussian reliability estimator. **D)** Distribution of the reliability ranks for MMP12 using the STAUCSY reliability estimator.*

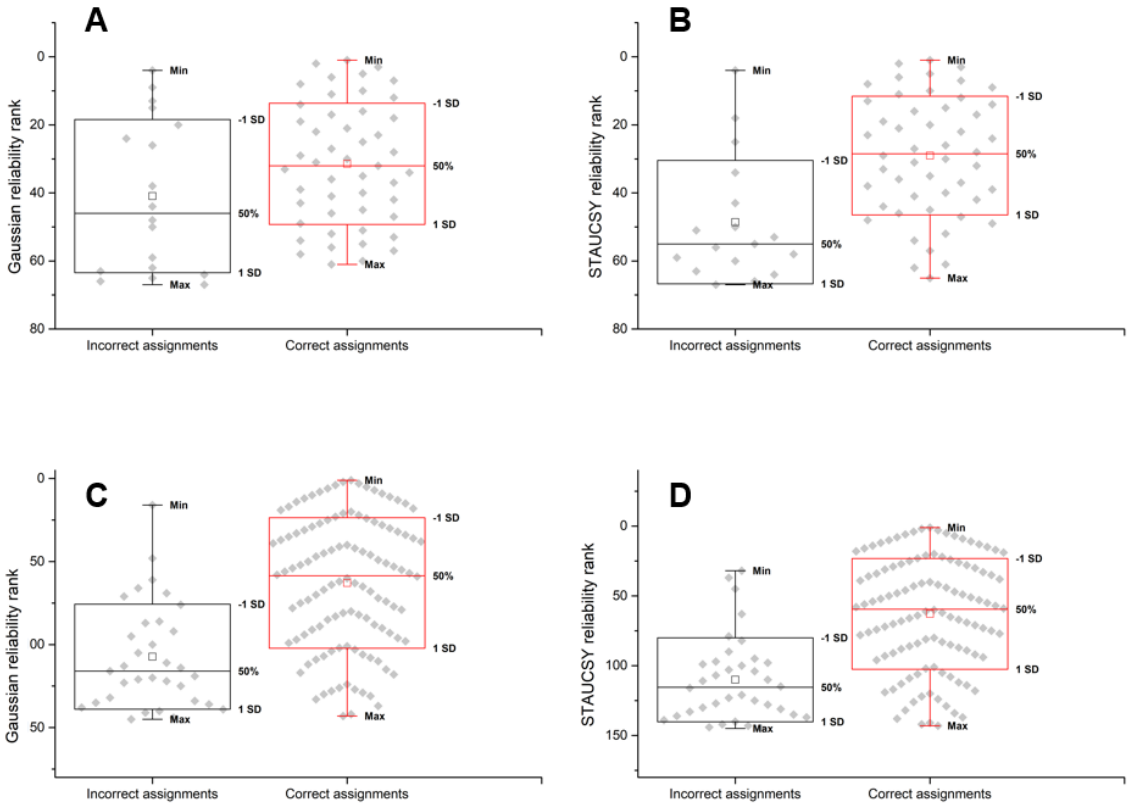

Fig. 4.4.2 Rank distributions of correctly and incorrectly assigned residues for the "average weight" assignment ($w_0 = 0.8$ for MMP12 and $w_0 = 0.8$ for ubiquitin). ***A)*** *Distribution of the reliability ranks for ubiquitin using the Gaussian reliability estimator.* ***B)*** *Distribution of the reliability ranks for ubiquitin using the STAUCSY reliability estimator.* ***C)*** *Distribution of the reliability ranks for MMP12 using the Gaussian reliability estimator.* ***D)*** *Distribution of the reliability ranks for MMP12 using the STAUCSY reliability estimator.*

The development of this software can provide several advantages for NMR spectroscopists, especially on saving time in assigning ^{1}H-^{15}N HSQC experiments needed for drug discovery and testing. In particular, the algorithms developed to predict the reliability of assignments seem to work in ranking the assignments from the strongest to weakest. In particular, with the STAUCSY algorithm we obtained better discrimination (both with optimized and average weights) between correctly and incorrectly assigned residues with respect to the Gaussian reliability predictor. The algorithm also provides alternative assignments that can be used to make corrections by the user.

4.5 Perspectives

We are currently adjusting the features of the last version of the program in order to train the software on peaklists coming from more proteins and then validate the results. In the

next implementation, the w_0 parameter of the d_{3D} estimator will be automatically set by a proper training, in function of the number of experimental NOEs and residues, or through the use of a L-curve routine.[143] I am currently developing a python version of CORMA[141] to be implemented in the software in order to substitute the naive approach of Eq 4.2.1 with a more rigorous calculation of a relaxation matrix. We are also considering the idea of adding TOCSY and T_1 sequences in the protocol. The ^{15}N-TOCSY-HSQC experiment,[147] when doable, provides information about the residue type, while T_1 measuring experiments[148] provide information about mobility. The information about mobility gives the possibility of assigning lower weights to the most mobile residues, which probably will have very different values of chemical shifts with respect to the ones calculated by SHIFTX2 from the protein PDB. Once better results will be obtained, in terms of number of proteins tested and correctness of the assignment, a proper graphical user interface will be developed for this software.

5 Conclusions

The relatively recent comprehension of the “prionic” and amyloidogenic nature of the proteins involved in the onset of Alzheimer’s disease and Parkinson’s disease radically changed the approach of scientists and clinicians in dealing with these neurodegenerative disorders by gathering the scientific community on studying the processes that lead to protein misfolding and aggregation. In this context, biophysics and computation methods managed to play a role in this process providing tools for the comprehension of the complex mechanisms of protein fibrillization and oligomerization.

This doctorate thesis dealt with different problems concerning the study of neurodegenerative diseases, particularly focusing on kinetics of aggregation, new diagnostic strategies, drug discovery and drug screening methodologies. In the first chapter I analyzed the aggregation kinetics of Aβ1-40. I carried out the analysis by performing unbiased (no fluorophore addition) NMR experiments to monitor the disappearance of the monomer signals. The data obtained in this way could not accurately fit with previously developed kinetic models based on a strong role of the secondary nucleation of fibrils. Thus, I developed an alternative kinetic model introducing a conversion step between reversible oligomers and fibrils. In the kinetic analysis I performed, I did not exclude secondary nucleation, but I did not find a significant contribution from secondary nucleation, a process that maybe can be more relevant at lower pH values, with respect to our experimental conditions. In the same work I highlighted the complementarity between liquid state NMR spectroscopy and ThT fluorescence. Parallel NMR and fluorescence experiments allowed me to parallelly monitor fibril formation and monomer depletion at the same time. The second chapter was instead dedicated to diagnostics.

The comprehension of the prion-like nature of α-syn brought the scientific community to the recent development of PMCA and RT-QuIC assays for the detection of α-syn aggregates in biological fluids. The sensitivity of these assays revealed to be strongly dependent on the fragmentation, nucleation and elongation kinetics of α-syn aggregates, which in turn depend on biophysical factors such as temperature, shaking modalities, pH, ionic strength, presence of preformed aggregates, presence of detergents and monomer starting concentration. Many of these variables were tested and the effects were analyzed in terms increase of detection sensitivity and differentiation among the added seed masses. In particular, I found that the linear relation between the logarithm of the seed mass and the

$t_{1/2}$ in PMCA/RT-QuIC experiments can be explained by applying a nucleated polymerization kinetic model with time dependent fragmentation. Fragmentation kinetics was found to play a major role in these protein aggregation assays, by enhancing fragmentation of fibrillary aggregates by the addition of glass beads particularly enhanced the detection sensitivity and the differentiation among added seeds. Among the tested variables we also found that the addition of human CSF decreased significantly the aggregation of α-syn.

The discovery of an antiaggregatory effect of human CSF on α-syn made all the scientists involved in this project question about which compounds present in biofluids could be the cause of this effect. From this observation, I started the “drug discovery” phase of the doctorate project, described in chapter 3, which began with the characterization of the effects of two biospecimens abundant in CSF and serum, namely HSA and HDL. HSA, at the physiological concentration found in human serum interacted with monomeric α-syn in a pH and ionic strength dependent manner and slowed the aggregation of α-syn significantly. This chaperone-like behavior of HSA, which is probably not responsible for the strong antiaggregatory effect observed for CSF, can be relevant in blood and serum, where, apart from the high level of HSA, high levels of α-syn are also physiologically present (it is highly expressed in red-blood cells). The understanding of the effects of HSA on the aggregation of α-syn will be for sure useful for manage the PMCA/RT-QuIC responses of blood-contaminated CSF samples or for the future developments of α-syn PMCA/RT-QuIC of plasma and serum samples. A stronger antiaggregatory effect was observed for Human plasma HDL (rich in apoA1), which decreased significantly the quantity of fibrillary and oligomeric aggregates produced by α-syn. Differently from what if was observed for HSA, we did not observed any relevant interaction between monomeric α-syn and HDL from ^{1}H ^{15}N HSQC NMR experiments, suggesting that a “remodeling” of α-syn aggregates may occur in the presence of apoA1-rich HDL. The observed antiaggregatory effect of plasma HDL on α-syn aggregation probably contributes to the antiaggregatory effect observed for human CSF and may also motivate the recent associations of lower apoA1 levels with decreased age at PD onset.[111,113]

This “drug-discovery in biofluids” line of research is currently ongoing. A more detailed characterization of the effects of lipoproteins on α-syn aggregation and a more general screening of the compounds present in CSF samples is currently being performed to find novel drug targets and to better understand the proteostasis of α-syn in CSF.

This experience I developed in protein-protein interaction studies made me realize the amount of job needed to perform drug screening by solution NMR and I started guessing if it was possible to find a way to automatically assign peaks of ^{1}H-^{15}N HSQC NMR spectra by using only ^{15}N labeled protein samples of a known structure (X-ray or good quality cryoEM structure). We observed that just using a 3D ^{1}H ^{15}N NOESY-HSQCs experiments together with chemical shift predictions by SHIFTX2, we can arrive to accurately assign about 75-80 % of the residues, reporting also a rank parameter related to the confidence of the specific residue assignment. Most of the algorithms used for this software (e.g. the reliability and distance estimators) were originally implemented in the context of the doctorate project.

Alzheimer's disease and Parkinson's disease are the two most common neurodegenerative disorders; together, they affect around 50 million people worldwide[7]. The social burden and medical costs of these progressive highly disabling disorders represent a tremendous challenge, also considering the progressive ageing of the population in developed countries. Nowadays, only symptomatic therapies are available for AD and PD patients and the journey to a full understanding of these diseases is still far from a conclusion. In this context, I hope that my modest work will be somehow useful, also for other scientists, to tackle this global health challenge.

References

1. Chiti, F. & Dobson, C. M. Amyloid formation by globular proteins under native conditions. *Nat. Chem. Biol.* **5,** 15–22 (2009).
2. Maji, S. K., Perrin, M. H., Sawaya, M. R., Jessberger, S., Vadodaria, K., Rissman, R. A., Singru, P. S., Nilsson, K. P. R., Simon, R., Schubert, D., Eisenberg, D., Rivier, J., Sawchenko, P., Vale, W. & Riek, R. Functional Amyloids as Natural Storage of Peptide Hormones in Pituitary Secretory Granules. *Science* **325,** 328–332 (2009).
3. Merlini, G. & Bellotti, V. Molecular Mechanisms of Amyloidosis. *N. Engl. J. Med.* **349,** 583–596 (2003).
4. Beck, M. W., Derrick, J. S., Suh, J.-M., Kim, M., Korshavn, K. J., Kerr, R. A., Cho, W. J., Larsen, S. D., Ruotolo, B. T., Ramamoorthy, A. & Lim, M. H. Minor Structural Variations of Small Molecules Tune Regulatory Activities toward Pathological Factors in Alzheimer's Disease. *ChemMedChem* **12,** 1828–1838 (2017).
5. Kumar, A., Singh, A. & Ekavali. A review on Alzheimer's disease pathophysiology and its management: an update. *Pharmacol. Rep.* **67,** 195–203 (2015).
6. Olanow, C. W. & Brundin, P. Parkinson's disease and alpha synuclein: is Parkinson's disease a prion-like disorder? *Mov. Disord. Off. J. Mov. Disord. Soc.* **28,** 31–40 (2013).
7. Goedert, M. Alzheimer's and Parkinson's diseases: The prion concept in relation to assembled Aβ, tau, and α-synuclein. *Science* **349,** 1255555 (2015).
8. Verma, M., Vats, A. & Taneja, V. Toxic species in amyloid disorders: Oligomers or mature fibrils. *Ann. Indian Acad. Neurol.* **18,** 138–145 (2015).
9. Meisl, G., Kirkegaard, J. B., Arosio, P., Michaels, T. C. T., Vendruscolo, M., Dobson, C. M., Linse, S. & Knowles, T. P. J. Molecular mechanisms of protein aggregation from global fitting of kinetic models. *Nat. Protoc.* **11,** 252 (2016).

10. Ferrone, F. Analysis of protein aggregation kinetics. *Methods Enzymol.* **309,** 256–274 (1999).
11. Bernacki, J. P. & Murphy, R. M. Model Discrimination and Mechanistic Interpretation of Kinetic Data in Protein Aggregation Studies. *Biophys. J.* **96,** 2871–2887 (2009).
12. Pallitto, M. M. & Murphy, R. M. A mathematical model of the kinetics of beta-amyloid fibril growth from the denatured state. *Biophys. J.* **81,** 1805–1822 (2001).
13. Erten-Lyons, D., Woltjer, R. L., Dodge, H., Nixon, R., Vorobik, R., Calvert, J. F., Leahy, M., Montine, T. & Kaye, J. Factors associated with resistance to dementia despite high Alzheimer disease pathology. *Neurology* **72,** 354–360 (2009).
14. Fusco, G., Chen, S. W., Williamson, P. T. F., Cascella, R., Perni, M., Jarvis, J. A., Cecchi, C., Vendruscolo, M., Chiti, F., Cremades, N., Ying, L., Dobson, C. M. & De Simone, A. Structural basis of membrane disruption and cellular toxicity by α-synuclein oligomers. *Science* **358,** 1440–1443 (2017).
15. Yoshiike, Y., Kayed, R., Milton, S. C., Takashima, A. & Glabe, C. G. Pore-forming proteins share structural and functional homology with amyloid oligomers. *Neuromolecular Med.* **9,** 270–275 (2007).
16. Serra-Batiste, M., Ninot-Pedrosa, M., Bayoumi, M., Gairí, M., Maglia, G. & Carulla, N. Aβ42 assembles into specific β-barrel pore-forming oligomers in membrane-mimicking environments. *Proc. Natl. Acad. Sci. U. S. A.* **113,** 10866–10871 (2016).
17. Thibaudeau, T. A., Anderson, R. T. & Smith, D. M. A common mechanism of proteasome impairment by neurodegenerative disease-associated oligomers. *Nat. Commun.* **9,** 1097 (2018).
18. Klein, A. M., Kowall, N. W. & Ferrante, R. J. Neurotoxicity and Oxidative Damage of Beta Amyloid 1–42 versus Beta Amyloid 1–40 in the Mouse Cerebral Cortex. *Ann. N. Y. Acad. Sci.* **893,** 314–320 (1999).

19. Oosawa, F. & Kasai, M. A theory of linear and helical aggregations of macromolecules. *J. Mol. Biol.* **4,** 10–21 (1962).
20. Foderà, V., Librizzi, F., Groenning, M., van de Weert, M. & Leone, M. Secondary Nucleation and Accessible Surface in Insulin Amyloid Fibril Formation. *J. Phys. Chem. B* **112,** 3853–3858 (2008).
21. Linse, S. Monomer-dependent secondary nucleation in amyloid formation. *Biophys. Rev.* **9,** 329–338 (2017).
22. Saborio, G. P., Permanne, B. & Soto, C. Sensitive detection of pathological prion protein by cyclic amplification of protein misfolding. *Nature* **411,** 810 (2001).
23. Atarashi, R., Sano, K., Satoh, K. & Nishida, N. Real-time quaking-induced conversion: a highly sensitive assay for prion detection. *Prion* **5,** 150–153 (2011).
24. Paciotti, S., Bellomo, G., Gatticchi, L. & Parnetti, L. Are We Ready for Detecting α-Synuclein Prone to Aggregation in Patients? The Case of “Protein-Misfolding Cyclic Amplification” and “Real-Time Quaking-Induced Conversion” as Diagnostic Tools. *Front. Neurol.* **9,** (2018).
25. Steiner, J. A., Angot, E. & Brundin, P. A deadly spread: cellular mechanisms of α-synuclein transfer. *Cell Death Differ.* **18,** 1425–1433 (2011).
26. Klein, A. D. & Mazzulli, J. R. Is Parkinson’s disease a lysosomal disorder? *Brain* **141,** 2255–2262 (2018).
27. Mesquita, S. D., Louveau, A., Vaccari, A., Smirnov, I., Cornelison, R. C., Kingsmore, K. M., Contarino, C., Onengut-Gumuscu, S., Farber, E., Raper, D., Viar, K. E., Powell, R. D., Baker, W., Dabhi, N., Bai, R., Cao, R., Hu, S., Rich, S. S., Munson, J. M., Lopes, M. B., Overall, C. C., Acton, S. T. & Kipnis, J. Functional aspects of meningeal lymphatics in ageing and Alzheimer’s disease. *Nature* **560,** 185–191 (2018).

28. Sui, Y.-T., Bullock, K. M., Erickson, M. A., Zhang, J. & Banks, W. A. Alpha synuclein is transported into and out of the brain by the blood–brain barrier. *Peptides* **62,** 197–202 (2014).

29. Barbour, R., Kling, K., Anderson, J. P., Banducci, K., Cole, T., Diep, L., Fox, M., Goldstein, J. M., Soriano, F., Seubert, P. & Chilcote, T. J. Red blood cells are the major source of alpha-synuclein in blood. *Neurodegener. Dis.* **5,** 55–59 (2008).

30. Padayachee, E. R., Zetterberg, H., Portelius, E., Borén, J., Molinuevo, J. L., Andreasen, N., Cukalevski, R., Linse, S., Blennow, K. & Andreasson, U. Cerebrospinal fluid-induced retardation of amyloid β aggregation correlates with Alzheimer's disease and the APOE ε4 allele. *Brain Res.* **1651,** 11–16 (2016).

31. Ferrone, F. A., Hofrichter, J. & Eaton, W. A. Kinetics of sickle hemoglobin polymerization. II. A double nucleation mechanism. *J. Mol. Biol.* **183,** 611–631 (1985).

32. Cohen, S. I. A., Vendruscolo, M., Welland, M. E., Dobson, C. M., Terentjev, E. M. & Knowles, T. P. J. Nucleated polymerization with secondary pathways. I. Time evolution of the principal moments. *J. Chem. Phys.* **135,** 065105 (2011).

33. Arosio, P., Knowles, T. P. J. & Linse, S. On the lag phase in amyloid fibril formation. *Phys. Chem. Chem. Phys.* **17,** 7606–7618 (2015).

34. Fauerbach, J. A., Yushchenko, D. A., Shahmoradian, S. H., Chiu, W., Jovin, T. M. & Jares-Erijman, E. A. Supramolecular Non-Amyloid Intermediates in the Early Stages of α-Synuclein Aggregation. *Biophys. J.* **102,** 1127–1136 (2012).

35. Lee, J., Culyba, E. K., Powers, E. T. & Kelly, J. W. Amyloid-β Forms Fibrils by Nucleated Conformational Conversion of Oligomers. *Nat. Chem. Biol.* **7,** 602–609 (2011).

36. Fu, Z., Aucoin, D., Ahmed, M., Ziliox, M., Van Nostrand, W. E. & Smith, S. O. Capping of Aβ42 Oligomers by Small Molecule Inhibitors. *Biochemistry* **53,** 7893–7903 (2014).

37. Bellomo, G., Bologna, S., Gonnelli, L., Ravera, E., Fragai, M., Lelli, M. & Luchinat, C. Aggregation kinetics of the Aβ1–40 peptide monitored by NMR. *Chem. Commun.* **54,** 7601–7604 (2018).

38. Wu, D. H., Chen, A. D. & Johnson, C. S. An Improved Diffusion-Ordered Spectroscopy Experiment Incorporating Bipolar-Gradient Pulses. *J. Magn. Reson.* **115,** 260–264 (1995).

39. Lichstein, H. C. & Soule, M. H. Studies of the Effect of Sodium Azide on Microbic Growth and Respiration. *J. Bacteriol.* **47,** 221–230 (1944).

40. Spillantini, M. G., Schmidt, M. L., Lee, V. M., Trojanowski, J. Q., Jakes, R. & Goedert, M. Alpha-synuclein in Lewy bodies. *Nature* **388,** 839–840 (1997).

41. Parnetti, L., Chiasserini, D., Persichetti, E., Eusebi, P., Varghese, S., Qureshi, M. M., Dardis, A., Deganuto, M., Carlo, C., Castrioto, A., Balducci, C., Paciotti, S., Tambasco, N., Bembi, B., Bonanni, L., Onofrj, M., Rossi, A., Beccari, T., El-Agnaf, O. & Calabresi, P. Cerebrospinal fluid lysosomal enzymes and alpha-synuclein in Parkinson's disease. *Mov. Disord.* **29,** 1019–1027 (2014).

42. Sidransky, E. & Lopez, G. The link between the GBA gene and parkinsonism. *Lancet Neurol.* **11,** 986–998 (2012).

43. Li, J.-Q., Tan, L. & Yu, J.-T. The role of the LRRK2 gene in Parkinsonism. *Mol. Neurodegener.* **9,** (2014).

44. Hoffmann, A.-C., Minakaki, G., Menges, S., Salvi, R., Savitskiy, S., Kazman, A., Miranda, H. V., Mielenz, D., Klucken, J., Winkler, J. & Xiang, W. Extracellular aggregated alpha synuclein primarily triggers lysosomal dysfunction in neural cells prevented by trehalose. *Sci. Rep.* **9,** 544 (2019).

45. Noyce, A. J., Lees, A. J. & Schrag, A.-E. The prediagnostic phase of Parkinson's disease. *J Neurol Neurosurg Psychiatry* **87,** 871–878 (2016).

46. Eusebi, P., Giannandrea, D., Biscetti, L., Abraha, I., Chiasserini, D., Orso, M., Calabresi, P. & Parnetti, L. Diagnostic utility of cerebrospinal fluid α-synuclein in Parkinson's disease: A systematic review and meta-analysis. *Mov. Disord.* **32,** 1389–1400 (2017).

47. Majbour, N. K., Vaikath, N. N., van Dijk, K. D., Ardah, M. T., Varghese, S., Vesterager, L. B., Montezinho, L. P., Poole, S., Safieh-Garabedian, B., Tokuda, T., Teunissen, C. E., Berendse, H. W., van de Berg, W. D. J. & El-Agnaf, O. M. A. Oligomeric and phosphorylated alpha-synuclein as potential CSF biomarkers for Parkinson's disease. *Mol. Neurodegener.* **11,** 7 (2016).

48. Parnetti, L., Castrioto, A., Chiasserini, D., Persichetti, E., Tambasco, N., El-Agnaf, O. & Calabresi, P. Cerebrospinal fluid biomarkers in Parkinson disease. *Nat. Rev. Neurol.* **9,** 131–140 (2013).

49. Majbour, N. K., Chiasserini, D., Vaikath, N. N., Eusebi, P., Tokuda, T., van de Berg, W., Parnetti, L., Calabresi, P. & El-Agnaf, O. M. A. Increased levels of CSF total but not oligomeric or phosphorylated forms of alpha-synuclein in patients diagnosed with probable Alzheimer's disease. *Sci. Rep.* **7,** (2017).

50. Tokuda, T., Qureshi, M. M., Ardah, M. T., Varghese, S., Shehab, S. a. S., Kasai, T., Ishigami, N., Tamaoka, A., Nakagawa, M. & El-Agnaf, O. M. A. Detection of elevated levels of α-synuclein oligomers in CSF from patients with Parkinson disease. *Neurology* **75,** 1766–1772 (2010).

51. Danzer, K. M., Kranich, L. R., Ruf, W. P., Cagsal-Getkin, O., Winslow, A. R., Zhu, L., Vanderburg, C. R. & McLean, P. J. Exosomal cell-to-cell transmission of alpha synuclein oligomers. *Mol. Neurodegener.* **7,** 42 (2012).

52. Shahnawaz, M., Tokuda, T., Waragai, M., Mendez, N., Ishii, R., Trenkwalder, C., Mollenhauer, B. & Soto, C. Development of a Biochemical Diagnosis of Parkinson

Disease by Detection of α-Synuclein Misfolded Aggregates in Cerebrospinal Fluid. *JAMA Neurol.* **74,** 163–172 (2017).

53. Fairfoul, G., McGuire, L. I., Pal, S., Ironside, J. W., Neumann, J., Christie, S., Joachim, C., Esiri, M., Evetts, S. G., Rolinski, M., Baig, F., Ruffmann, C., Wade-Martins, R., Hu, M. T. M., Parkkinen, L. & Green, A. J. E. Alpha-synuclein RT-QuIC in the CSF of patients with alpha-synucleinopathies. *Ann. Clin. Transl. Neurol.* **3,** 812–818 (2016).
54. Groveman, B. R., Orrù, C. D., Hughson, A. G., Raymond, L. D., Zanusso, G., Ghetti, B., Campbell, K. J., Safar, J., Galasko, D. & Caughey, B. Rapid and ultra-sensitive quantitation of disease-associated α-synuclein seeds in brain and cerebrospinal fluid by αSyn RT-QuIC. *Acta Neuropathol. Commun.* **6,** 7 (2018).
55. Sano, K., Atarashi, R., Satoh, K., Ishibashi, D., Nakagaki, T., Iwasaki, Y., Yoshida, M., Murayama, S., Mishima, K. & Nishida, N. Prion-Like Seeding of Misfolded α-Synuclein in the Brains of Dementia with Lewy Body Patients in RT-QUIC. *Mol. Neurobiol.* **55,** 3916–3930 (2018).
56. Salvadores, N., Shahnawaz, M., Scarpini, E., Tagliavini, F. & Soto, C. Detection of misfolded Aβ oligomers for sensitive biochemical diagnosis of Alzheimer's disease. *Cell Rep.* **7,** 261–268 (2014).
57. Blennow, K. A Review of Fluid Biomarkers for Alzheimer's Disease: Moving from CSF to Blood. *Neurol. Ther.* **6,** 15–24 (2017).
58. Blennow, K. & Zetterberg, H. Biomarkers for Alzheimer's disease: current status and prospects for the future. *J. Intern. Med.* **0,**
59. Blennow, K. & Zetterberg, H. Cerebrospinal fluid biomarkers for Alzheimer's disease. *J. Alzheimers Dis. JAD* **18,** 413–417 (2009).
60. Rumund, A. van, Green, A. J. E., Fairfoul, G., Esselink, R. A. J., Bloem, B. R. & Verbeek, M. M. α-Synuclein real-time quaking-induced conversion in the cerebrospinal fluid of uncertain cases of parkinsonism. *Ann. Neurol.* **85,** 777–781 (2019).

61. Kang, U. J., Boehme, A. K., Fairfoul, G., Shahnawaz, M., Ma, T. C., Hutten, S. J., Green, A. & Soto, C. Comparative study of cerebrospinal fluid α-synuclein seeding aggregation assays for diagnosis of Parkinson's disease. *Mov. Disord.* **34,** 536–544 (2019).

62. Shevchik, V. E., Condemine, G. & Robert-Baudouy, J. Characterization of DsbC, a periplasmic protein of Erwinia chrysanthemi and Escherichia coli with disulfide isomerase activity. *EMBO J.* **13,** 2007–2012 (1994).

63. Huang, C., Ren, G., Zhou, H. & Wang, C. A new method for purification of recombinant human alpha-synuclein in Escherichia coli. *Protein Expr. Purif.* **42,** 173–177 (2005).

64. Shammas, S. L., Knowles, T. P. J., Baldwin, A. J., MacPhee, C. E., Welland, M. E., Dobson, C. M. & Devlin, G. L. Perturbation of the Stability of Amyloid Fibrils through Alteration of Electrostatic Interactions. *Biophys. J.* **100,** 2783–2791 (2011).

65. Cohlberg, J. A., Li, J., Uversky, V. N. & Fink, A. L. Heparin and other glycosaminoglycans stimulate the formation of amyloid fibrils from alpha-synuclein in vitro. *Biochemistry* **41,** 1502–1511 (2002).

66. Giehm, L. & Otzen, D. E. Strategies to increase the reproducibility of protein fibrillization in plate reader assays. *Anal. Biochem.* **400,** 270–281 (2010).

67. Arosio, P., Cukalevski, R., Frohm, B., Knowles, T. P. J. & Linse, S. Quantification of the Concentration of Aβ42 Propagons during the Lag Phase by an Amyloid Chain Reaction Assay. *J. Am. Chem. Soc.* **136,** 219–225 (2014).

68. Linse, S. Mechanism of amyloid protein aggregation and the role of inhibitors. *Pure Appl. Chem.* **91,** 211–229 (2019).

69. Runge, C. Ueber die numerische Auflösung von Differentialgleichungen. *Math. Ann.* **46,** 167–178 (1895).

70. Pujols, J., Peña-Díaz, S., Lázaro, D. F., Peccati, F., Pinheiro, F., González, D., Carija, A., Navarro, S., Conde-Giménez, M., García, J., Guardiola, S., Giralt, E., Salvatella,

X., Sancho, J., Sodupe, M., Outeiro, T. F., Dalfó, E. & Ventura, S. Small molecule inhibits α-synuclein aggregation, disrupts amyloid fibrils, and prevents degeneration of dopaminergic neurons. *Proc. Natl. Acad. Sci.* **115,** 10481–10486 (2018).

71. Giehm, L., Oliveira, C. L. P., Christiansen, G., Pedersen, J. S. & Otzen, D. E. SDS-induced fibrillation of alpha-synuclein: an alternative fibrillation pathway. *J. Mol. Biol.* **401,** 115–133 (2010).
72. Kurnik, M., Sahin, C., Andersen, C. B., Lorenzen, N., Giehm, L., Mohammad-Beigi, H., Jessen, C. M., Pedersen, J. S., Christiansen, G., Petersen, S. V., Staal, R., Krishnamurthy, G., Pitts, K., Reinhart, P. H., Mulder, F. A. A., Mente, S., Hirst, W. D. & Otzen, D. E. Potent α-Synuclein Aggregation Inhibitors, Identified by High-Throughput Screening, Mainly Target the Monomeric State. *Cell Chem. Biol.* **25,** 1389-1402.e9 (2018).
73. Pöschel, T., Brilliantov, N. V. & Frömmel, C. Kinetics of Prion Growth. *Biophys. J.* **85,** 3460–3474 (2003).
74. Jessen, N. A., Munk, A. S. F., Lundgaard, I. & Nedergaard, M. The Glymphatic System: A Beginner's Guide. *Neurochem. Res.* **40,** 2583–2599 (2015).
75. Sweeney, M. D. & Zlokovic, B. V. A lymphatic waste-disposal system implicated in Alzheimer's disease. *Nature* (2018). doi:10.1038/d41586-018-05763-0
76. Iliff, J. J., Wang, M., Liao, Y., Plogg, B. A., Peng, W., Gundersen, G. A., Benveniste, H., Vates, G. E., Deane, R., Goldman, S. A., Nagelhus, E. A. & Nedergaard, M. A Paravascular Pathway Facilitates CSF Flow Through the Brain Parenchyma and the Clearance of Interstitial Solutes, Including Amyloid β. *Sci. Transl. Med.* **4,** 147ra111-147ra111 (2012).
77. Valdinocci, D., Radford, R. A. W., Siow, S. M., Chung, R. S. & Pountney, D. L. Potential Modes of Intercellular α-Synuclein Transmission. *Int. J. Mol. Sci.* **18,** (2017).

78. Iwai, A., Yoshimoto, M., Masliah, E. & Saitoh, T. Non-A beta component of Alzheimer's disease amyloid (NAC) is amyloidogenic. *Biochemistry* **34,** 10139–10145 (1995).

79. Iwai, A., Masliah, E., Yoshimoto, M., Ge, N., Flanagan, L., de Silva, H. A., Kittel, A. & Saitoh, T. The precursor protein of non-A beta component of Alzheimer's disease amyloid is a presynaptic protein of the central nervous system. *Neuron* **14,** 467–475 (1995).

80. Terakawa, M. S., Lin, Y., Kinoshita, M., Kanemura, S., Itoh, D., Sugiki, T., Okumura, M., Ramamoorthy, A. & Lee, Y.-H. Impact of membrane curvature on amyloid aggregation. *Biochim. Biophys. Acta BBA - Biomembr.* **1860,** 1741–1764 (2018).

81. Pineda, A. & Burré, J. Modulating membrane binding of α-synuclein as a therapeutic strategy. *Proc. Natl. Acad. Sci. U. S. A.* **114,** 1223–1225 (2017).

82. Bruinsma, I. B., Bruggink, K. A., Kinast, K., Versleijen, A. A. M., Segers-Nolten, I. M. J., Subramaniam, V., Kuiperij, H. B., Boelens, W., Waal, R. M. W. de & Verbeek, M. M. Inhibition of α-synuclein aggregation by small heat shock proteins. *Proteins Struct. Funct. Bioinforma.* **79,** 2956–2967 (2011).

83. Cox, D., Whiten, D. R., Brown, J. W. P., Horrocks, M. H., Gil, R. S., Dobson, C. M., Klenerman, D., Oijen, A. M. van & Ecroyd, H. The small heat shock protein Hsp27 binds α-synuclein fibrils, preventing elongation and cytotoxicity. *J. Biol. Chem.* **293,** 4486–4497 (2018).

84. Jones, D. R., Moussaud, S. & McLean, P. Targeting heat shock proteins to modulate α-synuclein toxicity. *Ther. Adv. Neurol. Disord.* **7,** 33–51 (2014).

85. Moors, T., Paciotti, S., Chiasserini, D., Calabresi, P., Parnetti, L., Beccari, T. & Berg, W. D. J. van de. Lysosomal Dysfunction and α-Synuclein Aggregation in Parkinson's Disease: Diagnostic Links. *Mov. Disord.* **31,** 791–801 (2016).

86. Bennett, M. C., Bishop, J. F., Leng, Y., Chock, P. B., Chase, T. N. & Mouradian, M. M. Degradation of α-Synuclein by Proteasome. *J. Biol. Chem.* **274,** 33855–33858 (1999).

87. Bernis, M. E., Babila, J. T., Breid, S., Wüsten, K. A., Wüllner, U. & Tamgüney, G. Prion-like propagation of human brain-derived alpha-synuclein in transgenic mice expressing human wild-type alpha-synuclein. *Acta Neuropathol. Commun.* **3,** 75 (2015).

88. Braak, H., Bohl, J. R., Müller, C. M., Rüb, U., de Vos, R. A. I. & Del Tredici, K. Stanley Fahn Lecture 2005: The staging procedure for the inclusion body pathology associated with sporadic Parkinson's disease reconsidered. *Mov. Disord. Off. J. Mov. Disord. Soc.* **21,** 2042–2051 (2006).

89. Cerri, S., Ghezzi, C., Sampieri, M., Siani, F., Avenali, M., Dornini, G., Zangaglia, R., Minafra, B. & Blandini, F. The Exosomal/Total α-Synuclein Ratio in Plasma Is Associated With Glucocerebrosidase Activity and Correlates With Measures of Disease Severity in PD Patients. *Front. Cell. Neurosci.* **12,** (2018).

90. Manne, S., Kondru, N., Hepker, M., Jin, H., Anantharam, V., Lewis, M., Huang, X., Kanthasamy, A. & Kanthasamy, A. G. Ultrasensitive Detection of Aggregated α-Synuclein in Glial Cells, Human Cerebrospinal Fluid, and Brain Tissue Using the RT-QuIC Assay: New High-Throughput Neuroimmune Biomarker Assay for Parkinsonian Disorders. *J. Neuroimmune Pharmacol. Off. J. Soc. NeuroImmune Pharmacol.* (2019). doi:10.1007/s11481-019-09835-4

91. Menéndez-González, M., Padilla-Zambrano, H. S., Tomás-Zapico, C. & García, B. F. Clearing Extracellular Alpha-Synuclein from Cerebrospinal Fluid: A New Therapeutic Strategy in Parkinson's Disease. *Brain Sci.* **8,** (2018).

92. Emamzadeh, F. N. & Allsop, D. α-Synuclein Interacts with Lipoproteins in Plasma. *J. Mol. Neurosci.* **63,** 165–172 (2017).

93. Feingold, K. R. & Grunfeld, C. in *Endotext* (eds. De Groot, L. J., Chrousos, G., Dungan, K., Feingold, K. R., Grossman, A., Hershman, J. M., Koch, C., Korbonits, M.,

McLachlan, R., New, M., Purnell, J., Rebar, R., Singer, F. & Vinik, A.) (MDText.com, Inc., 2000). at <http://www.ncbi.nlm.nih.gov/books/NBK305896/>

94. Vitali, C., Wellington, C. L. & Calabresi, L. HDL and cholesterol handling in the brain. *Cardiovasc. Res.* **103,** 405–413 (2014).

95. Bibow, S., Polyhach, Y., Eichmann, C., Chi, C. N., Kowal, J., Albiez, S., McLeod, R. A., Stahlberg, H., Jeschke, G., Güntert, P. & Riek, R. Solution structure of discoidal high-density lipoprotein particles with a shortened apolipoprotein A-I. *Nat. Struct. Mol. Biol.* **24,** 187–193 (2017).

96. Emamzadeh, F. N. Role of Apolipoproteins and α-Synuclein in Parkinson's Disease. *J. Mol. Neurosci.* **62,** 344–355 (2017).

97. Bales, K. R. Brain lipid metabolism, apolipoprotein E and the pathophysiology of Alzheimer's disease. *Neuropharmacology* **59,** 295–302 (2010).

98. Orth, M. & Bellosta, S. Cholesterol: Its Regulation and Role in Central Nervous System Disorders. *Cholesterol* (2012). doi:10.1155/2012/292598

99. Pitas, R. E., Boyles, J. K., Lee, S. H., Hui, D. & Weisgraber, K. H. Lipoproteins and their receptors in the central nervous system. Characterization of the lipoproteins in cerebrospinal fluid and identification of apolipoprotein B,E(LDL) receptors in the brain. *J. Biol. Chem.* **262,** 14352–14360 (1987).

100. Mahley, R. W. Central Nervous System Lipoproteins. *Arterioscler. Thromb. Vasc. Biol.* **36,** 1305–1315 (2016).

101. Fagan, A. M., Younkin, L. H., Morris, J. C., Fryer, J. D., Cole, T. G., Younkin, S. G. & Holtzman, D. M. Differences in the Aβ40/Aβ42 ratio associated with cerebrospinal fluid lipoproteins as a function of apolipoprotein E genotype. *Ann. Neurol.* **48,** 201–210 (2000).

102. Qian, J., Wolters, F. J., Beiser, A., Haan, M., Ikram, M. A., Karlawish, J., Langbaum, J. B., Neuhaus, J. M., Reiman, E. M., Roberts, J. S., Seshadri, S., Tariot, P. N., Woods,

B. M., Betensky, R. A. & Blacker, D. APOE-related risk of mild cognitive impairment and dementia for prevention trials: An analysis of four cohorts. *PLOS Med.* **14,** e1002254 (2017).

103. Perrier, V., Imberdis, T., Lafon, P.-A., Cefis, M., Wang, Y., Huetter, E., Arnaud, J.-D., Alvarez-Martinez, T., Guern, N. L., Maquart, G., Lagrost, L. & Desrumaux, C. Plasma cholesterol level determines in vivo prion propagation. *J. Lipid Res.* **58,** 1950–1961 (2017).
104. Safar, J. G., Wille, H., Geschwind, M. D., Deering, C., Latawiec, D., Serban, A., King, D. J., Legname, G., Weisgraber, K. H., Mahley, R. W., Miller, B. L., DeArmond, S. J. & Prusiner, S. B. Human prions and plasma lipoproteins. *Proc. Natl. Acad. Sci. U. S. A.* **103,** 11312–11317 (2006).
105. Corder, E. H., Saunders, A. M., Strittmatter, W. J., Schmechel, D. E., Gaskell, P. C., Small, G. W., Roses, A. D., Haines, J. L. & Pericak-Vance, M. A. Gene dose of apolipoprotein E type 4 allele and the risk of Alzheimer's disease in late onset families. *Science* **261,** 921–923 (1993).
106. Liu, C.-C., Kanekiyo, T., Xu, H. & Bu, G. Apolipoprotein E and Alzheimer disease: risk, mechanisms and therapy. *Nat. Rev. Neurol.* **9,** 106–118 (2013).
107. Poirier, J., Davignon, J., Bouthillier, D., Kogan, S., Bertrand, P. & Gauthier, S. Apolipoprotein E polymorphism and Alzheimer's disease. *Lancet Lond. Engl.* **342,** 697–699 (1993).
108. Federoff, M., Jimenez-Rolando, B., Nalls, M. A. & Singleton, A. B. A large study reveals no Association between APOE and Parkinson's disease. *Neurobiol. Dis.* **46,** 389–392 (2012).
109. Qiang, J. K., Wong, Y. C., Siderowf, A., Hurtig, H. I., Xie, S. X., Lee, V. M.-Y., Trojanowski, J. Q., Yearout, D., Leverenz, J., Montine, T. J., Stern, M., Mendick, S.,

Jennings, D., Zabetian, C., Marek, K. & Chen-Plotkin, A. S. Plasma Apolipoprotein A1 as a Biomarker for Parkinson's Disease. *Ann. Neurol.* **74,** 119–127 (2013).

110. Wang, E.-S., Sun, Y., Guo, J.-G., Gao, X., Hu, J.-W., Zhou, L., Hu, J. & Jiang, C.-C. Tetranectin and apolipoprotein A-I in cerebrospinal fluid as potential biomarkers for Parkinson's disease. *Acta Neurol. Scand.* **122,** 350–359 (2010).
111. Swanson, C. R., Li, K., Unger, T. L., Gallagher, M. D., Van Deerlin, V. M., Agarwal, P., Leverenz, J., Roberts, J., Samii, A., Gross, G. R., Hurtig, H., Rick, J., Weintraub, D., Trojanowski, J. Q., Zabetian, C. & Chen-Plotkin, A. S. Lower plasma ApoA1 levels are found in Parkinson's disease and associate with APOA1 genotype. *Mov. Disord. Off. J. Mov. Disord. Soc.* **30,** 805–812 (2015).
112. Marek, K., Jennings, D., Lasch, S., Siderowf, A., Tanner, C., Simuni, T., Coffey, C., Kieburtz, K., Flagg, E., Chowdhury, S., Poewe, W., Mollenhauer, B., Klinik, P.-E., Sherer, T., Frasier, M., Meunier, C., Rudolph, A., Casaceli, C., Seibyl, J., Mendick, S., Schuff, N., Zhang, Y., Toga, A., Crawford, K., Ansbach, A., De Blasio, P., Piovella, M., Trojanowski, J., Shaw, L., Singleton, A., Hawkins, K., Eberling, J., Brooks, D., Russell, D., Leary, L., Factor, S., Sommerfeld, B., Hogarth, P., Pighetti, E., Williams, K., Standaert, D., Guthrie, S., Hauser, R., Delgado, H., Jankovic, J., Hunter, C., Stern, M., Tran, B., Leverenz, J., Baca, M., Frank, S., Thomas, C.-A., Richard, I., Deeley, C., Rees, L., Sprenger, F., Lang, E., Shill, H., Obradov, S., Fernandez, H., Winters, A., Berg, D., Gauss, K., Galasko, D., Fontaine, D., Mari, Z., Gerstenhaber, M., Brooks, D., Malloy, S., Barone, P., Longo, K., Comery, T., Ravina, B., Grachev, I., Gallagher, K., Collins, M., Widnell, K. L., Ostrowizki, S., Fontoura, P., Ho, T., Luthman, J., Brug, M. van der, Reith, A. D. & Taylor, P. The Parkinson Progression Marker Initiative (PPMI). *Prog. Neurobiol.* **95,** 629–635 (2011).
113. Swanson, C. R., Berlyand, Y., Xie, S. X., Alcalay, R. N., Chahine, L. M. & Chen-Plotkin, A. S. Plasma ApoA1 Associates with Age at Onset and Motor Severity in Early

Parkinson Disease Patients. *Mov. Disord. Off. J. Mov. Disord. Soc.* **30,** 1648–1656 (2015).

114. Kim, J., Basak, J. M. & Holtzman, D. M. The Role of Apolipoprotein E in Alzheimer's Disease. *Neuron* **63,** 287–303 (2009).
115. Koch, S., Donarski, N., Goetze, K., Kreckel, M., Stuerenburg, H.-J., Buhmann, C. & Beisiegel, U. Characterization of four lipoprotein classes in human cerebrospinal fluid. *J. Lipid Res.* **42,** 1143–1151 (2001).
116. Roher, A. E., Maarouf, C. L., Sue, L. I., Hu, Y., Wilson, J. & Beach, T. G. Proteomics-Derived Cerebrospinal Fluid Markers of Autopsy-Confirmed Alzheimer's Disease. *Biomark. Biochem. Indic. Expo. Response Susceptibility Chem.* **14,** 493–501 (2009).
117. Song, H., Saito, K., Seishima, M., Noma, A., Katsuya Urakami & Nakashima, K. Cerebrospinal fluid apo E and apo A-I concentrations in early- and late-onset Alzheimer's disease. *Neurosci. Lett.* **231,** 175–178 (1997).
118. Johansson, P., Almqvist, E. G., Bjerke, M., Wallin, A., Johansson, J.-O., Andreasson, U., Blennow, K., Zetterberg, H. & Svensson, J. Reduced Cerebrospinal Fluid Concentration of Apolipoprotein A-I in Patients with Alzheimer's Disease. *J. Alzheimers Dis.* **59,** 1017–1026 (2017).
119. Bodenhausen, G. & Ruben, D. J. Natural abundance nitrogen-15 NMR by enhanced heteronuclear spectroscopy. *Chem. Phys. Lett.* **69,** 185–189 (1980).
120. Biancalana, M. & Koide, S. Molecular Mechanism of Thioflavin-T Binding to Amyloid Fibrils. *Biochim. Biophys. Acta* **1804,** 1405–1412 (2010).
121. Kayed, R., Head, E., Sarsoza, F., Saing, T., Cotman, C. W., Necula, M., Margol, L., Wu, J., Breydo, L., Thompson, J. L., Rasool, S., Gurlo, T., Butler, P. & Glabe, C. G. Fibril specific, conformation dependent antibodies recognize a generic epitope common to amyloid fibrils and fibrillar oligomers that is absent in prefibrillar oligomers. *Mol. Neurodegener.* **2,** 18 (2007).

122. Glabe, C. G. Structural classification of toxic amyloid oligomers. *J. Biol. Chem.* **283,** 29639–29643 (2008).

123. Fejzo, J., Lepre, C. & Xie, X. Application of NMR screening in drug discovery. *Curr. Top. Med. Chem.* **3,** 81–97 (2003).

124. Lamberto, G. R., Torres-Monserrat, V., Bertoncini, C. W., Salvatella, X., Zweckstetter, M., Griesinger, C. & Fernández, C. O. Toward the discovery of effective polycyclic inhibitors of alpha-synuclein amyloid assembly. *J. Biol. Chem.* **286,** 32036–32044 (2011).

125. Velander, P., Wu, L., Henderson, F., Zhang, S., Bevan, D. R. & Xu, B. Natural product-based amyloid inhibitors. *Biochem. Pharmacol.* **139,** 40–55 (2017).

126. Lopez del Amo, J. M., Fink, U., Dasari, M., Grelle, G., Wanker, E. E., Bieschke, J. & Reif, B. Structural Properties of EGCG-Induced, Nontoxic Alzheimer's Disease Aβ Oligomers. *J. Mol. Biol.* **421,** 517–524 (2012).

127. Bieschke, J., Herbst, M., Wiglenda, T., Friedrich, R. P., Boeddrich, A., Schiele, F., Kleckers, D., Lopez del Amo, J. M., Grüning, B. A., Wang, Q., Schmidt, M. R., Lurz, R., Anwyl, R., Schnoegl, S., Fändrich, M., Frank, R. F., Reif, B., Günther, S., Walsh, D. M. & Wanker, E. E. Small-molecule conversion of toxic oligomers to nontoxic β-sheet–rich amyloid fibrils. *Nat. Chem. Biol.* **8,** 93–101 (2012).

128. Arndt, J. W., Qian, F., Smith, B. A., Quan, C., Kilambi, K. P., Bush, M. W., Walz, T., Pepinsky, R. B., Bussière, T., Hamann, S., Cameron, T. O. & Weinreb, P. H. Structural and kinetic basis for the selectivity of aducanumab for aggregated forms of amyloid-β. *Sci. Rep.* **8,** 6412 (2018).

129. Cristóvão, J. S., Morris, V. K., Cardoso, I., Leal, S. S., Martínez, J., Botelho, H. M., Göbl, C., David, R., Kierdorf, K., Alemi, M., Madl, T., Fritz, G., Reif, B. & Gomes, C. M. The neuronal S100B protein is a calcium-tuned suppressor of amyloid-β aggregation. *Sci. Adv.* **4,** (2018).

130. Schmidt, E. & Güntert, P. A New Algorithm for Reliable and General NMR Resonance Assignment. *J. Am. Chem. Soc.* **134,** 12817–12829 (2012).
131. Jung, Y.-S. & Zweckstetter, M. Mars - robust automatic backbone assignment of proteins. *J. Biomol. NMR* **30,** 11–23 (2004).
132. Langmead, C. J. & Donald, B. R. An expectation/maximization nuclear vector replacement algorithm for automated NMR resonance assignments. *J. Biomol. NMR* **29,** 111–138 (2004).
133. McGregor, A. Graph Stream Algorithms: A Survey. *SIGMOD Rec* **43,** 9–20 (2014).
134. Schwalbe, H., Grimshaw, S. B., Spencer, A., Buck, M., Boyd, J., Dobson, C. M., Redfield, C. & Smith, L. J. A refined solution structure of hen lysozyme determined using residual dipolar coupling data. *Protein Sci. Publ. Protein Soc.* **10,** 677–688 (2001).
135. Kuhn, H. W. The Hungarian method for the assignment problem. *Nav. Res. Logist. Q.* **2,** 83–97 (1955).
136. Han, B., Liu, Y., Ginzinger, S. W. & Wishart, D. S. SHIFTX2: significantly improved protein chemical shift prediction. *J. Biomol. NMR* **50,** 43 (2011).
137. Shen, Y. & Bax, A. SPARTA+: a modest improvement in empirical NMR chemical shift prediction by means of an artificial neural network. *J. Biomol. NMR* **48,** 13–22 (2010).
138. Neal, S., Nip, A. M., Zhang, H. & Wishart, D. S. Rapid and accurate calculation of protein 1H, 13C and 15N chemical shifts. *J. Biomol. NMR* **26,** 215–240 (2003).
139. Kohlhoff, K. J., Robustelli, P., Cavalli, A., Salvatella, X. & Vendruscolo, M. Fast and Accurate Predictions of Protein NMR Chemical Shifts from Interatomic Distances. *J. Am. Chem. Soc.* **131,** 13894–13895 (2009).
140. Bertini, I., Felli, I. C., Luchinat, C. & Rosato, A. A complete relaxation matrix refinement of the solution structure of a paramagnetic metalloprotein: Reduced HiPIP I from Ectothiorhodospira halophila. *Proteins Struct. Funct. Bioinforma.* **24,** 158–164 (1996).

141. Borgias, B. A., Gochin, M., Kerwood, D. J. & James, T. L. Relaxation matrix analysis of 2D NMR data. *Prog. Nucl. Magn. Reson. Spectrosc.* **22,** 83–100 (1990).
142. Macqueen, J. Some methods for classification and analysis of multivariate observations. in *5-Th Berkeley Symp. Math. Stat. Probab.* 281–297 (1967).
143. Hansen, P. C. The L-Curve and its Use in the Numerical Treatment of Inverse Problems. in *Comput. Inverse Probl. Electrocardiol. Ed P Johnston Adv. Comput. Bioeng.* 119–142 (WIT Press, 2000).
144. Kendall, M. G. A New Measure of Rank Correlation. *Biometrika* **30,** 81–93 (1938).
145. Cloarec, O., Dumas, M.-E., Craig, A., Barton, R. H., Trygg, J., Hudson, J., Blancher, C., Gauguier, D., Lindon, J. C., Holmes, E. & Nicholson, J. Statistical total correlation spectroscopy: an exploratory approach for latent biomarker identification from metabolic 1H NMR data sets. *Anal. Chem.* **77,** 1282–1289 (2005).
146. Cuthill, E. & McKee, J. Reducing the Bandwidth of Sparse Symmetric Matrices. in *Proc. 1969 24th Natl. Conf.* 157–172 (ACM, 1969). doi:10.1145/800195.805928
147. Marion, D., Driscoll, P. C., Kay, L. E., Wingfield, P. T., Bax, A., Gronenborn, A. M. & Clore, G. M. Overcoming the overlap problem in the assignment of proton NMR spectra of larger proteins by use of three-dimensional heteronuclear proton-nitrogen-15 Hartmann-Hahn-multiple quantum coherence and nuclear Overhauser-multiple quantum coherence spectroscopy: application to interleukin 1.beta. *Biochemistry* **28,** 6150–6156 (1989).
148. Spera, S., Ikura, M. & Bax, A. Measurement of the exchange rates of rapidly exchanging amide protons: Application to the study of calmodulin and its complex with a myosin light chain kinase fragment. *J. Biomol. NMR* **1,** 155–165 (1991).

Acknowledgments

I would like to express my very great gratitude to Professor Claudio Luchinat for giving me the opportunity of taking the stimulating path of the International Doctorate in Structural Biology at CERM. His suggestions and advices have been always of great inspiration and guided me while facing difficult scientific problems or during the interpretation of the results.

Professor Lucilla Parnetti had great impact on the developments and outcomes of my research during my PhD. The collaboration we established gave me the opportunity to learn a lot about neurodegenerative diseases both from a clinical and biochemical point of view. Not all the students (and especially physicists working on computational stuff) working in life sciences have the opportunity of looking at both the "hospital" and the "laboratory" point of view and I will be always thankful to her for giving me such chance.

A special thanks goes also to Professor Moreno Lelli because of the passion by which he performs his research and because if I matured as a scientist in these three years is also because I worked at his side learning from his advices and speeches.

If some of the projects in which I was involved into went well I have to thank the presence of Professor Marco Fragai and his critical sense. Professor Marco Fragai has been always helping me since the very first phase of the doctorate, supporting my ideas and providing always stimulating and constructive advices.

I would like also to thank my "cermian" collaborators, first of all Linda who is the real supporting column of CERM, her great abilities and her sense of duty really impressed and inspired me during my PhD. Second, I would like to thank Stefano, Azzurra, Enrico, Leonardo (the king of the labs) and Sara for the fantastic support and friendship they gave me during the experiments and the free-time.

The great patience by which my collaborators of Perugia, Silvia and Leonardo, welcomed me in the lab deserves for sure a big "thank you!". It is not easy, I suppose, for expert biotechnologists to patiently answer at all the questions that a physicist that had never been into a lab can ask. I thank them for the extraordinary support they gave to our projects and for their fantastic friendship.

I would like to thank also all the fantasy-football players of the FANTACERM: Domenico, Silvia, Veronica N., Gaia, Alessia, Matteo, Letizia, Alessio, Vincenzo, Davide and Maria

Grazia. Although we are friends, I won’t give up the first place of our league! Together with them a special thanks goes also to the all the other cermians and in particular to Tommaso, Alessandro DC, Domenico, Veronica G., Josè and our technicians Massimo, Fabio and Enrico. Another acknowledgment goes to our long-term visitor Professor Frans Mulder for our friendship and for his inspiring course.

Last but not least, I thank my beloved wife Chiara for her inestimable love and support, I wouldn't have got far without her. An enormous thanks goes also to my parents Gianni and Gabriela and my grandmother Gina; she passed away in late 2018, this thesis is dedicated to her memory.